Home Institution

University of Messina

Department of ChiBioFarAm

Host Institution

University of Antwerp

Departement Chemie

Electrified CO_2 conversion: Integrating Experimental, Computational, and Process Simulation Methods for Sustainable Chemical Synthesis

Dissertation submitted to obtain the degree of Doctor of Science in "*Advanced Catalytic Processes for using Renewable Energy Sources"* (ACCESS) from the University of Messina and Doctor of Science in "*Chemistry*" from the University of Antwerp defended by

Federica De Luca

Supervisor:

Professor Salvatore Abate (University of Messina)

Co-supervisor:

Professor Annemie Bogaerts (University of Antwerp)

Ph.D. course Coordinator:

Professor Gabriele Centi (University of Messina)

Academic year 2022-2023 – XXXVI cycle

S.S.D. CHIM/04

PON
RICERCA E INNOVAZIONE 2014 - 2020

Ministero dell'Istruzione, dell'Università e della Ricerca

UNIONE EUROPEA
Fondo Sociale Europeo

Abstract (English)

Nowadays, the burning of fossil fuels, particularly petroleum, natural gas, and coal, meets the rising need for power and fuels for automobiles and industries. This has given rise to ecological and climate challenges. This thesis explores these issues from three distinct perspectives: (i) experimental, (ii) computational, and (iii) process simulation, with a focus on studying CO_2 as an alternative and economically viable raw material.

Firstly, the experimental study is focused on the synthesis, characterization, and testing of novel catalysts for electroreduction of CO_2 and oxalic acid, an intermediate product of CO_2. Electrocatalysts based on Cu supported by citrus (orange and lemon) peel biomass are prepared. These catalysts exhibit activity in the electrochemical reduction of CO_2, emphasizing the effectiveness of biomasses, particularly orange peels, as environmentally friendly precursors for sustainable and efficient electrocatalysts. In addition, graphitic carbon nitrides/TiO_2 nanotubes (g-C_3N_4/TiNT) composites are prepared for the electrocatalytic reduction of oxalic acid to glycolic acid, revealing superior electrocatalytic properties compared to pristine TiNT. Characterization by X-ray diffraction, X-ray photoelectron spectroscopy, and scanning electronic microscopy were performed for all the prepared electrocatalysts.

Delving into the reduction of CO_2 on Cu catalysts, a computational study about the synthesis of methanol on Cu(111) surface is performed by using the Vienna Ab initio Simulation Package. A systematic study is carried out to define the activation energies of the elementary reactions by using mGGA DF. Consequently, it is shown that the rate-controlling step is CH_3O^* hydrogenation and the formate pathway on Cu(111) proceeds through the $HCOOH^*$ intermediate.

Finally, the process simulation, performed by using the software Aspen Plus 11 from AspenTech Inc., is based on the comparison of a catalytic (oxidation of ethylene glycol) and an electrocatalytic process (CO_2 electroreduction chain) to synthesize glycolic acid. An economic analysis of the operational and investment costs reveals that the catalytic process is more cost-effective due to the current instability of electrocatalysts and proton exchange membranes, resulting in increased maintenance costs and, consequently, higher prices for the product.

Abstract (Nederlands)

Het verbranden van fossiele brandstoffen, met name aardolie, aardgas en kolen, voorziet momenteel in de toenemende behoefte aan stroom en brandstoffen voor auto's en de industrie. Dit heeft geleid tot ecologische en klimaatuitdagingen. Dit proefschrift onderzoekt deze kwesties vanuit drie verschillende perspectieven: (i) experimenteel, (ii) computationeel en (iii) processimulatie, met de nadruk op het bestuderen van CO_2 als alternatieve en economisch levensvatbare grondstof.

Ten eerste is de experimentele studie gericht op de synthese, karakterisering en het testen van nieuwe katalysatoren voor elektro-reductie van CO_2 en oxaalzuur-een tussenproduct van CO_2. Elektrokatalysatoren op basis van Cu op een drager van citrusschil (sinaasappel en citroen) biomassa worden bereid. Deze katalysatoren vertonen activiteit in de elektrochemische reductie van CO_2, wat de effectiviteit benadrukt van biomassa, met name sinaasappelschillen, als milieuvriendelijke voorlopers voor duurzame en efficiënte elektrocatalysatoren. Daarnaast worden grafietkoolnitriden /TiO_2-nanobuisjes (g-C_3N_4/TiNT) -composieten bereid voor elektrokatalytische reductie van oxaalzuur tot glycolzuur, waardoor superieure elektrokatalytische eigenschappen worden verkregen in vergelijking met enkel TiNT. Karakterisering door röntgendiffractie en röntgenfoto-elektronenspectroscopie en scanning elektronenmicroscopie bevestigen de synthese van alle elektrokatalysatoren.

Voor meer inzicht in de reductie van CO_2 op Cu-katalysatoren, wordt een computationeel onderzoek uitgevoerd naar de synthese van methanol op Cu(111)-oppervlak, met behulp van het “Vienna Ab initio Simulation Package”. Er wordt een systematisch onderzoek uitgevoerd om de activeringsenergieën van de elementaire reacties te definiëren met mGGA DF. Hierbij wordt aangetoond dat de snelheidsbepalende stap de CH_3O * hydrogenatie is, en dat het formaat pad op Cu(111) verloopt via het HCOOH * tussenproduct.

Ten slotte wordt een processimulatie uitgevoerd met de software Aspen Plus 11 van AspenTech Inc., gebaseerd op de vergelijking van een katalytisch (oxidatie van ethyleenglycol) en een elektrokatalytisch proces (CO_2-elektroreducie-ketting) om glycolzuur te synthetiseren. Uit een economische analyse van de operationele en investeringskosten blijkt dat het katalytische proces kosteneffectiever is vanwege de huidige instabiliteit van elektrokatalysatoren en protonuitwisselingsmembranen, resulterend in hogere onderhoudskosten, en bijgevolg hogere prijzen voor het product.

Abstract (Italiano)

Attualmente, la combustione di combustibili fossili, in particolare petrolio, gas naturale e carbone, soddisfa il crescente bisogno di energia e di combustibili per automobili e industrie. Ciò ha dato origine a sfide ecologiche e climatiche. Questa tesi esplora queste problematiche attraverso tre prospettive distinte: (i) sperimentale, (ii) computazionale e (iii) di simulazione di processo, con particolare attenzione allo studio della CO_2 come materia prima alternativa ed economicamente valida.

In primo luogo, lo studio sperimentale si concentra sulla sintesi, la caratterizzazione e il test di nuovi catalizzatori per l'elettroriduzione della CO_2 e dell'acido ossalico, un intermedio della CO_2. Alcuni elettrocatalizzatori a base di Cu supportato da biomassa di buccia di agrumi (arancia e limone) sono stati preparati. Questi ultimi mostrano attività nella riduzione elettrochimica della CO_2, sottolineando l'efficacia delle biomasse, in particolare delle bucce d'arancia, come precursori ecologici per elettrocatalizzatori sostenibili ed efficienti. Sono stati invece preparati compositi di nitruri di carbonio grafitico/ nanotubi di TiO_2 (g-C_3N_4/TiNT) per la riduzione elettrocatalitica dell'acido ossalico ad acido glicolico, rivelando proprietà elettrocatalitiche superiori rispetto al TiNT tal quale. Caratterizzazione mediante diffrazione di raggi X, spettroscopia di fotoelettroni a raggi X e microscopio elettronico a scansione è stata effettuata su tutti gli elettrocatalizzatori.

Approfondendo la riduzione della CO_2 su catalizzatori di Cu, è stato effettuato uno studio computazionale sulla sintesi del metanolo sulla superficie di Cu(111) utilizzando il software Vienna Ab initio Simulation Package. È stato condotto uno studio sistematico per definire le energie di attivazione delle reazioni elementare utilizzando mGGA DF. Di conseguenza, si dimostra che il passo che controlla la velocità è l'idrogenazione di CH_3O^* e che il percorso del formiato su Cu(111) procede attraverso gli intermedi del HCOOH*.

Infine, la simulazione di processo, eseguita utilizzando il software Aspen Plus 11 di AspenTech Inc. si basa sul confronto tra un processo catalitico (ossidazione del glicole etilenico) e uno elettrocatalitico (catena di elettroriduzione della CO_2) per sintetizzare l'acido glicolico. Un'analisi economica dei costi operativi e di investimento rivela che il processo catalitico è più conveniente a causa dell'attuale instabilità degli elettrocatalizzatori e delle membrane a scambio protonico, con conseguente aumento dei costi di manutenzione e, di conseguenza, del prezzo del prodotto.

Table of Contents

ACRONYMS

GHG	Greenhouse Gas
CFC	Chlorofluorocarbons
COP	Conference of the Parties
CCS	Carbon Capture and Storage
CCU	Carbon Capture and Utilization
DAC	Direct Air Capture
LUMO	Lowest Unoccupied Molecular Orbital
HOMO	Highest Occupied Molecular Orbital
HER	Hydrogen Evolution Reaction
SHE	Standard Hydrogen Electrode
SCE	Saturated Calomel Electrode
CEM	Cation Exchange Membrane
FA	Formic Acid
OX	Oxalic acid
CNT	Carbon Nanotube
GDL	Gas Diffusion Layer
SEM	Scanning Electrons Microscope
SE	Secondary Electron
BSE	Back-scattered electron
EDX	Energy-dispersive X-ray spectroscopy
XPS	X-ray PhotoelectronSpectroscopy
BE	Binding Energy

IR	Infrared (spectroscopy)
XRD	X-ray diffraction
WE	Working Electrode
TCD	Thermal Conductivity detector
CV	Cyclic Voltammetry
ECSA	Electrochemical Surface Area
C_{DL}	Double Layer Capacitance
C_s	Specific Capacitance
FE	Faradaic Efficiency
LC-MS	Liquid Chromatography–Mass Spectroscopy
TiNT	Titanium oxide Nanotube array
GO	Glyoxylic acid
GC	Glycolic acid
$g\text{-}C_3N_4$	Graphitic Carbon Nitride
AO	Anodic Oxidation
CVD	Chemical Vapor Deposition
FWHM	Full Width at Half Maximum
M	Melamine
U	Urea
MU	Melamine-Urea
VASP	Vienna Ab initio Simulation Package
DFT	Density Functional Theory
mGGA	meta-generalized gradient approximation

GGA	Generalized Gradient Approximation
NEB	Nudge Elastic Band
VTST	VASP Transition State Tool
TS	Transition State
PBE	Perdew–Burke-Ernzerhof
PW91 DF	Perdew-Wang Density Functional
CARG	Compound Annual Growth rate
NRTL	Non-random Two-Liquid model
ELECNRTL	Electrolyte Non-Random Two-liquid model
KFA	Potassium Formate
AACE	Association for the Advancement of Cost Engineering
OPEX	Operational Expense
CAPEX	Capital Expense
CEPCI	Chemical Engineering Plant Cost Index
EE	Energy Efficiency
M&O	Maintenance and Operation

LIST OF TABLES

LIST OF IMAGES

CHAPTER 1

1.1 Introduction

Nowadays, the burning of fossil fuels, particularly petroleum, natural gas, and coal meets the rising need for power and fuels for automobiles and industry. However, the extraction, refining, and use of fossil fuels contribute to CO_2 emissions, which contribute to global warming and climate change[1]. The increasing CO_2 emission is not only because of humans, as greenhouse gases are even produced by natural processes e.g., organic matter decomposition, forest fires, volcanic eruptions, and so on[2].

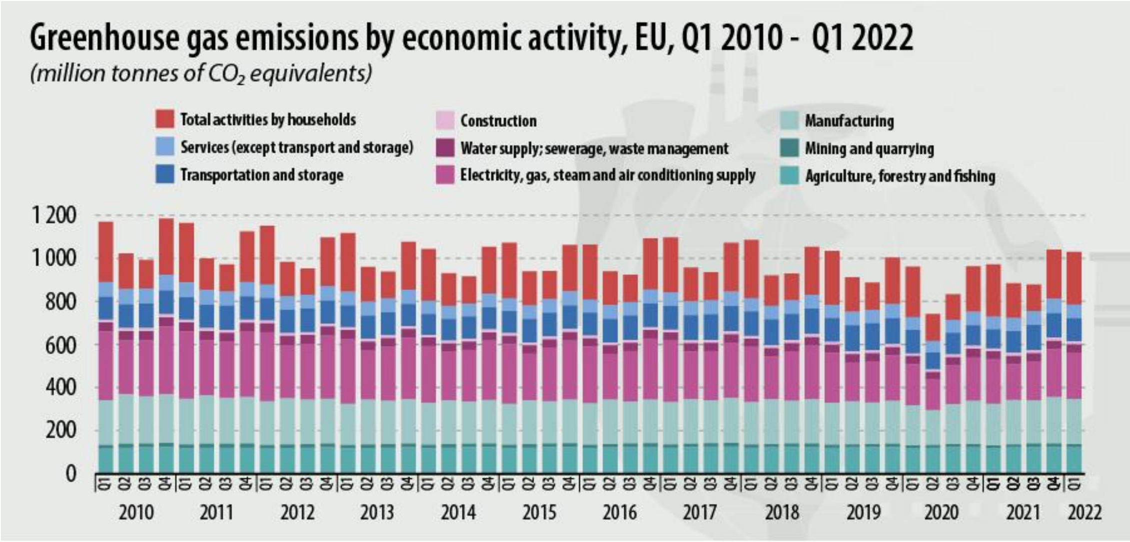

ec.europa.eu/eurostat

Figure 1.1: European greenhouse gas emissions by sector from 2010 to 2022 (Source Data: https://ec.europa.eu/).

As shown in figure 1.1, households (24%), power and gas supply (21%), and manufacturing (20%) were the economic sectors responsible for the greatest greenhouse gas emissions, followed by agriculture (12%) and transportation and storage (10%). Greenhouse gas emissions grew in all sectors except households, which stayed unchanged (245 million tons CO_2-eq.) from the same time in 2021. Transportation and storage (+21%), mining (+15%), and building (+11%) had the greatest growth. CO_2 is the most prevalent greenhouse gas (GHG), with a total global emission rate of 40 gigatons per year and over 3200 gigatons in the atmosphere. Coal is the dominant source of energy for power production among conventional fossil fuels, and it is the second-largest feedstock of primary energy after crude oil [3]. Figure 1.2 shows the sources for producing energy worldwide: 84% of the total energy demand is met by fossil fuels (including 33%, 27%, and 24% from oil, coal, and natural gas, respectively), with 6% coming from hydroelectricity, 5% coming from renewable sources, and 4% from nuclear power.

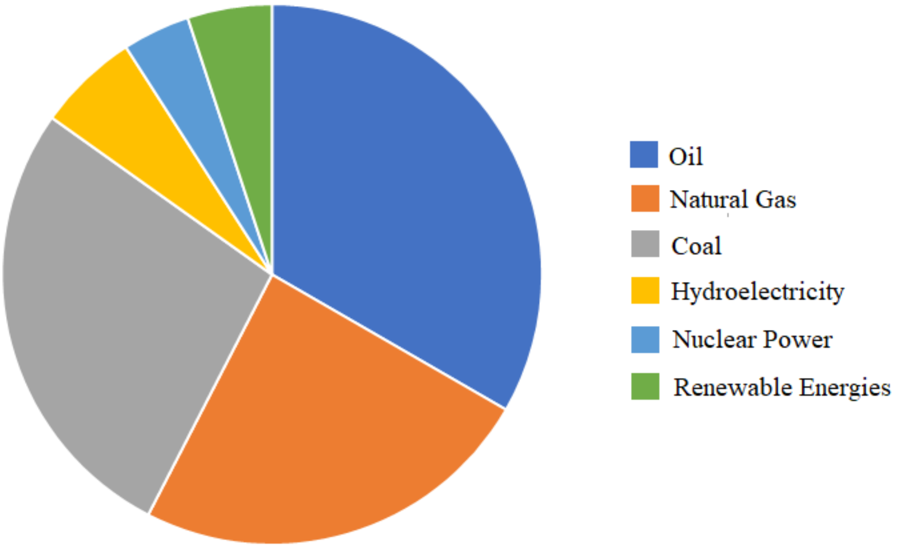

Figure 1.2: Sources for energy production: 33% oil, 27% coal, 24% natural gas, 6% hydroelectricity, 5% renewable energies, and 4% nuclear power (International Energy Agency – IEA).

Carbon dioxide, methane, nitrous oxide, chlorofluorocarbons (CFC), and water vapor are examples of greenhouse gases. They are naturally components of the Earth atmosphere. Greenhouse gases play a vital role because they can retain a part of the infrared component of the solar radiation that affects the Earth, thereby regulating the temperature of our planet. Each gas has a different behavior:

- **Carbon dioxide** is the main component due to its concentration but is not as effective as many other greenhouse gases. Because of its amount in the atmosphere its total radiative forcing is greater.
- **Water vapor** is the main natural greenhouse gas, whose presence in the atmosphere is constantly regulated by its property to condense and fall back in the form of precipitation.
- **Methane** has far lower concentrations than CO_2 but has a much larger potential for infrared radiation absorption and emission.
- **Nitrous oxide** is a gas with a high capacity to absorb heat but is present in much lower concentrations than the other gases.
- **CFC** is a class of compounds derived solely from anthropogenic activities with high greenhouse power, but thanks to numerous international agreements, their atmospheric concentrations have steadily declined since the 1990s.

However, as is already known, human and natural activities have led to an increase in carbon dioxide and other greenhouse gas concentrations in the atmosphere. Because of the release into the atmosphere of much higher quantities than the natural levels of these gases, an imbalance has been created that has transformed the greenhouse effect from positive to negative.
As reported by among others "*National Geographic*" the increasing GHG concentration in atmosphere provokes climate change.

The main side effects of climate change are:

- **Temperature increase:** There is a worldwide average temperature anomaly between 1850 and 2025 (pre-industrial and current period). As is clear from figure 1.3, the worldwide average temperature has increased significantly over the years, exceeding 1.1° C and it is predicted to further grow in the follow decades. As consequence, it will lead to the desertification, intensification and spread of extreme weather events such as droughts, hurricanes, and floods [4].

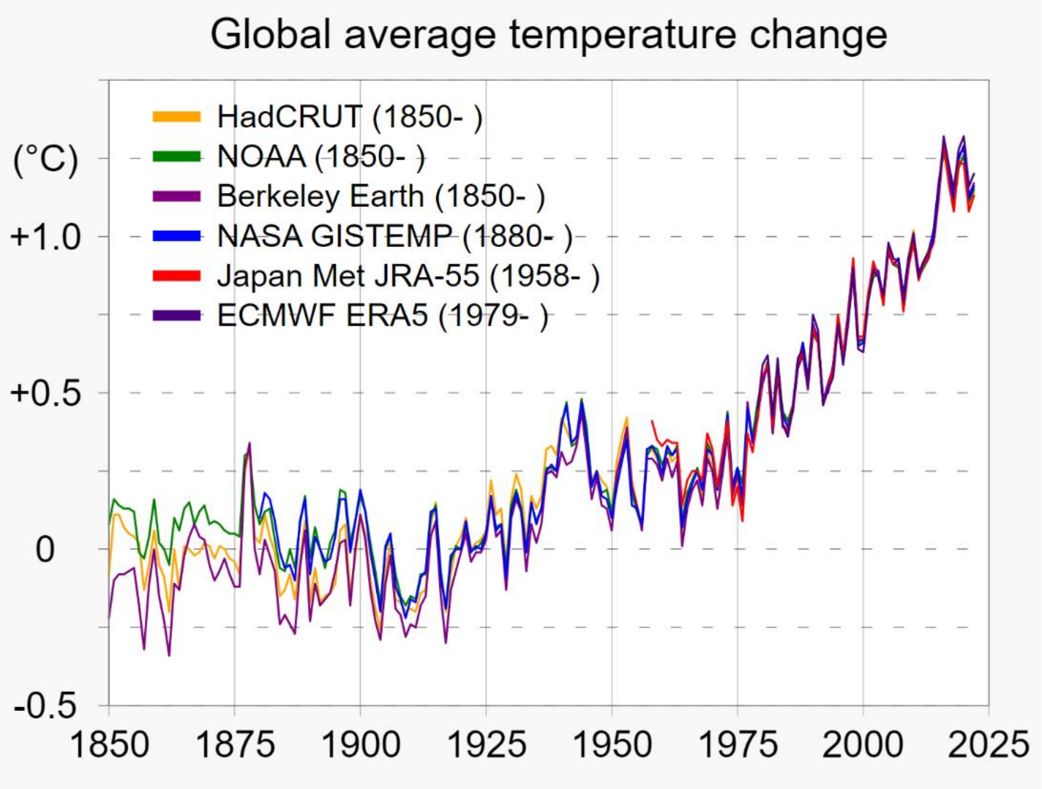

Figure 1.3: Data from different scientific organizations on worldwide average temperatures is highly connected. (The "0" number in this figure represents the average temperature from 1850 to 1900, which is considered the "pre-industrial" temperature level) [5–8].

- **Acidification of oceans:** Around 50% of atmospheric CO_2 dissolves in the seas and creates carbonic acid:

  $CO_{2\,(g)} + H_2O \leftrightarrows H_2CO_{3\,(aq)}$

  Carbonic acid then dissolves, releasing H_3O^+ ions:

  $H_2CO_{3(aq)} + H_2O \leftrightarrows H_3O^+ + HCO_3^-$

  This process causes a decrease in the pH of the oceans.
- **Glacier meltdown**: In the Arctic, where warming is two or three times greater, glaciers are melting [9]. This causes increase of the sea level.

Projections show an increase in average sea level of 0.26 to 0.77 meters by 2100, submerging small islands, shallow coastal regions, and river deltas.

- **Economy:** The rising global temperatures will put economic growth at jeopardy. For instance, it will be caused by a decrease in area of land that can be cultivated, and therefore a minor production of corn, rice, wheat, and other cereals, especially in America, Africa, and Asia.

These changes affect the ecosystem (e.g., biodiversity loss, species extinction, change in biological cycles, disturbances in marine ecosystems, and so on) and living beings (health problems, food safety, forced migration, etc.).

1.2 Policy measures to mitigate global warming

During the last decades, several international measures have been taken. First of these is the Kyoto protocol (1997), which established greenhouse gas emission reduction obligations for industrialized countries. Associated with the latter, a Clean Development Mechanism was created to incentivize emission reduction projects in developing countries. It has been operational since 2000. In addition, many enterprises and private sector organizations have made voluntary promises to minimize CO_2 emissions and implement more sustainable practices in recent decades.

Subsequently, as of 2015, the United Nations had created 17 Sustainable Development Goals, generally known as the 2030 Agenda. The 17 points cover a wide range of economic and social concerns (Figure 1.4).

These objectives are intended to solve a variety of global issues, including poverty, inequality, climate change, environmental degradation, peace, and justice.

Figure 1.4: 17 goals of sustainable development (https://sdgs.un.org/goals).

Furthermore, in 2015, at COP 21 in Paris, an international agreement (Paris Agreement) established long-term goals for mitigating climate change. The Agreement established a series of deadlines and review cycles to guarantee that nations gradually enhance their ambition in terms of limiting emissions and adapting to climate change. The primary goal is to keep the global average temperature rise "well below" 2° Celsius over pre-industrial levels, with the goal of maintaining the rise to 1.5° Celsius.

Besides, in November 2021, at COP 26 in Glasgow, another ambitious aim was confirmed namely to achieve net-zero emission of carbon by 2050. The Paris Agreement impact will be determined by additional action and commitment by member countries and the international community. It is critical to recognize that climate change is a complex and ongoing problem, and that implementing the Agreement will need a continual and rising commitment to accomplish the long-term mitigation and adaptation targets. Policies, efforts, technical improvements, and shifts in worldwide awareness of the problem's importance will all have an impact on future developments.

Recently, in December 2023, at COP 28 in Dubai, the need was highlighted to reach the peak of global greenhouse gas emissions by 2025 and reduce them with 43% by 2030 and with 60% by 2035 compared to 2019 levels, to limit global warming to 1.5 ºC. In addition, due to the current environmental impact of energy production, the participating parties were encouraged to phase out fossil fuels by 2050, tripling the world’s renewable energy capacity and doubling the rate of energy efficiency improvement by 2030.

Consequently, to overcome the crucial challenges of CO_2 emission mitigation several measures are considered e.g., the transition to renewable energy sources, carbon capture and storage (CCS), and carbon capture and utilization (CCU), i.e., the valorization of CO_2. CO_2 valorization means the conversion into added-value products via electro-catalytic, photo-catalytic, thermo-catalytic, plasma-catalytic or biological methods.

1.3 Transition to renewable energy sources

To meet the goals of COP26 and COP28, the main tool is the energy transition which is the change from an energy based on fossil fuels to one based on renewable energy sources to reach zero CO_2 emission within 2050. The electrification of consumption, which replaces fossil fuel-generated electricity with energy generated from renewable sources, contributes significantly to decarbonization.

Renewable energy is derived from natural resources that renew continuously over time, such as sunlight, wind, waves, tides and so on. Renewable energy sources represent any form of energy that can be regenerated regularly and can never run out. The benefits of renewable energy are numerous, including (i) equipment that requires less maintenance, (ii) renewable sources that are found all over the world, making them more reliable as a source of energy than fossil fuels. (iii) Using renewable energy reduces greenhouse gas emissions, and (iv) energy costs stabilize. Obviously, renewable energy sources have certain drawbacks: (i) the initial setup costs are very expensive; (ii) high storage costs pose a challenge for storing energy; (iii) renewable energy relies on weather conditions that can be unpredictable, resulting in possible energy shortages; and (iv) a wide area is required for establishing sufficient renewable energy[10].

Currently, the market for renewable energy is expected to expand significantly during the next decade. Iceland and Norway are now the only two countries that produce all of their power from renewable sources. Furthermore, at least 47 nations presently produce more than half of their power from renewable sources, with the goal of reaching 100% renewable by 2050 [11]. The fast adoption of renewable energy and energy efficiency technology is resulting in increased energy security, climate change mitigation, and economic advantages. According to "*Bloomberg New Energy Finance*", by 2050, solar and wind energy will meet around 50% of the global energy demand, while fossil fuel consumption will decrease by 11%. The lower cost of renewable energy will have an impact on the cost of electricity generated from renewable resources, and renewable energy will eventually become the most cost-effective means of generating power.

1.4 Carbon capture and storage

Carbon capture and storage technologies have been identified as one of the best options for lowering CO_2 levels in the atmosphere [12]. Several investigations on CO_2 capture, usage, and storage methods have been performed. CO_2 capture technologies are critical globally because CO_2 emissions from fossil fuels have posed serious threats to the economy, the environment, natural ecosystems, and human health. Capture, storage, and use of carbon can be accomplished in three phases. As shown in figure 1.5, the first step is to remove CO_2 from the source, then CO_2 is capture by membrane separation, physical and chemical absorption, and other approaches, following by the separation, and finally storage [13,14].

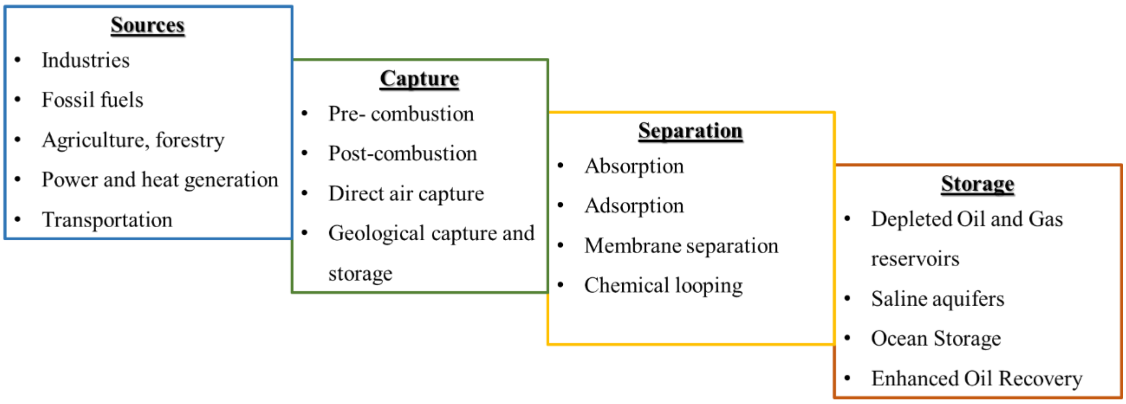

Figure 1.5: Common CO_2 sources, followed by its usual capture, separation, and storage pathway.

The main CO_2 capture methods include pre-combustion, post-combustion, and direct air capture.

- **Pre-combustion** occurs before the combustion process during which the fuel is gasified in the presence of oxygen and steam, resulting in syngas production. CO from syngas is transformed into CO_2 and collected before combustion via the water-gas shift reaction, whereas H_2 in syngas is utilized as a direct fuel in gas turbines [15].To extract CO_2 from the produced syngas, the pre-combustion capture technology employs both physical and chemical approaches. Chemical absorbents such as carbonates and physical solvents such as methanol and polypropylene glycol are commonly employed on a commercial basis for CO_2 collection [16].
- **Post-combustion**, as the name-implies, involves the removal of CO_2 from the gas emitted by coal-fired power plants and other industrial enterprises after the combustion process. For transforming existing power plants, post-combustion methods are the preferred alternative. Membrane separation, chemical looping, chemical and physical absorption are the most prevalent post-combustion carbon capture processes.

- CO_2 is present in the air in a considerably lower concentration than it is in industrial exhaust emissions. There are currently two methods for extracting CO_2 from the air: **solid and liquid direct air capture (DAC)**. Solid DAC employs solid sorbent materials capable of chemical adsorption of CO_2. The concentrated CO_2 contained in the filter can be recovered by heating or storing it in a vacuum system for later storage or usage. The air in liquid DAC systems is routed through a hydroxide solution, which removes the CO_2. The acquired CO_2 can subsequently be stored in deep geological rocks or ocean bottoms by high-pressure injection [17].

Another of several used methods to capture and store CO_2 is geo-sequestration. It is the process of permanently storing CO_2 underground by injecting it into porous rocks or beneath the bottom of the ocean [18]. The injected CO_2 fills the pores inside the rocks and is held in place from above by a waterproof coating.

Geological sequestration is an efficient method of absorbing CO_2 from its source point at enterprises or other energy sources and storing it in deep geological formations [19–21]. CO_2 capture, transit, and storage are the three major steps of geological CO_2 sequestration. During the capture step, CO_2 is separated from other gases at the place of emission using various methods. The collected CO_2 is compressed into a thick fluid and transferred to the storage facility via pipes or ships. Finally, the compressed CO_2 is pumped into deep geological formations to be permanently stored. Geological CO_2 storage is typically carried out in depleted oil and gas reservoirs by injecting high-pressure, compressed, and fluidized CO_2 (supercritical CO_2) in order to replace the residual oil and gas. The reservoir pressure varies between 4.4 and110 MPa[22]. Other potential geological formations for CO_2 storage include saline formations in extremely absorbent and porous sedimentary basins, which have the greatest storage capacity [20]. Geological sequestration is a fast-emerging sector that is tackling economic, technological, and environmental concerns via continuous research and development.

1.5 Valorization of CO_2

Excessive anthropogenic CO_2 emissions led to ecological, and climate challenges. To mitigate these negative consequences, turning CO_2 into fuels or commodity chemicals signals the beginning of an energy transition from today "fossil fuel economy" to a sustainable "CO_2 economy." Conversion of CO_2 rather than sequestration is a hot issue as a potential alternative solution to CO_2 emissions into the environment. The production of valuable value-added compounds as an alternative to petrochemistry looks promising since it offers the dual benefit of recycling CO_2 while saving fossil resources and minimizing CO_2 emissions from their usage.

Currently, research efforts are concentrated on using CO_2 as a carbon source due to its potential to serve as a true feedstock for the production of added value compounds, thereby transforming a negative into a positive. CO_2 may be transformed in a variety of ways, including electro-chemical [23–26], photo-chemical [27], thermo-chemical[28] and plasma-chemical processes[29]. Nonetheless, CO_2 conversion is a difficult task due to its high thermodynamic stability, attributed to the two strong equivalent C=O linear bonds, i.e., double bonds with a much higher bonding energy (750 kJ mol^{-1})than single bonds[30]. Also, CO_2 has a large energy gap (13.7 eV) between its lowest unoccupied molecular orbital (LUMO) and highest occupied molecular orbital (HOMO)[31]. As a result, an appropriate CO_2 transformation method must overcome these energy barriers, which need significant energy input, ideally from carbon-neutral sources, as well as the utilization of an active catalyst or high pressures and temperatures, or the use of plasma technology [32,33].

To speed up this reduction process, homogeneous[34] and heterogeneous catalysts[35] were used. Although homogeneous catalysis achieves great selectivity, most homogeneous systems have problems such as high cost, toxicity, poor stability, and complicated post-separation, which restrict practical use. These problems are less likely to occur in heterogeneous catalysis.

1.6 Electrocatalysis

Since the start in the 19th century, electrochemistry has evolved to serve a wide range of applications, including energy storage, metallurgy, and chemical synthesis[36]. The use of an applied potential, in general, allows for the acceleration of reactions far beyond thermodynamic equilibrium, allowing access to reaction pathways and chemical intermediates that would otherwise be impossible to utilize.

Electrochemistry allows for substrate activation at the electrode surface. This way of activation frequently necessitates substrate engineering to regulate reactivity and might forego control over the selectivity of chemical processes after electron transfer[37]. Such limits can be overcome through electrocatalysis that uses redox-active catalysts, which enable efficient electron transfer and provide more selectivity than non-mediated processes[38].

Also, one significant trend in the development of electrocatalysis involves the integration of nanotechnology[39–41]. Nanomaterials, such as nanoparticles, nanowires, and nanotubes, offer advantages:

- **Enhanced surface area:** nanomaterials typically have high surface-to-volume ratios due to their small size and increased surface area. This property allows for more active sites for electrochemical reactions to occur, leading to improved catalytic activity[42].
- **Facilitated mass transport:** nanomaterials often exhibit favorable transport properties for reactants and products. Their small size and porous structures can facilitate the diffusion of ions and molecules, reducing mass transport limitations[43].
- **Catalyst support:** nanomaterials can serve as excellent supports for catalytically active species. For example, metal nanoparticles supported on

carbon nanotubes or graphene can combine the unique properties of both materials, leading to synergistic effects that enhance overall electrocatalytic performance[44].

- **Tailored morphology and composition**: nanotechnology enables precise control over the morphology and composition of electrocatalysts. This tunability allows researchers to design materials with specific characteristics to meet the requirements of a particular electrochemical application and therefore enhance catalytic activity[45].

Finally, another reason that increases the scientific interest in generating commodity chemicals and fuels from electricity is that electrocatalysis can be combined with clean and renewable electricity which is becoming ever more convenient. The use of electricity instead of ecologically hazardous chemical reagents such as stoichiometric oxidants and reductants makes electrocatalysis an appealing method for increasing the efficiency and sustainability of synthetic chemistry.

Despite all advantages of electrocatalysis, some drawbacks can be highlighted, in particular:

- **Cost and availability:** many efficient electrocatalysts, particularly those based on precious metals like platinum[46], can be costly and limited in availability, posing economic challenges for large-scale applications.
- **Durability and stability:** maintaining the stability and durability of electrocatalysts over extended periods is a significant challenge. Catalyst degradation can occur due to factors such as corrosion, poisoning, or structural changes.

Addressing these challenges is crucial for the continued advancement and practical implementation of electrocatalysis in various fields, including energy storage, conversion, and environmental applications.

1.7 Electrocatalysis vs thermal catalysis: reduction of CO_2

CO_2 emissions from the use of fossil fuels may be captured and converted employing renewable energy to chemicals or fuels. Among the procedures for reducing CO_2 emissions, catalysis is an efficient, cost-effective, and long-term method for converting CO_2 to chemicals and fuels[47,48]. The catalytic conversion techniques are particularly appealing since they may minimize the use of fossil fuels while also providing an economic incentive to use CO_2. For instance, in thermal catalysis, CO_2 and other gases (such as renewable H_2) are converted by passing over catalysts at high temperatures and pressures. By electrocatalytic process, on the other hand, dissolved or gaseous CO_2 reacts at the electrolytes and electrodes (electrocatalysts) interface (with protons and electrons exchange), often at ambient or near-ambient temperatures.

So far, thermal catalytic hydrogenation of CO_2 (figure 1.6) has produced formic acid[49], methane[50,51], carbon monoxide[52], methanol[53], hydrocarbon[54], olefins[55] on selected catalysts and a pressures range from 0.1 to 10 MPa. In contrast, electrocatalytic reduction of CO_2 can also produce similar products (figure 1.6) such as carbon monoxide[56], formic acid[57], methane[58], methanol[59], ethylene[60], ethanol[61], propylene[62], and higher carbon-containing products[63]. It depends on the chosen electrocatalysts, the controlled potential range (-0.1 to -3 V vs. RHE), and electrolyte (neutral, acidic, and alkaline). In literature, there are a plethora of papers regarding CO_2 reduction via thermal-catalysis [54,55,64,65] or electrocatalysis[61,66–68].

Here, their similarities, differences and commonalities will be discussed. In theory, any heterogeneous process involving redox reactions, adsorption of charged intermediates, or even heterolysis of small molecules should have analogies with electrochemical reactions happening at electrified surfaces[69].

Temperature and pressure are the main driving forces to overcome the activation barrier and enhance the reaction rate in the thermal-catalytic CO_2 reduction process. The energy required or released is passed through the reactants and/or thermal-catalysts since almost all of the reactants are in touch with a thermal-catalyst. The conversion of some processes is often restricted by thermodynamic equilibrium, and these reactions have undergone extensive thermodynamic research[70].

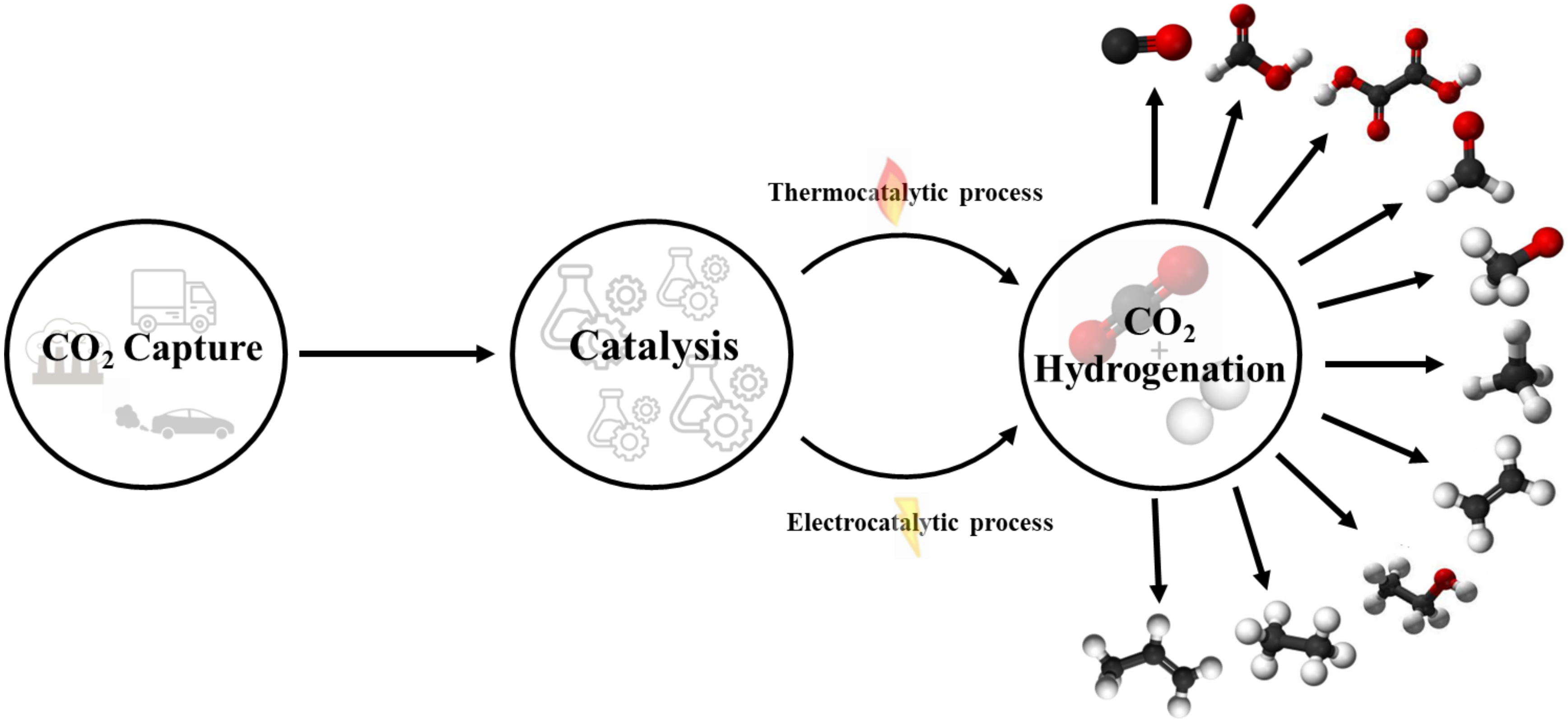

Figure 1.6: Main products from the reduction of CO_2.

A fixed bed reactor (shown in figure 1.7) is the most often used reactor in CO_2 thermal-catalytic hydrogenation. It is generally a cylindrical tube filled with thermal-catalyst pellets, with gas reactants (CO_2 and H_2) passing through the packed catalyst bed and being transformed into products. CO_2 hydrogenation temperatures and pressures vary depending on the product, but the basic ranges are 100°-500° C and 0.1-10 MPa, respectively.

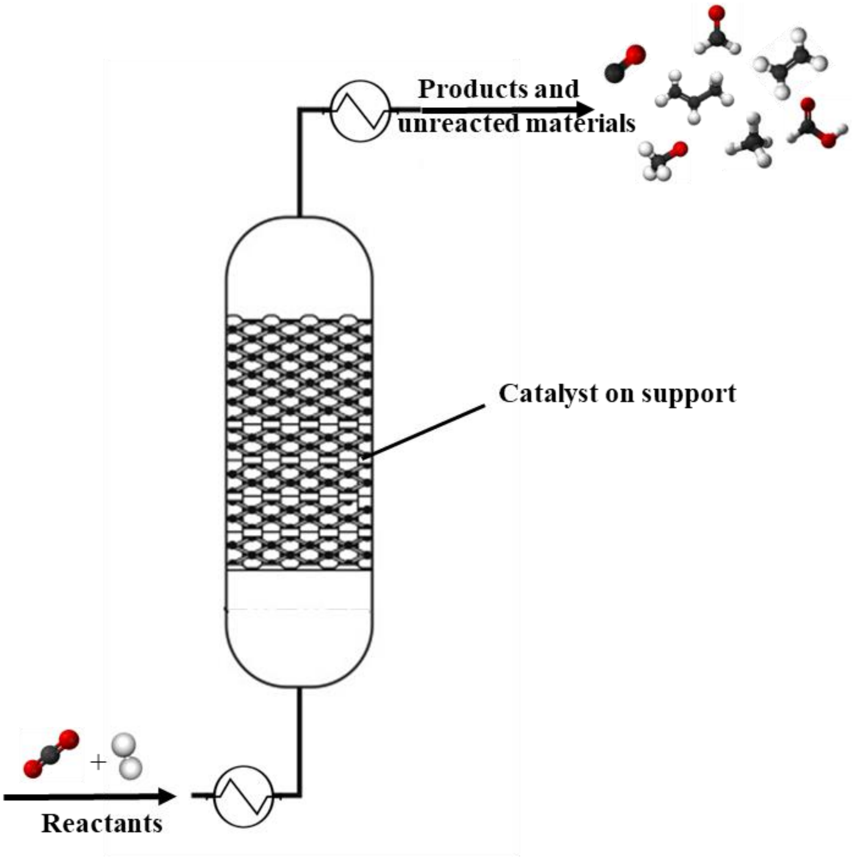

Figure 1.7: Ideal fixed bed reactor design to convert CO_2.

Thermal catalysts for CO_2 hydrogenation need the simultaneous activation of CO_2 molecules and H_2 molecules, and numerous transition metals and metal oxides, as well as nonmetals, exhibit high activity and selectivity. In the case of electrocatalytic CO_2 conversion, the reactor (electrochemical cell) used in are typically consists in two forms, as shown in figure 1.8.

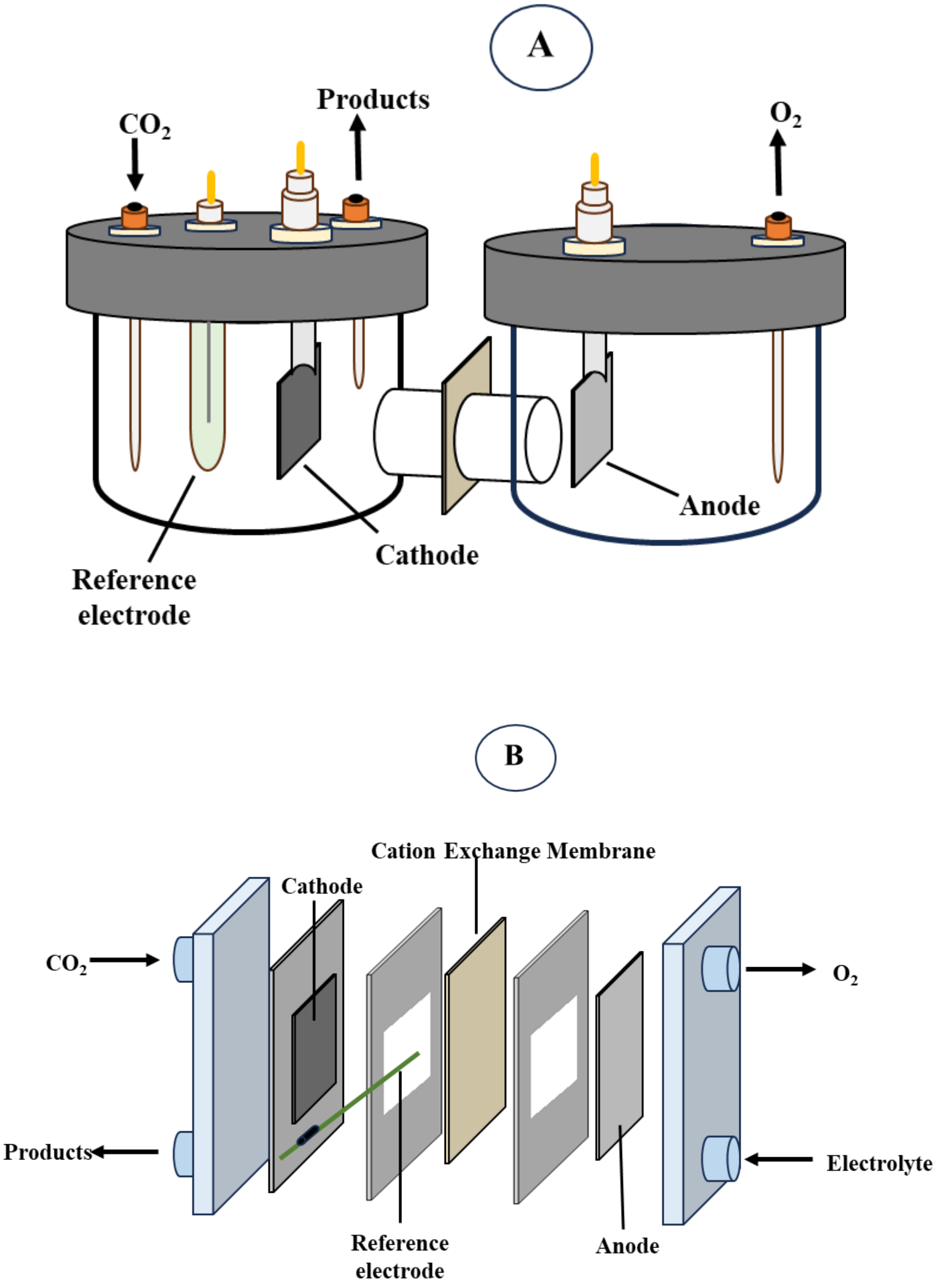

Figure 1.8: Typical three-electrodes setup electrochemical cell: A) H-type cell, and B) flow-type cell.

The electrochemical reactions need conductors for electron transport and electrolytes for ion transport, making the electrochemical reaction process more complex than the thermochemical reaction process. Temperature and overpotential can be used to control the rate of electrochemical processes. It should be remembered that while higher temperatures might speed up an electrochemical process, they also reduce the efficiency of the applied overpotential. Typically, the overpotential (the difference between the thermodynamically calculated equilibrium potential and the potential used to initiate the reaction) is more effective in lowering the activation barrier and enhancing kinetics. Also, a catalyst can bind or interact with the chemical intermediates, stabilizing them and significantly lowering the activation energy[71]. Generally, a proton-electron pair is utilized as a reactant in electrocatalysis to reduce CO_2 ($CO_2 + nH^+ + ne^-$), with the chemical potential of electrons and protons adjustable by the applied electrode voltage. This differs from the thermo-catalysis procedure, in which pressure and temperature are commonly used to change the chemical potential of H_2. An optimum electrocatalyst can minimize the overpotential necessary to drive a certain electrochemical process, boosting electrical efficiency. To produce a full chemical reaction, the cathodic half-reactions must be combined with an anodic half-reaction that gives protons and electrons (e.g., water oxidation reaction: $2H_2O \leftrightarrow O_2 + 4H^+ + 4e^-$). After the production on the anodic side, protons and electrons move to the cathodic side to make the electrochemical CO_2 reduction process take place. In addition to the favored reaction, a side reaction can occur which can compete with it, namely the hydrogen evolution reaction (2H+ 2e- ↔ H2, E0 = 0 V vs. RHE). As consequence, the hydrogen evolution reaction (HER) is a critical side reaction in CO_2 electrochemical reduction. CO_2 electroreduction may produce a variety of products and many mechanistic paths have been postulated, with crucial intermediates such as *CO, *OH, COOH*/CHO*, and OCHO* playing a crucial part in the determination of end products. More electron and proton transfer steps are required to form multi-carbon compounds, complicating the reaction pathway, and making mechanistic investigations more difficult.

Thermal-catalytic reduction of CO_2 to produce added value chemicals such as CO, CH_4, and CH_3OH, etc. needs molecular H_2 as the reactant. The reaction is often carried out at a higher temperature range of 100° to 500° C and at a greater pressure range of 0.1-10 MPa. The major benefits of thermal-catalytic CO_2 hydrogenation are simpler reactor construction and better output rates. The main issue is producing green hydrogen, which is strongly reliant on local water supplies and renewable energy for power generation, making the entire process area dependent. In contrast, electrocatalytic CO_2 reduction normally occurs at lower temperatures (max. 100° C) and pressures (<1 MPa). Furthermore, electrocatalytic CO_2 conversion employs water as the hydrogen supply rather than molecular H_2, allowing for more flexibility in process design. However, the design of a CO_2 electrolyzer, which involves three phases (CO_2 gas, liquid electrolytes, and solid electrocatalysts), is more difficult than that of a thermal-catalytic reactor, and the former is not frequently employed at the industrial scale at the moment. Furthermore, electrocatalytic CO_2 reduction often has a lower product yield than thermal catalysis. Although electrolysis in an acidic environment is regarded a promising method[72], it still has low performance and stability.

Furthermore, the energy input for thermal-catalytic CO_2 hydrogenation is mostly in the form of heat from the burning of fossil fuels in an engine, whereas the energy input for electrocatalytic CO_2 reduction is primarily from electricity. In terms of product separation, the thermal-catalytic technique offers benefits in liquid phase product separation since it can readily separate them from unconverted gases CO_2 and H_2. Because the product concentration is generally low and dissolved in the liquid electrolyte, similar product purification or separation in electrocatalytic CO_2 reduction will be more energy intensive. Also, as compared to thermal-catalytic CO_2 hydrogenation processes, chemical engineering characteristics such as technical current densities, mass transfer, and energy efficiency of most electrocatalytic CO_2 reduction processes are far from mature.

To summarize, thermal- catalytic and electrocatalytic processes have advantages and drawbacks. At the same time, the use of renewable hydrogen via thermal catalysis or renewable electricity via electrocatalysis to produce valuable chemicals and fuels (e.g., formic acid, carbon monoxide, methanol, methane, ethylene, ethanol) provides an appealing and sustainable way to address our climate change challenge. Although the thermal-catalytic route is already at industrial-scale applications, several of the processes are constrained by slow kinetic or thermodynamic equilibrium. On the other hand, the electrocatalytic method to CO_2 reduction is far from mature, although it has certain benefits, such as ambient temperature and pressure, the use of water as a hydrogen source, and the lack of thermodynamic equilibrium constraints.

1.8 Aim of thesis

The aim of the thesis, as outlined in the abstract, is to address the ecological and climate challenges associated with the burning of fossil fuels, specifically petroleum, natural gas, and coal. The thesis explores this issue from three perspectives: experimental (chapter 2 and 3), computational (chapter 4), and process simulation (chapter 5), with a specific focus on studying carbon dioxide (CO_2) as an alternative and economically viable raw material.

Bibliography

1. Zeng, C., Stringer, L. C. & Lv, T. The spatial spillover effect of fossil fuel energy trade on CO 2 emissions. *Energy* **223**, 120038 (2021).

2. Nanda, S., Reddy, S. N., Mitra, S. K. & Kozinski, J. A. The progressive routes for carbon capture and sequestration. **6**, 99–122 (2016).

3. Wei, X., Manovic, V. & Hanak, D. P. Techno-economic assessment of coal- or biomass-fired oxy-combustion power plants with supercritical carbon dioxide cycle. *Energy Convers. Manag.* **221**, 113143 (2020).

4. Suarez-gutierrez, L. *et al.* Extreme heat waves under 1 . 5 ° C and 2 ° C global warming OPEN ACCESS Extreme heat waves under 1 . 5 ◦ C and 2 ◦ C global warming. (2018).

5. Morice, C. P. *et al.* An Updated Assessment of Near-Surface Temperature Change From 1850: The HadCRUT5 Data Set. *J. Geophys. Res. Atmos.* **126**, (2021).

6. Lenssen, N. J. L. *et al.* Improvements in the GISTEMP Uncertainty Model. *J. Geophys. Res. Atmos.* **124**, 6307–6326 (2019).

7. Hersbach, H. *et al.* The ERA5 global reanalysis. *Q. J. R. Meteorol. Soc.* **146**, 1999–2049 (2020).

8. Pérez-Fortes, M. & Tzimas, E. *Techno-economic and environmental evaluation of CO2 utilisation for fuel production. Synthesis of methanol and formic acid*. *Scientific and Technical Research Series* (2016). doi:10.2790/89238.

9. Logan, C. A. A Review of Ocean Acidification and America ' s Response. **60**, 819–828 (2010).

10. Quéré, C. Le *et al.* Global Carbon Budget 2016. 605–649 (2016) doi:10.5194/essd-8-605-2016.

11. Treasure, B. Geothermal Technologies Program.

12. Raza, A., Gholami, R., Rezaee, R., Rasouli, V. & Rabiei, M. Significant aspects of carbon capture and storage – A review. *Petroleum* **5**, 335–340 (2019).

13. Patra, B. R., Mukherjee, A., Nanda, S. & Dalai, A. K. Biochar production, activation and adsorptive applications: a review. *Environ. Chem. Lett.* (2021) doi:10.1007/s10311-020-01165-9.

14. Patra, B. R., Nanda, S., Dalai, A. K. & Meda, V. Chemosphere Taguchi-based process optimization for activation of agro-food waste biochar and performance test for dye adsorption. *Chemosphere* **285**, 131531 (2021).

15. Zhou, T., Shi, H., Ding, X. & Zhou, Y. Thermodynamic modeling and rational design of ionic liquids for pre-combustion carbon capture. *Chem. Eng. Sci.* **229**, 116076 (2021).

16. Sifat, N. S. & Haseli, Y. A critical review of CO2 capture technologies and prospects for clean power generation. *Energies* **12**, (2019).

17. González-nicolás, A. *et al.* International Journal of Greenhouse Gas Control Pressure management via brine extraction in geological CO 2 storage : Adaptive optimization strategies under poorly characterized reservoir conditions. *Int. J. Greenh. Gas Control* **83**, 176–185 (2019).

18. Jing, Y. *et al.* An image-based coal network model for simulating hydro-mechanical gas flow in coal : An application to carbon dioxide geo-sequestration. *J. Clean. Prod.* **379**, 134647 (2022).

19. Zhao, X., Liao, X. & He, L. The evaluation methods for CO 2 storage in coal beds , in China. *J. Energy Inst.* **89**, 389–399 (2016).

20. Shabani, B. & Vilc, J. Computers and Geosciences A fast and robust TOUGH2 module to simulate geological CO 2 storage in saline aquifers.

111, 58–66 (2018).

21. Chen, B., Harp, D. R., Lin, Y., Keating, E. H. & Pawar, R. J. Geologic CO 2 sequestration monitoring design : A machine learning and uncertainty quantification based approach. **225**, 332–345 (2018).

22. Agartan, E., Gaddipati, M., Yip, Y., Savage, B. & Ozgen, C. International Journal of Greenhouse Gas Control CO 2 storage in depleted oil and gas fields in the Gulf of Mexico. *Int. J. Greenh. Gas Control* **72**, 38–48 (2018).

23. Zhu, D. D., Liu, J. L. & Qiao, S. Z. Recent Advances in Inorganic Heterogeneous Electrocatalysts for Reduction of Carbon Dioxide. 3423–3452 (2016) doi:10.1002/adma.201504766.

24. Ruiz-López, E., Gandara-Loe, J., Baena-Moreno, F., Reina, T. R. & Odriozola, J. A. Electrocatalytic CO2 conversion to C2 products: Catalysts design, market perspectives and techno-economic aspects. *Renew. Sustain. Energy Rev.* **161**, (2022).

25. Marepally, B. C. *et al.* Role of small Cu nanoparticles in the behaviour of nanocarbon-based electrodes for the electrocatalytic reduction of CO2. *J. CO2 Util.* **21**, 534–542 (2017).

26. Abdel-Mageed, A. M. & Wohlrab, S. Review of CO2 reduction on supported metals (Alloys) and single-atom catalysts (SACs) for the use of green hydrogen in power-to-gas concepts. *Catalysts* **12**, (2022).

27. Habisreutinger, S. N., Schmidt-mende, L. & Stolarczyk, J. K. Photocatalytic Reduction of CO 2 on TiO 2 and Other Semiconductors Angewandte. 7372–7408 (2013) doi:10.1002/anie.201207199.

28. Klankermayer, J., Wesselbaum, S. & Beydoun, K. Selective Catalytic Synthesis Using the Combination of Carbon Dioxide and Hydrogen : Catalytic Chess at the Interface of Energy and Chemistry Angewandte.

7296–7343 (2016) doi:10.1002/anie.201507458.

29. Snoeckx, R. & Bogaerts, A. Plasma technology-a novel solution for CO2 conversion? *Chem. Soc. Rev.* **46**, 5805–5863 (2017).

30. Kar, S., Goeppert, A. & Prakash, G. K. S. Catalytic Homogeneous Hydrogenation of CO2 to Methanol. *Co* 89–112 (2021) doi:10.1002/9783527824113.ch4.

31. Li, K., Peng, B. & Peng, T. Recent Advances in Heterogeneous Photocatalytic CO 2 Conversion to Solar Fuels. (2016) doi:10.1021/acscatal.6b02089.

32. Tomboc, G. M., Choi, S., Kwon, T., Hwang, Y. J. & Lee, K. Potential Link between Cu Surface and Selective CO 2 Electroreduction : Perspective on Future Electrocatalyst Designs. **1908398**, 1–23 (2020).

33. Kamkeng, A. D. N., Wang, M., Hu, J., Du, W. & Qian, F. Transformation technologies for CO 2 utilisation : Current status , challenges and future prospects. *Chem. Eng. J.* **409**, 128138 (2021).

34. Grills, D. C. *et al.* Electrocatalytic CO 2 Reduction with a Homogeneous Catalyst in Ionic Liquid: High Catalytic Activity at Low Overpotential. 1–6 (2014).

35. Xie, H., Wang, T., Liang, J., Li, Q. & Sun, S. Nano Today Cu-based nanocatalysts for electrochemical reduction of CO 2. *Nano Today* **21**, 41–54 (2018).

36. Lund, H. A Century of Organic Electrochemistry. *J. Electrochem. Soc.* **149**, S21 (2002).

37. Moeller, K. D. Using Physical Organic Chemistry to Shape the Course of Electrochemical Reactions. *Chem. Rev.* **118**, 4817–4833 (2018).

38. Francke, R. & Little, R. D. Redox catalysis in organic electrosynthesis:

Basic principles and recent developments. *Chem. Soc. Rev.* **43**, 2492–2521 (2014).

39. Dai, Y., Wang, Y., Liu, B. & Yang, Y. Metallic nanocatalysis: An accelerating seamless integration with nanotechnology. *Small* **11**, 268–289 (2015).

40. Yin, Z., Palmore, G. T. R. & Sun, S. Electrochemical Reduction of CO2 Catalyzed by Metal Nanocatalysts. *Trends Chem.* **1**, 739–750 (2019).

41. Zhu, J., Hu, L., Zhao, P., Lee, L. Y. S. & Wong, K. Y. Recent Advances in Electrocatalytic Hydrogen Evolution Using Nanoparticles. *Chem. Rev.* **120**, 851–918 (2020).

42. Wu, T., Han, M. Y. & Xu, Z. J. Size Effects of Electrocatalysts: More Than a Variation of Surface Area. *ACS Nano* **16**, 8531–8539 (2022).

43. Liu, Y., Wang, Y., Zhao, S. & Tang, Z. Metal–Organic Framework-Based Nanomaterials for Electrocatalytic Oxygen Evolution. *Small Methods* **6**, 1–28 (2022).

44. Zhu, C. & Dong, S. Recent progress in graphene-based nanomaterials as advanced electrocatalysts towards oxygen reduction reaction. *Nanoscale* **5**, 1753–1767 (2013).

45. Maity, D., Sahoo, S. R. & Saha, S. Synthesis and Characterization of Nanomaterials for Electrochemical Sensors. *ACS Symp. Ser.* **1437**, 193–222 (2023).

46. Verma, J. & Goel, S. Cost-effective electrocatalysts for Hydrogen Evolution Reactions (HER): Challenges and Prospects. *Int. J. Hydrogen Energy* **47**, 38964–38982 (2022).

47. Xu, Y. *et al.* Multi-field driven hybrid catalysts for CO2 reduction: Progress, mechanism and perspective. *Mater. Today* **54**, 225–246 (2022).

48. Hu, X. & Yip, A. C. K. Heterogeneous Catalysis: Enabling a Sustainable Future. *Front. Catal.* **1**, 1–5 (2021).

49. Sun, R. *et al.* Heterogeneous catalysts for CO2hydrogenation to formic acid/formate: From nanoscale to single atom. *Energy Environ. Sci.* **14**, 1247–1285 (2021).

50. Frontera, P., Macario, A., Ferraro, M. & Antonucci, P. L. Supported catalysts for CO2 methanation: A review. *Catalysts* **7**, 1–28 (2017).

51. Ashok, J. *et al.* A review of recent catalyst advances in CO2 methanation processes. *Catal. Today* **356**, 471–489 (2020).

52. Chen, X. *et al.* Recent Advances in Supported Metal Catalysts and Oxide Catalysts for the Reverse Water-Gas Shift Reaction. *Front. Chem.* **8**, 1–21 (2020).

53. Jiang, X., Nie, X., Guo, X., Song, C. & Chen, J. G. Recent Advances in Carbon Dioxide Hydrogenation to Methanol via Heterogeneous Catalysis. *Chem. Rev.* **120**, 7984–8034 (2020).

54. Yang, H. *et al.* A review of the catalytic hydrogenation of carbon dioxide into value-added hydrocarbons. *Catal. Sci. Technol.* **7**, 4580–4598 (2017).

55. Gao, J., Jia, C. & Liu, B. Direct and selective hydrogenation of CO2 to ethylene and propene by bifunctional catalysts. *Catal. Sci. Technol.* **7**, 5602–5607 (2017).

56. Küngas, R. Review—Electrochemical CO 2 Reduction for CO Production: Comparison of Low- and High-Temperature Electrolysis Technologies . *J. Electrochem. Soc.* **167**, 044508 (2020).

57. Duarah, P., Haldar, D., Yadav, V. S. K. & Purkait, M. K. Progress in the electrochemical reduction of CO2 to formic acid: A review on current trends and future prospects. *J. Environ. Chem. Eng.* **9**, 106394 (2021).

58. Pan, H. & Barile, C. J. Electrochemical CO2reduction to methane with remarkably high Faradaic efficiency in the presence of a proton permeable membrane. *Energy Environ. Sci.* **13**, 3567–3578 (2020).

59. Yang, D. *et al.* Selective electroreduction of carbon dioxide to methanol on copper selenide nanocatalysts. *Nat. Commun.* **10**, 1–9 (2019).

60. Zhang, W. *et al.* Atypical Oxygen-Bearing Copper Boosts Ethylene Selectivity toward Electrocatalytic CO2Reduction. *J. Am. Chem. Soc.* **142**, 11417–11427 (2020).

61. Nitopi, S. *et al.* Progress and Perspectives of Electrochemical CO2 Reduction on Copper in Aqueous Electrolyte. *Chem. Rev.* **119**, 7610–7672 (2019).

62. Gao, J. *et al.* Electrochemical synthesis of propylene from carbon dioxide on copper nanocrystals. *Nat. Chem.* **15**, 705–713 (2023).

63. Chang, B. *et al.* Electrochemical reduction of carbon dioxide to multicarbon (C2+) products: challenges and perspectives. *Energy Environ. Sci.* **16**, (2023).

64. Sancho-Sanz, I., Korili, S. A. & Gil, A. Catalytic valorization of CO2 by hydrogenation: current status and future trends. *Catal. Rev. - Sci. Eng.* **65**, 698–772 (2023).

65. Ye, R. P. *et al.* CO2 hydrogenation to high-value products via heterogeneous catalysis. *Nat. Commun.* **10**, (2019).

66. Lim, R. J. *et al.* A review on the electrochemical reduction of CO2 in fuel cells, metal electrodes and molecular catalysts. *Catal. Today* **233**, 169–180 (2014).

67. Long, C. *et al.* Electrochemical Reduction of CO2 over Heterogeneous Catalysts in Aqueous Solution: Recent Progress and Perspectives. *Small*

Methods **3**, 1–20 (2019).

68. Lei, Y. *et al.* Recent advances on electrocatalytic CO2 reduction to resources: Target products, reaction pathways and typical catalysts. *Chem. Eng. J.* **453**, 139663 (2023).

69. Fortunato, G. V. *et al.* Analysing the relationship between the fields of thermo- and electrocatalysis taking hydrogen peroxide as a case study. *Nat. Commun.* **13**, 1–7 (2022).

70. Jia, C., Gao, J., Dai, Y., Zhang, J. & Yang, Y. The thermodynamics analysis and experimental validation for complicated systems in CO2 hydrogenation process. *J. Energy Chem.* **25**, 1027–1037 (2016).

71. Bligaard, T. *et al.* The Brønsted-Evans-Polanyi relation and the volcano curve in heterogeneous catalysis. *J. Catal.* **224**, 206–217 (2004).

72. Zhao, Y. *et al.* Conversion of CO2 to multicarbon products in strong acid by controlling the catalyst microenvironment. *Nat. Synth.* **2**, 403–412 (2023).

CHAPTER 2

2.1 Electrocatalytic hydrogenation of CO_2

Electrochemical CO_2 reduction has gained popularity due to its numerous potential applications in the energy and chemical sectors, creating value-added fuels and chemicals under moderate circumstances and in a carbon-neutral manner[1,2]. The electrochemical reduction of CO_2 enables for fine-tuning of the selectivity of the value-added products[3].

Direct electro-reduction of CO_2 into hydrocarbons, oxygenates or CO is appealing due to (1) environmental compatibility with carbon-free renewable energy resources (solar, tides, and wind), (2) operating at ambient temperature and pressure, (3) reaction control by modifying parameters including electrolytes and applied voltages, and (4) engineering and economic feasibility.

Without a doubt, the largest problem of the CO_2 reduction is the chemical stability of the molecule. To overcome its energy barriers, it needs the application of stronger negative potentials that are near to the water reduction equilibrium potential in order to reduce it electrochemically. In fact, the initial step in the electrochemical reduction of a CO_2 molecule is the use of a large overpotential. The main reason is the production of CO_2^{*-}, a radical intermediate via single-electron transfer ($E = -1.9$ V vs. SHE). It is regarded the rate-determining step on most transition metal-based catalysts [4,5]. Furthermore, aqueous electrocatalytic CO_2 reduction is particularly difficult due to the competing proton reduction ($2e^-$ transfer), which results in low selectivity for carbonaceous products. Another concern is the poor CO_2 solubility in water (0.034 M), which has a negative impact on diffusion-controlled processes.

This chapter is based on:

Miah, T., Demoro, P., Nduka, I., De Luca, F., Abate, S., Arrigo, R.
Orange-Peel Biomass-derived Carbon Supported Cu Electrocatalysts Active in the CO_2-Reduction to Formic Acid, ChemPhysChem **202200589**, (2023). doi.org/10.1002/cphc.202200589

Catalytic techniques have therefore been created to avoid CO_2^{*-} generation, reducing CO_2 at reduced energy costs via proton-assisted multiple-electron transfer. CO_2 may be reduced to 10 distinct compounds depending on the number of electrons and protons transferred (figure 2.1).

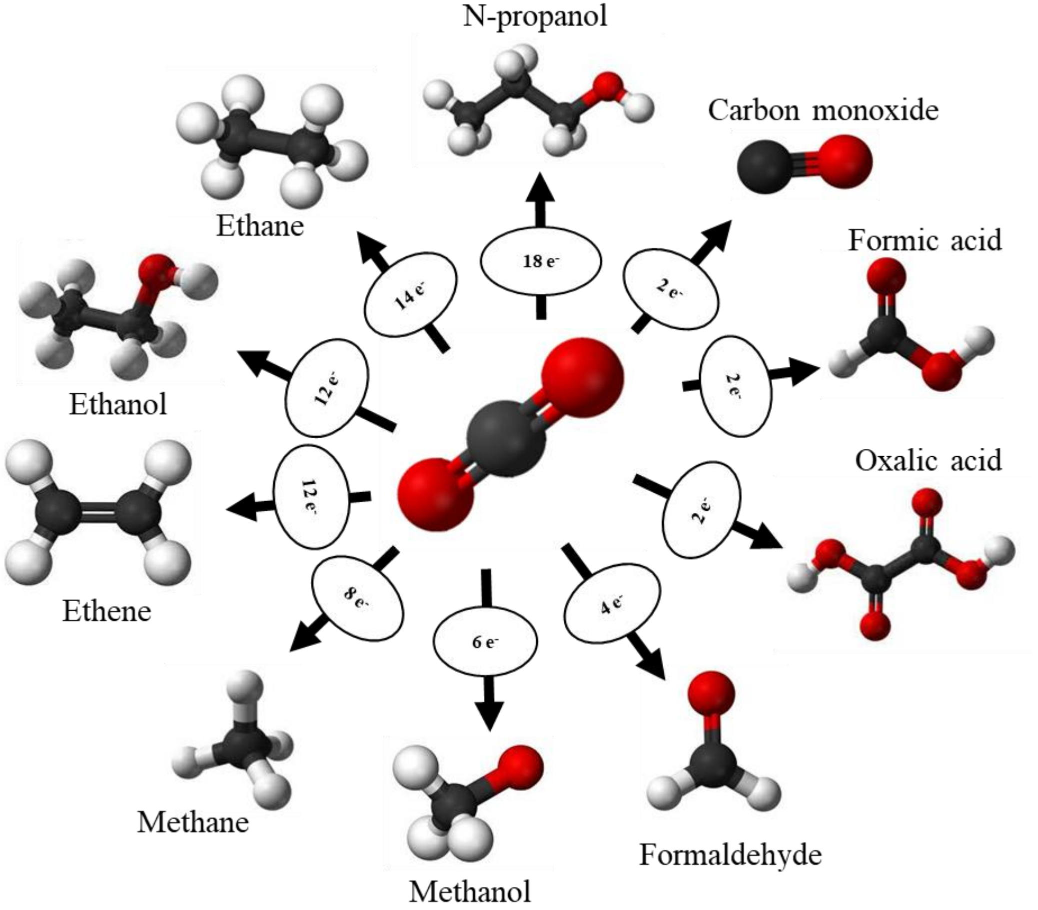

Figure 2.1: Main products from electrochemical reduction of CO_2 depending on the number of electrons and protons transferred.

Heterogeneous electrochemical CO_2 reduction takes place at electrode-electrolyte interfaces. When modeling these heterogeneous catalytic processes, three phases are primarily considered (figure 2.2):

- CO_2 adsorption chemically on the surface of a catalyst (cathode).
- Electron and/or proton transfers leading to C-H, C-O bonds, or C-C coupling.
- Product species rearrangement, followed by desorption from the electrode surface and diffusion into the electrolyte [4,6,7].

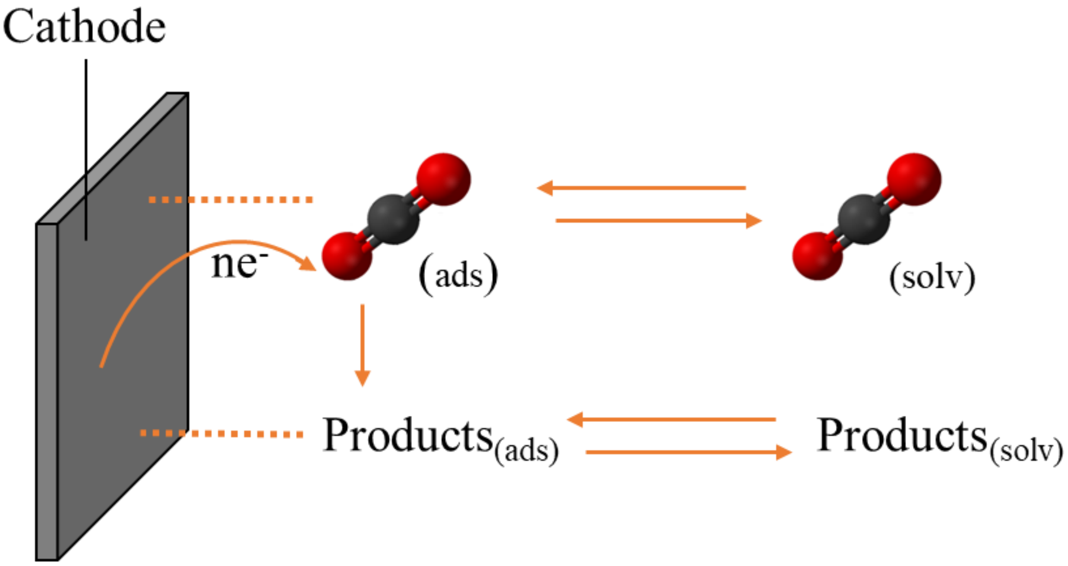

Figure 2.2: Scheme for CO_2 reduction by a heterogeneous catalyst in an electrochemical film.

The effects of parameters such as electrocatalyst type (size, composition, shape, crystallographic structure, and oxidation state), electrolytes (cation, anion, pH, and concentration), pressure, temperature, and applied potential can make a reaction more or less easy, resulting in a specific product being selective.

Typically, a reduction reaction with a more positive E^0 is thermodynamically more favorable according to the relationship:

$$\Delta G = - nFE^0 \quad \text{(eq. 2.1)}$$

Where:

n is the number of electrons transferred during the redox reaction;
F is the Faraday constant;
E^0 is the standard potential.

CO_2 reduction, in addition to a thermodynamic barrier, has a kinetic dependence on the concentration of available protons in solution. This means that a catalyst, thanks to its catalytic sites, makes it easier to transfer electrons that are close to sites providing protons. Therefore, the electrocatalyst has a substantial influence on the reaction paths and the product distributions. In literature, noble metals (Ag, Au, and Pd)[8–10], have been reported to be highly selective catalysts for C_1 products such as CO and HCOOH, whereas Cu-based catalysts have demonstrated activity towards more than $2e^-$ products such as methanol and methane[11,12]. Aside from selecting a selective electrocatalyst, the product distribution may be altered by adjusting external parameters such as electrode properties (surface, morphology, facets, etc.), operating circumstances (applied overpotential, electrolyte, anodic reaction), or cell design itself.

Also, in electrocatalysis, another crucial point is electricity. It plays a key role, because in the profitability of the CO_2 conversion it is the main factor in the operational costs[13,14]. One of the advantages of the electrochemical CO_2 reduction reaction is that it can be considered as an efficient way to store electrical green energy as transportable chemicals and fuels.

Due to the availability of renewable energy, the electrochemical reduction of CO_2 is justified in terms of the environment. In this way, extra electricity from wind or solar light may be utilized to reduce the CO_2 molecule, allowing it to be used as a chemical or fuel. In this manner, CO_2 serves as a storage of energy.

Thanks to its many potential applications in the energy and chemical sectors including the production of value-added fuels and chemicals, shown in figure 2.1, under moderate conditions and in a carbon-neutral manner [1,2,15], electrochemical reduction of CO_2 has attracted increasing interest. In fact, it is a valid candidate for large-scale carbon management applications because it can operate with good efficiency and high reaction rates at ambient conditions[16–19].

2.2 Electrochemical cell setup

Typically, an electrocatalytic reactor is a three electrodes set-up electrochemical cell that consists of [20]:

- **Working electrode**: it plays an essential role in the electrochemical reaction of interest. In an electrochemical cell, it provides the site for either the oxidation (anode) or reduction (cathode) half-reaction. During an experiment, a potential is applied to the working electrode, which drives the electrochemical reaction. The resulting current is monitored to better understand the kinetics and thermodynamics of the reaction. In some circumstances, catalysts may be added to the working electrode to improve reaction rate, selectivity, or sensitivity.
- **Reference electrode:** it is used to have a known and steady electrochemical potential against which the working electrode potential is measured. Maintaining a constant potential allows accurate control and measurement of the potential applied to the working electrode. There are various types of reference electrodes, including the standard hydrogen electrode (SHE), the silver/silver chloride electrode (Ag/AgCl) and the calomel electrode (Saturated Calomel Electrode or SCE). A key feature of a reference electrode is its stability because it should maintain a constant potential under the conditions of the experiment. This stability is crucial for accurate electrochemical measurements.
- **Counter electrode:** it is responsible for completing the electrical circuit in an electrochemical cell. It generates a way for electricity to flow, allowing oxidation or reduction processes to take place at the working electrode. It

basically balances the charge within the cell. Counter electrodes tend to be made of conductive materials such as platinum, gold, graphite, or other highly conductive materials. The counter electrode is often inert, which means it does not participate in the electrochemical processes occurring in the cell. Because of their inert character, the reactions are centered on the working electrode.

The three electrodes are submerged in an electrolyte solution. The latter is essential in electrochemical cells. It is significant for various reasons, for example[20]:

- **Ion transport:** ions are needed to complete the circuit and maintain charge balance. Thus, it is essential for the flow of charge and the overall functioning of the cell.
- **Conductivity:** electrolyte solutions are conductive, allowing for the movement of charge and as consequence generating electrical current.
- **Electrode Reactions:** electrochemical processes involve redox reactions, where one electrode loses electrons, and the other gains them. Electrolyte solutions provide a medium for the transfer of electrons between the electrodes.
- **Electrolyte Selectivity:** the choice of electrolyte can also impact the selectivity of the electrochemical reactions. Specific ions can enhance or suppress certain reactions, which is crucial in electrochemical applications.

Besides, to keep the anodic and cathodic compartments separated, a selective exchange membrane is used. Typically, in the reduction reactions of CO_2 or its intermediates, a cation exchange membrane (CEM) is employed to allow the moving of protons from the anodic side to the cathodic compartment. The membrane selectivity is an advantageous property because it prevents crossover and maintains charge separation[21]. It can enhance the cell efficiency because it avoids the mixing of substrate and oxidating gases in the cathodic compartment.

Finally, it is resistant to a wide range of chemicals, which is vital for its use in various chemical processes and electrochemical applications[22].

After considering generic notions, depicted in figure 2.3, the three-electrode setup electrochemical cell, where the experiments take place, is presented.

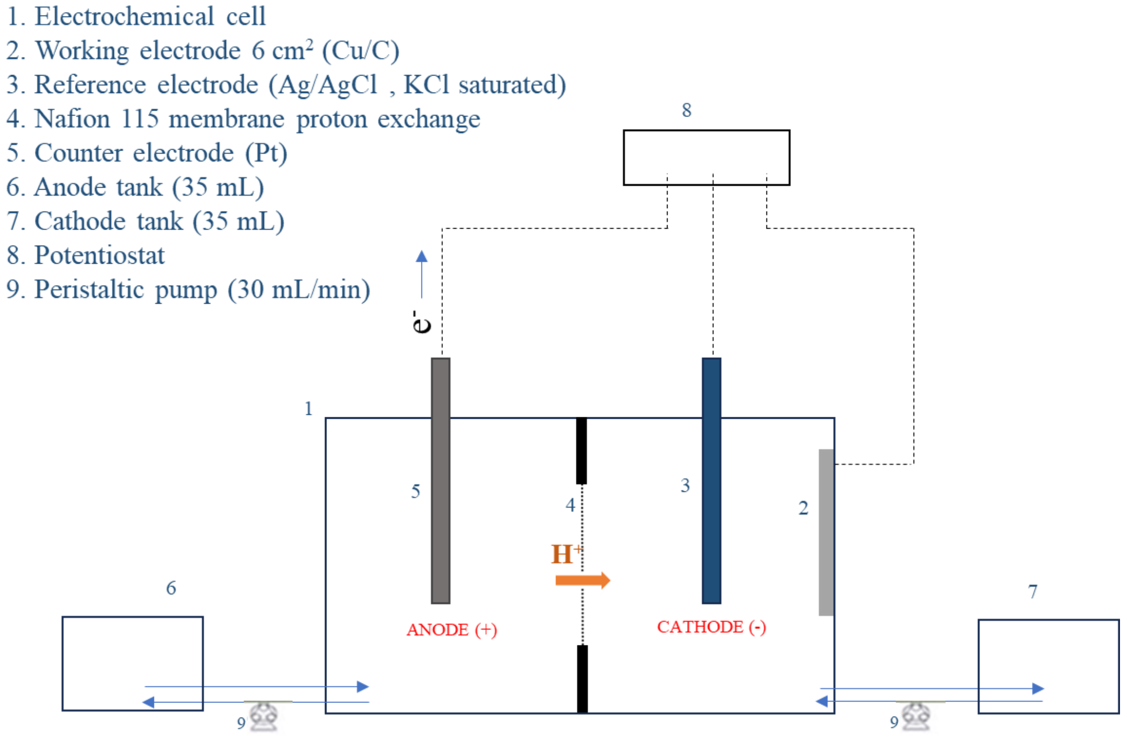

Figure 2.3: Experimental three electrodes set-up electrochemical cell.

The electrocatalytic cell is divided into two compartments: (1) anodic and (2) cathodic with the (4) proton-exchange membrane (Nafion® 115) acting as the partition. Because reduction reactions were investigated, in the cathode tank (7), the working electrode (2) was collocated. The electrolytic solutions are flushed to both the compartments by using a peristaltic pump (9). The solution volume (cathode + external tank + tubes) is 35 ml and the net volume in the cathodic compartment is 7 ml, the same as in the anode.

2.3 CO_2 reduction reaction

The electrode potential is a fundamental concept in understanding redox processes and hence electrochemical cells. The cell potential is a measure of the spontaneity of a redox reaction based on this potential difference. The cell potential is defined as the difference between the reduction potential of the cathode and the oxidation potential of the anode, which can be determined thermodynamically and is commonly tabulated for standard circumstances. By combining the reduction potentials of the two half-reactions, it is possible to calculate the cell standard potential (E°) of a redox reaction (eq. 2.2).

$$E^o_{cell} = E^o_{cathode} - E^o_{anode} \qquad \text{(eq. 2.2)}$$

Looking at the reactions related to CO_2 reduction, it is clear that the majority of redox reactions involve a negative cell potential and hence do not occur spontaneously. Normally, electrochemical processes do not occur at the theoretical value predicted by thermodynamics, and in electrolytic cells, the cathode potential must be more negative, requiring a higher energy than thermodynamics predicts. In the studied case, the main reduction reaction products are formic acid (FA), carbon monoxide, oxalic acid (OX), and methane, and the cell standard potential of these reactions are reported in table 2.1. The anodic reaction is the water oxidation (table 2.1) that provides electrons and protons that move to the cathode side through a cation exchange membrane, as shown in the electrochemical cell depicted in figure 2.3.

Table 2.1: Cell standard potential (E^o) of main reduction reaction products (formic acid, carbon monoxide and methane) at 25°C and 1 atm.

Anode		
Half- reaction	E^o_{anode} (V vs SHE)	
$2H_2O \rightarrow 4H^+ + 4e^- + O_2$	+ 1.23	
Cathode		
Half- reaction	$E^o_{cathode}$ (V vs SHE)	E^o_{cell} (V)
$CO_2(g) + 2H^+(aq) + 2\ e^- \rightarrow CO(g) + H_2O(l)$	- 0.106	- 1.34
$CO_2(g) + 2H^+(aq) + 2\ e^- \rightarrow HCOOH(l)$	- 0.199	- 1.43
$2CO_2(g) + 2H^+(aq) + 2\ e^- \rightarrow (HCOO)_2(l)$	- 0.475	- 1.70
$CO_2(g) + 8H^+(aq) + 8\ e^- \rightarrow CH_4(g) + H_2O(l)$	+ 0.169	- 1.06

2.4 Biomass-derived carbon electrocatalysts

Carbon is a chemical element that has gained a lot of interest because of its many dimensions, structures, textures, and other properties. Chemical bonding and hybridization are used to classify these properties, which include sp, sp^2, and sp^3 [23]. Activated charcoal, carbon black, carbon nanotubes (CNTs), graphite, fullerenes, and porous carbon nanostructures are examples of carbon materials. Because of their remarkable mechanical, physical, and electrical capabilities, as well as geometrical traits such as a small diameter and a high surface area[24], they offer a wide range of energy conversion and storage applications.

However, the growing need for energy sources, as well as their environmental consequences, are important driving forces in the development of sustainable energy conversion technologies. The cost and energy efficiency of electrochemical energy conversion materials are essential aspects of tackling the energy crisis and maintaining long-term sustainability. As sustainable, renewable, and efficient carbon-based electrode materials for key electrochemical applications, biomass-derived carbon compounds are extremely important. Vassilev et al.[25] define biomass as a non-fossil, complex, and biogenic heterogeneous mixture of organic and inorganic matter primarily generated by photosynthesis, such as natural constituents from water-based and land vegetation; and anthropogenic processing of plants, wood, and other organic matter, such as manure or household waste.

Based on the aforementioned considerations, a novel method for the synthesis of carbon materials, known as biochar carbon, has been produced through a thermal decomposition (like pyrolysis) of biomass. Biochar carbon is a very heterogeneous material whose elemental composition varies substantially depending on the food substrate[26]. Initially, biochar had been produced from sawdust, but progressively replaced with other elements of farm waste products to reuse the waste materials to help farmers. As a result, fruit peels, coconut husks, and other agricultural waste are used to generate biochar[27]. The availability of low-cost and environmentally friendly leftovers has heightened interest in using them as biochar feedstock. Furthermore, turning organic waste into biochar lowers the operating expenses associated with waste product disposal[28]. It is estimated that 500 t of agricultural waste is produced globally each year. Consequently, most of these resources, rarely used, might serve as a constant feedstock for biochar formation.

Thanks to this variety of biomass raw materials, high-ordered structures of carbonaceous materials with high surface areas and flexible porosity may be created. Consequently, biochar carbon is a promising candidate as a sustainable carbon material. Typically, biochar carbon is utilized as a supporting material and is crucial in maintaining the homogeneous dispersion of metal nanoparticles and providing more active sites for enhanced utilization[29]. The catalyst supports have a substantial influence on the performance, cost, and durability of anodic and cathodic half-cell electrode materials. Some of the most important characteristics of catalyst supports for improved electrocatalytic performance are (i) improved proton and electron conductivity; (ii) good thermal and mechanical stability; (iii) strong interaction with surface reaction; (iv) high electrochemical stability under operating conditions; and (v) a large surface area, which may be advantageous for achieving uniform dispersion of metal nanoparticles, resulting in increased efficiency.

Thanks to the diversity of carbon-based materials in terms of their chemical-physical properties and of most suited tailor-made capabilities to get efficient metal catalyst supports, this path will continue to be pursued in further research and development.

To summarize, the main biomass sources and their advantages and disadvantages[30] are listed in table 2.2.

Table 2.2: Biomass sources and their advantages and disadvantages for biochar production.

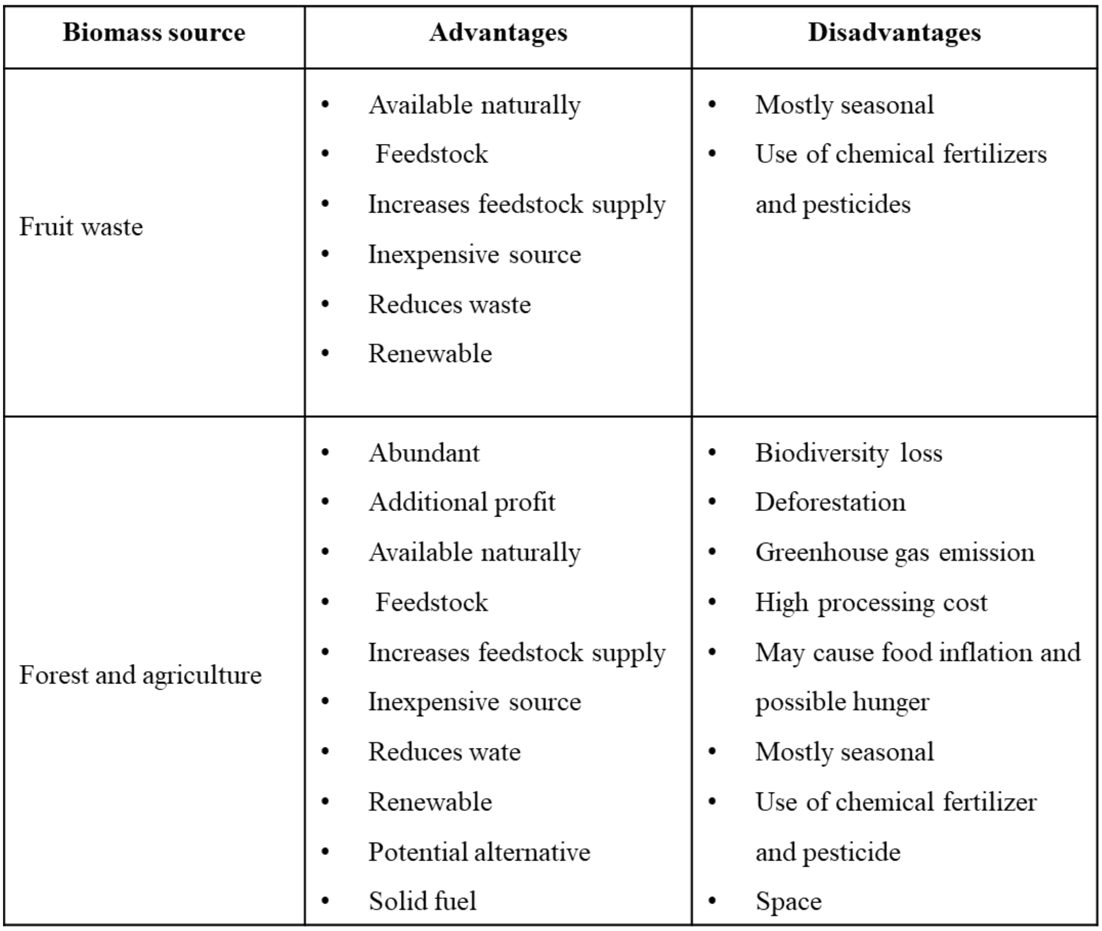

Biomass source	Advantages	Disadvantages
Fruit waste	• Available naturally • Feedstock • Increases feedstock supply • Inexpensive source • Reduces waste • Renewable	• Mostly seasonal • Use of chemical fertilizers and pesticides
Forest and agriculture	• Abundant • Additional profit • Available naturally • Feedstock • Increases feedstock supply • Inexpensive source • Reduces wate • Renewable • Potential alternative • Solid fuel	• Biodiversity loss • Deforestation • Greenhouse gas emission • High processing cost • May cause food inflation and possible hunger • Mostly seasonal • Use of chemical fertilizer and pesticide • Space

2.5 Cu-based catalyst for CO_2 reduction

The electrochemical reduction of CO_2 is an intriguing strategy for the production of value-added fuels or chemicals. Cu-based electrodes have been widely employed in the conversion of CO_2 to hydrocarbons.

Several Cu electrocatalysts have been produced and may be further divided: Cu compound (Cu^+ non-metal), Cu alloy, and supported Cu-based catalyst (Cu supported by metal oxides, carbon, or polymers) are all examples of Cu-based catalysts[31,32]. Despite significant increases in overall CO_2RR performance, Cu-based electrocatalyst provides a diverse range of products such as formic acid, carbon monoxide, methane, and ethylene[32]. Different factors, including chemical-physical properties (e.g., particle size, crystal facet, morphology, etc.), changes in oxidation states (Cu^0, Cu^+, Cu^{2+}), surface defects such as lattice distortion, phase changes, oxygen or copper vacancies, and grain boundaries have been reported to be responsible for modifying the catalytic activities of Cu-based electrocatalysts[4,33].

The electrocatalytic reduction of CO_2 by using citrus peel biomass-derived carbon supported Cu catalyst will be discussed. As widely reported in literature, carbonaceous materials are used in sustainable energy applications such as energy conversion and storage [34–38].

In the framework of a circular economy, the generation of carbonaceous materials from biomass[39] creates chances to raise the economic value of the waste[40]. For example, the worldwide citrus extract market was estimated at 5.6 billion USD in 2019, with a 4.2% annual growth rate predicted from 2020 to 2027. It is estimated that citrus waste would increase correspondingly to 50-60% of the worldwide citrus processing volume[40].

Nevertheless, the handling of citrus waste necessitates proper management due to the possible harmful environmental consequences of its chemical contents (organic matter, oils, and free acids). Citrus waste components, on the other hand, comprise chemical compounds with added value (e.g., essential oils, phenolic and flavonoids, pectin, and other fibers), which have prompted extensive study into their extraction[41].

Ascorbic acid, one of the chemical components found in citrus peel, is being employed as a reducing agent, as well as a capping agent in the manufacture of Cu nanoparticles active in CO_2 electroreduction[42,43]. Therefore, one of the goals of the discussion is to demonstrate the practicality of employing citrus waste directly in a synthesis of C-supported Cu nanoparticles using carbonaceous precursors naturally high in ascorbic acid. Thus, using orange peel directly has two advantages: i) it offers carbon support for the Cu nanoparticles, and ii) it supplies the ascorbic acid required for Cu reduction without the need to separate it from natural sources and use it as a reducing agent in the synthesis. Here will be demonstrated that the chemical nature of the biomass has an impact not only on the chemical speciation of the as-prepared electrocatalyst but also on its behavior and stability under reaction conditions. This indicates that biomass use is application-dependent and requires a reasonable strategy to be effective.

2.6 Synthesis of electrocatalysts

Citrus peel biomass-derived carbon supported Cu catalysts were synthesized by the following protocol: 3 g of $CuSO_4$ (anhydrous and 99.99% purity, Sigma Aldrich) were solubilized in 30 mL of distilled water at 50 °C. Commercial citrus peels (orange and lemon peel), were utilized. 0.65 g of finely ground citrus peel powder (lemon or orange) was suspended in 4 mL of $CuSO_4$ solution and diluted to 8 mL with distilled water in a microwave tube, which was then irradiated for 11 minutes at 68 °C by CEM Discover Microwave Reactor. After cooling for 2 minutes, the suspension was centrifuged at 1500 rpm for 8 minutes. The solid material was vacuum filtered and washed with distilled water and ethanol. In order to investigate the electrocatalytic performances, the catalysts were thermally treated in argon for 2 hours at 500 °C with a ramp rate of 5 °C/min with the goal to improve the graphitization of the carbonaceous support, which is required for electron conduction[44]. Then, in order to obtain an ink, 3 mg of as-prepared catalyst was dispersed in 8 μL of Nafion perfluorinated resin (aqueous dispersion10 wt%, Sigma Aldrich), and 300 μL of pure ethanol anhydrous (Carlo Erba) and sonicated for 2 hours. The produced ink was then spray coated onto SIGRACET GDL 28 BC (surface approximately 6 cm^2).

2.7 Characterization

The as-prepared samples are named Cu-L and Cu-O, where L stands for lemon peel and O for orange peel, respectively. To investigate the morphology of the sample, a Scanning electrons microscope (SEM) was utilized. In particular, a FEI Quanta FEG 250 SEM was used to analyze fresh samples, whereas after thermal treatment, the samples were characterized using a Phenom ProX Desktop instrument.

The SEM images (Figure 2.4 a-c), acquired in secondary electron (SE) mode, show the morphology of fresh Cu-O, which is characterized by deeply porous support, and uniformly decorated with round Cu nanoparticles ranging in size from 270 nm to 525 nm (average particle size determined by statistical analysis on the SEM images is 370±60 nm).

Figure 2.4 d shows a SEM image recorded in back-scattered electron (BSE) mode that allows us to identify the metal nanoparticles more precisely (brighter areas are owing to the heavier element, in this case Cu) and demonstrates that the particles are actually coated by an overlayer, most likely carbonaceous in origin.

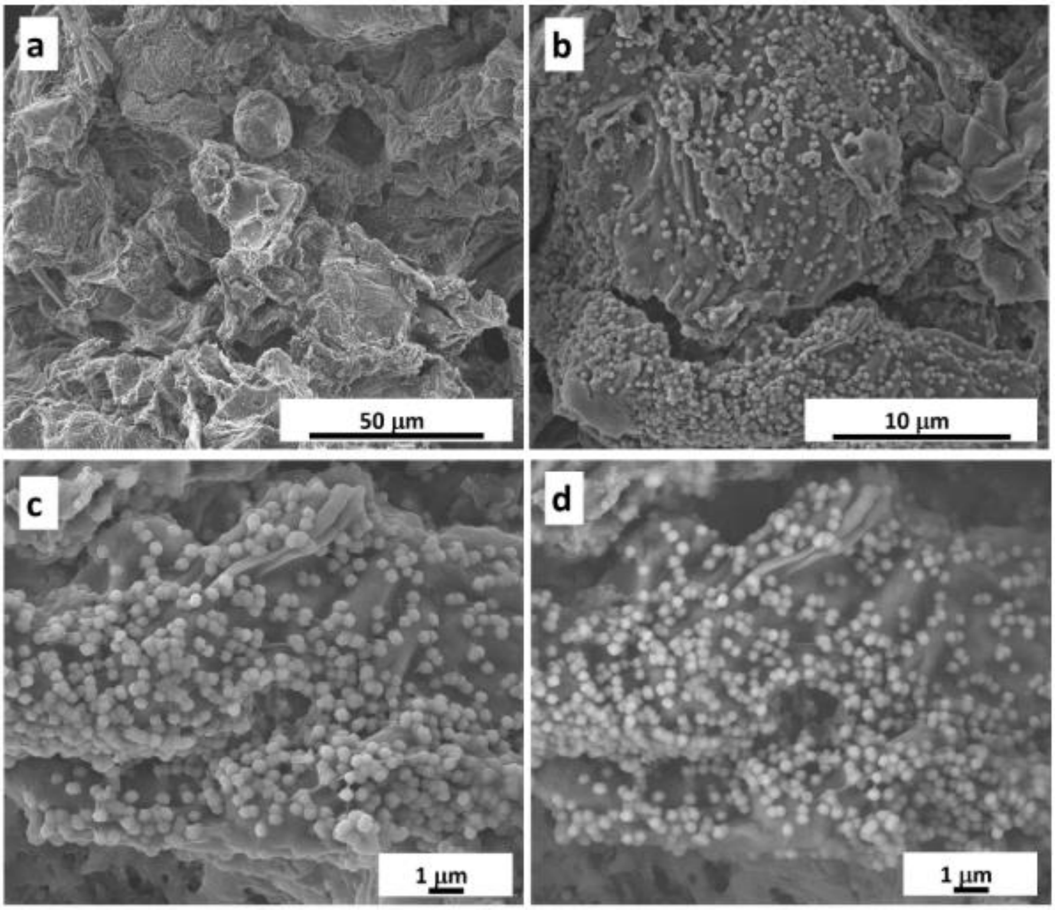

Figure 2.4: SEM images of fresh samples Cu-O acquired at different magnification. a) 2000× and b) 10000× c) 20000× in in secondary electron (SE) mode, and d) 20000× in back-scattered electron mode.

The Cu-L sample, on the other hand, is characterized mostly by unsupported big single crystals (such as the one in the upper left corner of Figure 2.5 a) or deposited crystals with a poorly defined morphology (Figure 2.5 b-d). The morphology of the big particles differs greatly between the two samples.

Large single crystals are detected for Cu-L, while the biggest particles observed for Cu-O are due to an aggregation of smaller crystallites, with a morphology clearly different from the rounder NPs in the same image. These agglomerates of small crystallites are also present in Cu-L, as seen in Figure 2.5 c-d.

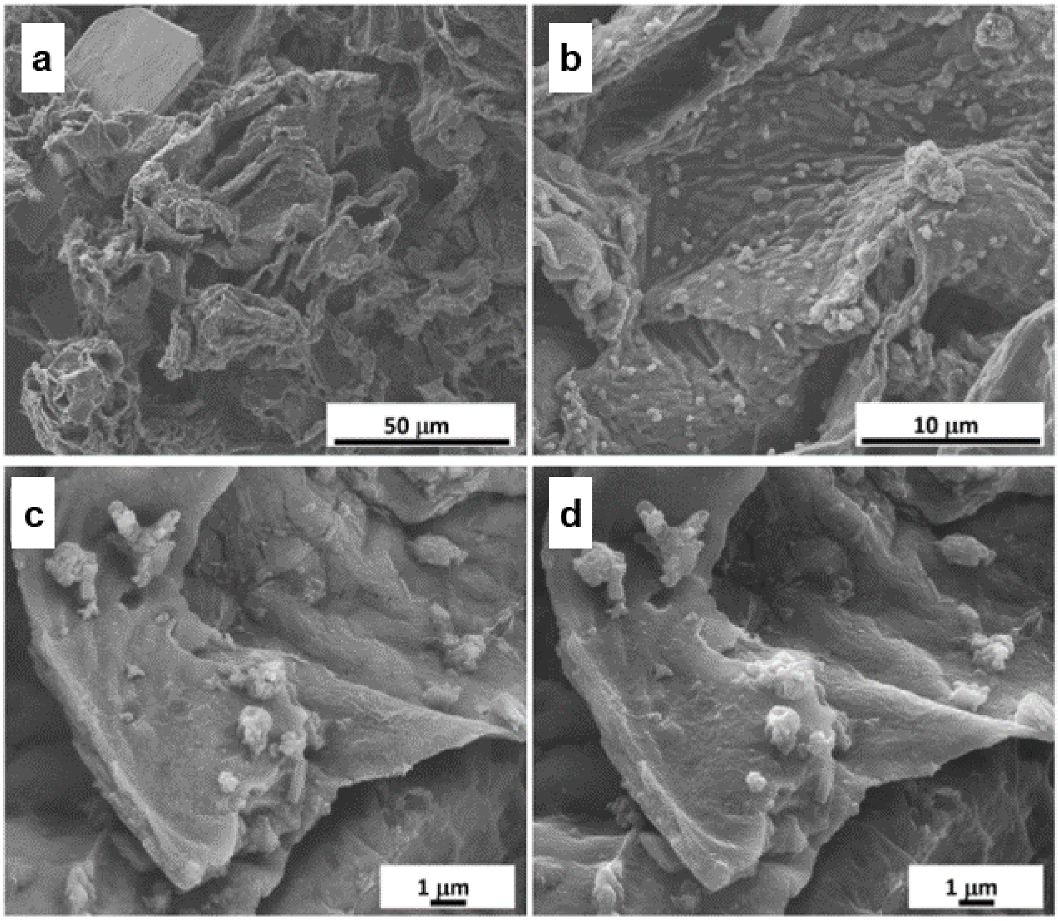

Figure 2.5: SEM images of fresh samples Cu-L acquired at different magnification. a) 2000× and b) 10000×; c) 20000× in SE mode and d) 20000× in BSE mode.

The Energy-dispersive X-ray spectroscopy (EDX) analysis in the highlighted area (green and red for Cu-L and Cu-O, respectively) in Figure 2.6 reveals that these particles include S, which might be the sulfate component seen in the Cu2p XPS spectra in figure 2.8. This is consistent with the finding that in Cu-O, only a limited number of those bigger particles are present, and no huge single crystals are observed as in Cu-L. Figure 2.6 depicts SEM images of large particles and also, they were investigated by EDX analysis.

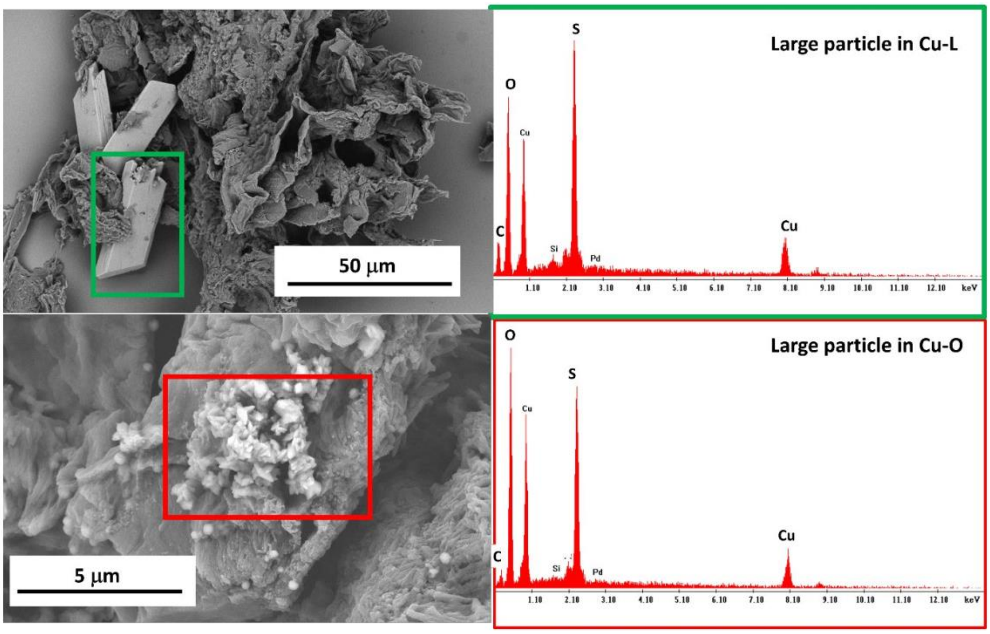

Figure 2.6: SEM images taken with varying magnifications for fresh Cu-L (top) and Cu-O (bottom) and EDX spectra of the area selected (green for Cu-L and red for Cu-O).

After thermal treatment, samples are named T-Cu-L and T-Cu-O, to indicate that the treatment has been carried out. These as-prepared samples are tested for the electrocatalytic reduction of CO_2, later discussed in the next section. Their SEM images (Figure 2.7) show an extended sintering of the Cu particles on both samples.

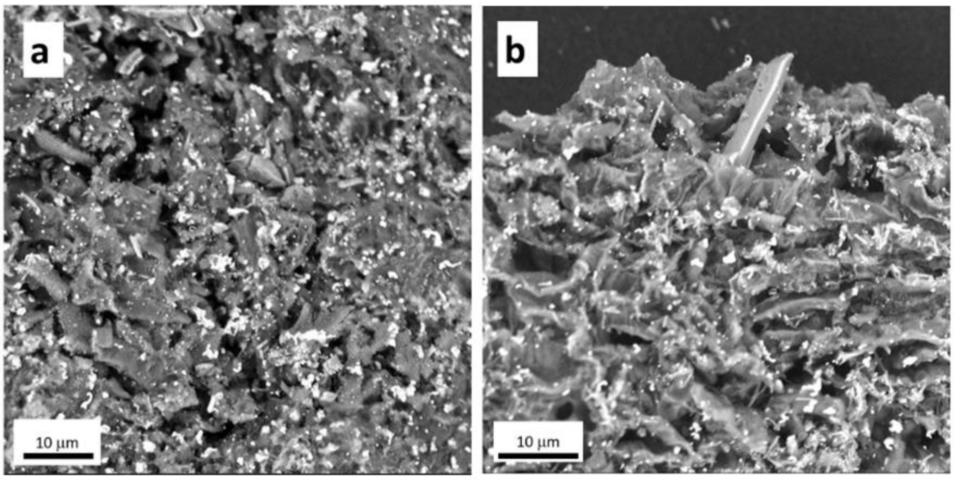

Figure 2.7: SEM in BSE mode: a) T-Cu-O at ×4000 magnification; b) T-Cu-L at ×4500 magnification.

However, smaller particles are kept on the T-Cu-O, demonstrating that the support has a significant effect on particle stability.

To obtain information about the surface chemical speciation, X-ray photoelectron spectroscopy (XPS) analysis was performed on the thermal treated samples in powder form by using PHI VersaProbe II (Physical Electronics), equipped with an Al Kα (1486.6 eV) X-ray source. The XPS analysis of the Cu-O, and Cu-L powder at the $Cu2p_{3/2}$, C1s and O1s core levels (Figure 2.8 a) is carried out.

The survey spectra reveal the surface chemical composition of the materials, which is mostly Cu, O, and C, with impurities such as N, Ca, and S. Table 2.3 shows the quantitative elemental analysis from the XPS data. As a result, the surface S and O content of the Cu-L samples is greater, which is compatible with sulfate species as shown in the Cu2p XPS spectra (Figure 2.8 b).

Table 2.3: XPS elemental analysis (%wt).

Sample	**C**	**N**	**O**	**S**	**Cu**
Cu-O	67.2	1.32	24.76	2.04	4.67
Cu-L	48.18	0.83	34.81	6.73	9.44
T-Cu-O	72.51	2.38	16.20	2.35	6.56
T-Cu-L	76.33	2.57	13.98	1.84	5.28

The experimental section describes the parameters used for fitting the high-resolution core level spectra. $Cu2p_{3/2}$ spectra of Cu-L and Cu-O were fitted using the model given in ref.[45,46] and include a component with a bonding energy (BE) of 933 eV (P2), which is intangibly higher than the value of bulk Cu_2O or Cu metal (Cu^0 at 932.6 eV and Cu_2O at 932.4 eV)[47].

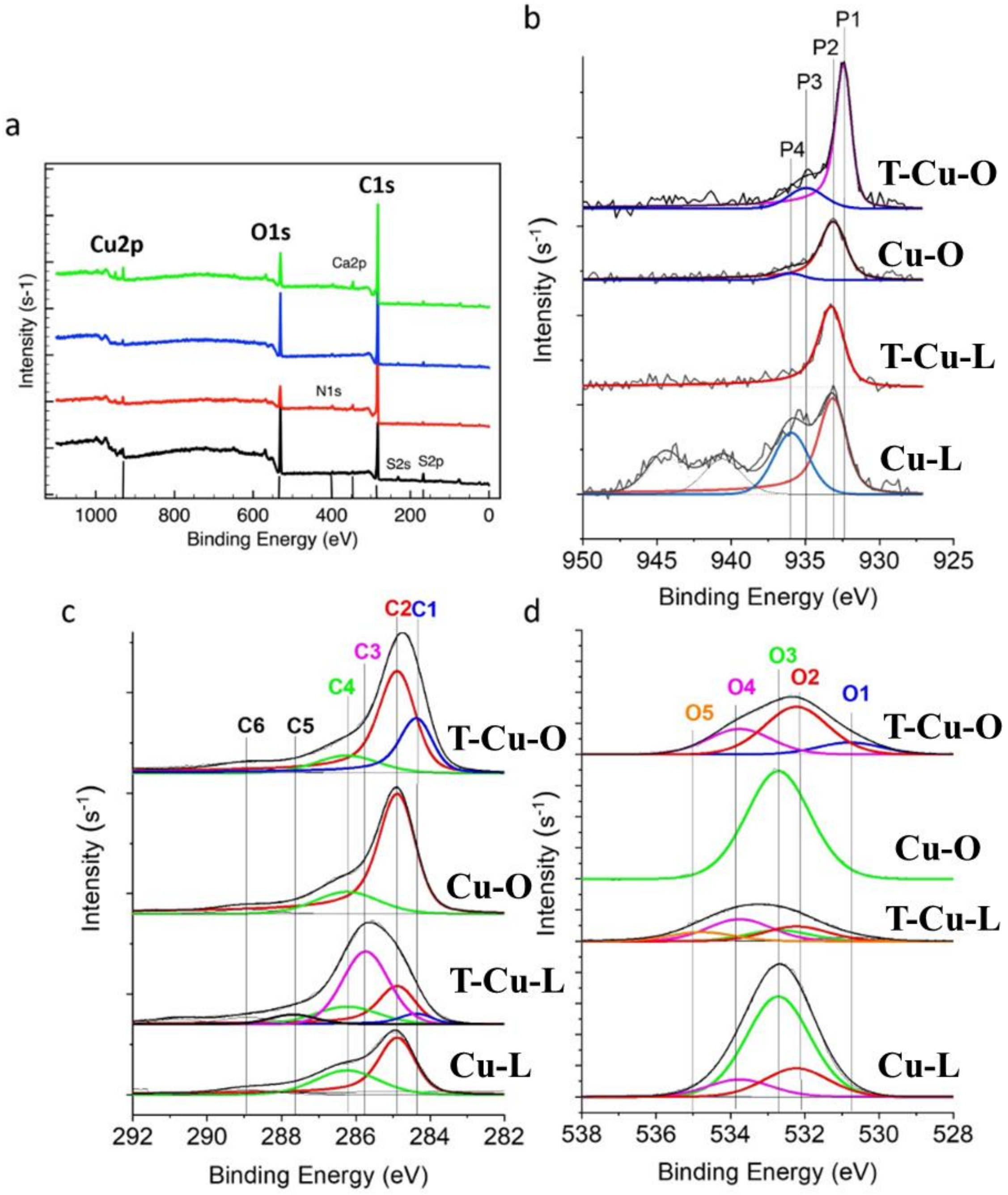

Figure 2.8: XPS analysis of fresh and thermal treated samples. For each spectrum from bottom to top: Cu-L; T-Cu-L; Cu-O; T-Cu-O. a) Survey spectra; b) Cu 2p$_{3/2}$; c) C1s; d) O1s.

A similar BE value was reported for Cu/Cu_2O core-shell nanoparticles on thin C films, with BE value for the Cu_2O shell from 932.3 eV to 933.8 eV[48] according to the metallic core size and the surface Cu/C ratio: the lower the BE, the larger the metallic core and the higher the surface Cu/C ratio. This phenomenon can be clarified by assuming that the XPS signal is dominated by the Cu/C interfaces, therefore a higher Cu abundance implies a thinner C overlayer, allowing for a greater volume of the nanoparticle to be probed, and as a result, the BE shifts to lower values closer to those expected for bulk Cu_2O or metallic Cu. It should be highlighted that the composition of metallic Cu and Cu_2O cannot be established via Cu2p spectra analysis, as the former is found at just 0.2 eV higher BE, which cannot be resolved with the XPS instrument precision, despite the fact that the nanoparticles in this study are fairly bulk from an XPS standpoint. Therefore, it may reasonably be concluded that a similar scenario exists here, with the P2 signal denoting a Cu_2O phase covered by a C overlayer. At 935.9 eV (P4) in the Cu2p spectra (Figure 2.8 b) a component, more abundantly on Cu-L, is assigned to Cu^{2+} and is accompanied by satellite peaks at around 941 eV and 944 eV, which is consistent with literature[45,46]. This species is thought to be connected to sulfate Cu species[49] produced from the precursor utilized (Cu(II) aqua-sulfate complex), which remained unreduced during Cu-L synthesis conditions and precipitated as unsupported particles during the centrifugation process. The C1s spectra may be used to determine the nature of the C support in as-synthesized materials (Figure 2.8 c).

By using the fitting described by Arrigo et al.[50], two major components are discovered: C2 (red component at around 284.8 eV) and C4 (green component at about 286.2 eV). At 288.9 eV, an additional minor component (C6) is discovered. The samples differ in C speciation, as evidenced by the relative ratio of C2 to C4. The C2 component is attributed to the occurrence of sp3 C-C species bound to an aromatic ring and, more broadly, to highly disordered graphite with a greater contribution from C in a sp^3 bonding environment [50]; the formation occurs during the hydrothermal synthesis because of the deoxygenation of aliphatic fragments of the lignin and cellulose components naturally present in the citrus peel. The C4 component, the most intense in the C1 spectrum of cellulose [51], is correlated to C-O species, namely methoxy species [46]. Hence, it is correct to conclude that in the sample Cu-L, most of the initial peel stays unmodified after the hydrothermal synthesis. Finally, the C6 component is generally attributed to carbonates [46].

For ease, the O1s spectrum of Cu-O, in Figure 2.8 d, was perfectly matched with the component at 532.7 eV (O3); nevertheless, it has to be noted that this peak should contain contributions from both the oxygen species on the Cu(I)-O particles (expected in the low binding energy region of the peak) and the O species on the C support. Also, Cu-L shows the O2 component at around 532.2 eV and the O4 component at 533.7 eV; the former is ascribed to oxygen species in S-O or C-O species[46,52], and the latter to COO-derived species on the support[46], which is consistent with the oxidized species found in the Cu2p and C1s XPS spectra. These results are interesting because they suggest the chemical composition of the used peel influences the chemical speciation in the sample of both the Cu nanostructures and the support, which influences the electrocatalytic properties of these materials. This behavior is intuitively attributed to the larger content of ascorbic acid in orange peel than in lemon peel, as documented in the literature[53].

The thermal treatment causes structural changes that differ greatly between the two samples, indicating the importance of the chemical character of the citrus waste utilized. Firstly, it can be seen that the O content decreases for both samples (Cu2p XPS in Figure 2.8 b), and for the lemon peel-derived system it is more pronounced due to the decomposition of the Cu sulfate species, and even for more acidic and thus more thermolabile oxygenated functional groups on C[46], such as species containing C-O single bonds.

The N concentration for both lemon- and orange-derived systems is now relatively comparable, although the Cu changes seemingly for both samples. It should be pointed out that XPS is a surface-sensitive technique with a depth of probing of approximately 5 nm in Cu2p measurements (KE 560 eV)[50], and thus an increase in particle size (thus reducing metal dispersion) or a raise in the thickness of a C overlayer may result in an apparent decrease in metal content[54].

For the thermal treated samples, the $Cu2p_{3/2}$ XPS spectrum of T-Cu- L illustrates only the P2 component, which was previously ascribed to Cu(I) species in Cu_2O. Instead, the C1 spectrum reveals the following extra components: C1 component at 284.3 eV due to sp^2 graphitic carbon; C3 component at 285.7 eV owing to sp^3 C (-CH3) in amorphous carbon; C5 component at 287.7 eV due to C-O species[46,50]. This finding, as predicted, implies deoxygenation/dehydrogenation of the C support, which is consistent with the considerable decrease in the abundance of the O species revealed in the O1s spectrum. The extra O5 species at 535 eV is typically observed on C materials, particularly after thermal treatment. The apparent increase in metal loading in T-Cu-O, on the other hand, can be explained by a higher weight of Cu in the overall composition due to thermolabile species desorption, or by a reduction in the thickness of the surface C overlayer with no significant change in particle size distribution.

The reduction is more effective for T-Cu-O, which now has a dominant component in the Cu $2p_{3/2}$ XPS spectrum (P1 at 932.4 eV) and a minority of Cu(II)-OH[49] species (P3 at 934.9 eV), which is consistent with the appearance of an O1 component in the O1s spectrum for this sample. The P1 component is 0.6 eV lower in binding energy than the P2 component, indicating that the shell of the nanoparticle is still Cu_2O, but the metallic core has expanded in size due to thermal annealing[48]. The graphitization of the carbon support (C1 component in blue) is more apparent in the Cu-O C1s spectrum.

Also, infrared spectroscopy (IR) was used to analyze the variations in the chemical compositions of Cu-O and Cu-L samples from precursor (Figure 2.9). Figure 2.9 shows the IR spectra of the samples, which indicate substantial variations in the carbonaceous support of the two samples. Only Cu-L has a bending vibration of

CH/CH_2 at 882 cm^{-1} in non-substituted benzene or alkene. This sample has a stretching vibration for CH in alkanes/alkenes or aromatics at 2975 cm^{-1}. Other CH vibrations in this area are most likely attributable to alkane functionalities (e.g., at 2898 cm^{-1}) and can be found in both samples, but more so in Cu-L.

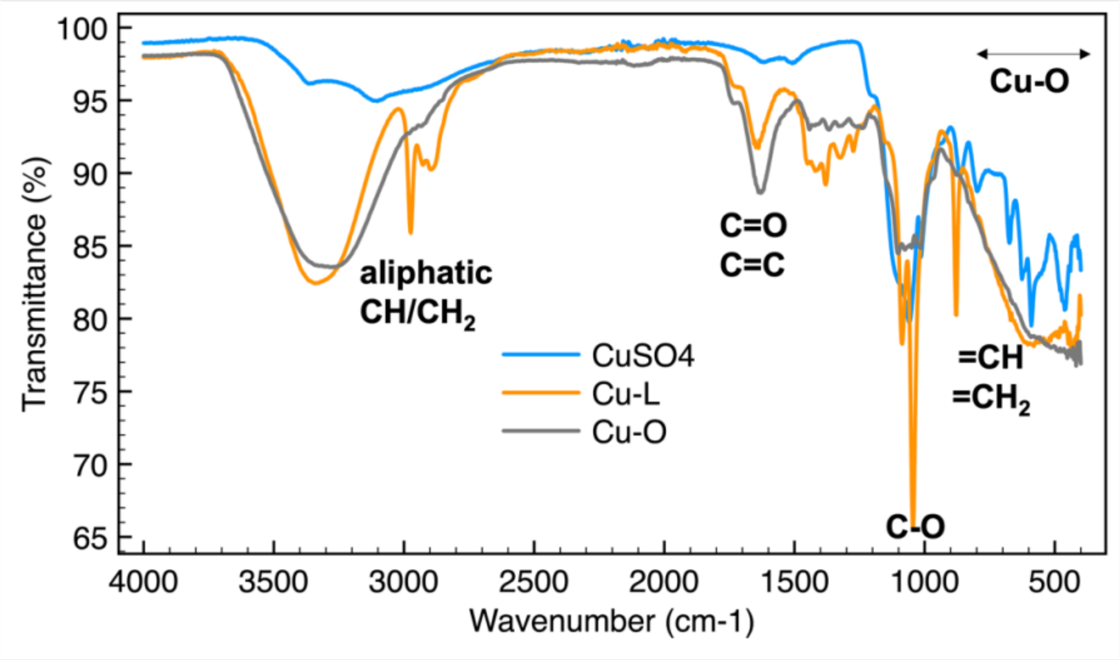

Figure 2.9: IR spectra of indicated samples (blue line $CuSO_4$, orange Cu-L, and grey Cu-O).

Cu-L is additionally distinguished by intense peaks at 1046 cm^{-1} and 1086 cm^{-1}, which correspond to C-O bond vibrations of ethers, carboxylic acids (and derivatives such as anhydrides), and alcohol/methoxy species. This area also contains S-O species, which are projected to be in greater abundance for Cu-L. Cu-L contains multiple peaks between 1214 cm^{-1} and 1492 cm^{-1} that are more intense than Cu-O sample and can be attributed to a variety of bending and stretching vibrations of the functional group previously stated above. The peak at 1635 cm^{-1}, on the other hand, is more intense for the sample Cu-O, which is related to C=C vibrations in alkenes and aromatic hydrocarbons but also C=O vibrations in unsaturated ketones and amides. A modest peak at 1720 cm^{-1} verifies the presence of C=O species in carboxylic acids and derivatives, as well as ketones that have not been conjugated with other unsaturated functionalities. Another variation between the samples may be noticed above 3000 cm^{-1}. Cu-L has a wide band width at around 3340 cm^{-1} due to H-bonded OH of alcohols, phenols, or carboxylic acids. Furthermore, the Cu-O sample exhibits an overlapping broad band with a maximum at around 3240 cm^{-1}, which is typically attributed to the same kind of species, but in a different chemical environment from the preceding one. Thus, Cu-O has a C-backbone with a more extended conjugated π-system, while the Cu-L sample has more CH terminals, including aromatic species, and more C-O single bonds, which is consistent with the XPS study in Figure 2.8 c.

Finally, X-ray diffraction (XRD) measurements were performed by Bruker D8-Advance by using Cu-Kα (λ= 1,54186 Å) as the source, in the range of 2θ from 10° to 85°. Figure 2.10 shows the XRD pattern of as-prepared samples.

The diffractograms confirm that the synthesized samples, after thermal treatment, show Cu and Cu_2O crystal diffraction peaks, and even a broad peak attributed to carbonaceous support. No other peaks were detected, which demonstrates that the samples have high phase purity.

The orientation planes of the metallic Cu (111), (200), and (220) were represented by the diffraction peaks obtained at 2θ = 43.3, 50.34, and 74.08° [55] and Cu_2O (111) and (220) at 36.43, and 61,71° [56].

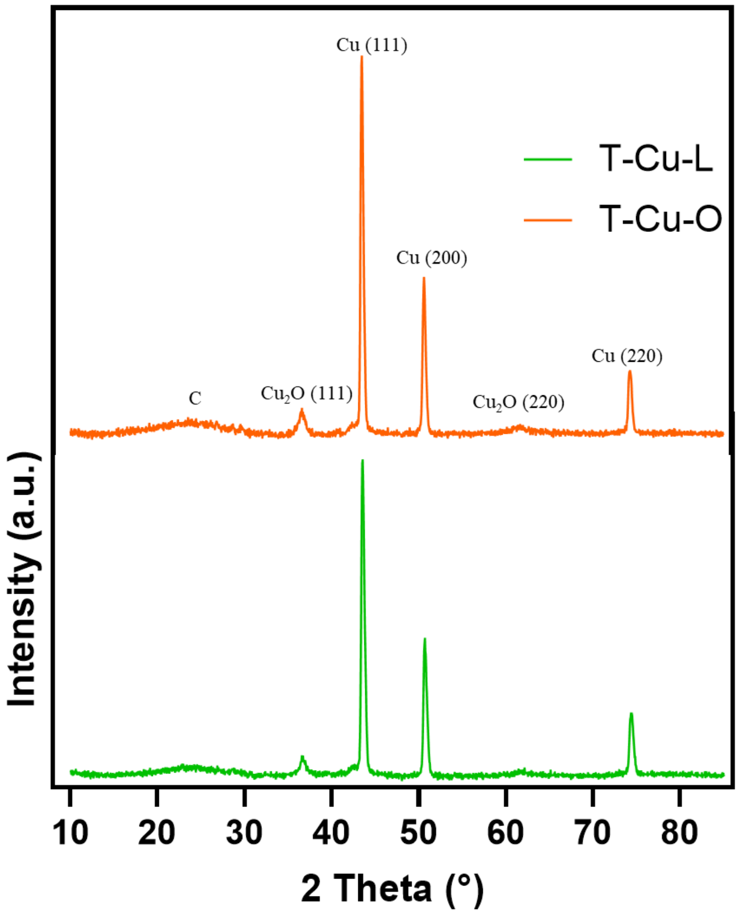

Figure 2.10: X-ray diffraction patterns of the as-prepared electrodes T-Cu-L (in green) and T-Cu-O (in orange).

2.8 Protocol testing

The experiments were performed by using T-Cu-L and T-Cu-O as working electrode (WE), its geometric surface is about 6 cm^2.

The setup of the electrochemical cell, where the experiments take place, is shown in figure 2.3. A 0.1 M KOH (or $KHCO_3$) and CO_2-saturated solution is used to perform the reaction in the cathodic compartment, while the electrolyte solution (0.1M KOH or $KHCO_3$) is used for the anodic compartment. The two sides are separated by a cation exchange membrane (Nafion 115). The cathode tank is flowed with CO_2 (20 ml/min) for 20 minutes to obtain a CO_2 saturated electrolytic solution. The electrolytic solutions are flushed to both the compartments by using a peristaltic pump. The solution volume (cathode + external tank + tubes) is 35 ml and the net volume in the cathodic compartment is 7 ml, the same as in the anode.

Cyclic voltammetry in the potential range 1.5÷-2 V vs Ag/AgCl and scan rate of 50 mV/sec was carried out in 0.1M KOH solution suturated with CO_2.

The amperometric detection experiments were performed at constant applied voltage in the range of -1.8 and -2 V vs Ag/AgCl, monitoring the current density. In the anodic compartment, the H^+ are generated in situ by water co-electrolysis. They move through the Nafion membrane to reach the cathodic side where the reduction reaction occurs. The test was carried out for 2 hours per each potential investigated. The liquid products were analyzed using an ion chromatograph. The analyses were performed on a Metrohm ion chromatograph with a mobile phase of H_2SO_4 0.05 mm, a flow rate of 0.05 ml/min, and an average pressure of 5 MPa, and a stationary phase of a column for organic acids 25 cm long and with an internal diameter of 7.8 mm, preceded by a Metrosep Organic Acid Guard pre-column 50 mm long and 4 mm thick. At 215 nm, a 944 professional UV/vis Detector Vario detector was utilized to detect the products. Gaseous products developed in the headspace were analyzed, exploiting the online connection to the micro gas chromatograph (Micro GC, Agilent 490),. The instrument has two columns: (i) PoraPLOT Q for the determination of volatile organic compounds and (ii) Molsieve 5 A for the separation of inorganic compounds (H_2, N_2 and O_2, CO and CH_4). Analytes are determined using a thermal conductivity detector (TCD).

2.9 Cyclic Voltammetry (CV)

The electrodes were investigated by CV[57–59] to define their redox behavior.

Figure 2.11 shows the CV in 0.1M KOH CO_2-saturated solution of T-Cu-L and T-Cu-O samples.

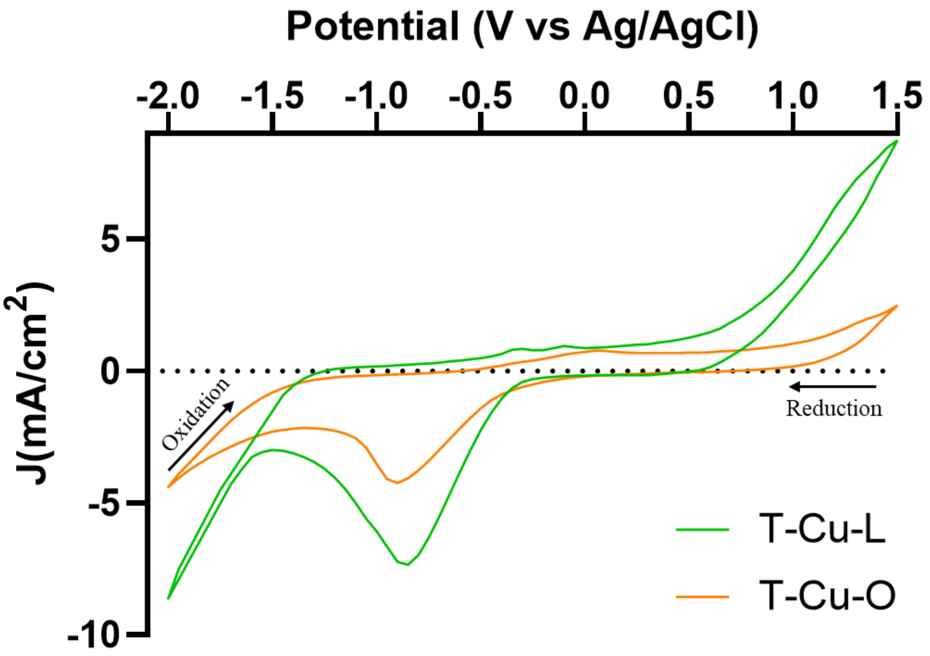

Figure 2.11: Cyclic voltammetry of T-Cu-L (green curve) and T-Cu-O (orange curve) electrodes in 0.1M KOH CO_2-saturated solution.

According to eq. 2.3, a reversible reduction peak at around -0.86 V vs Ag/AgCl was identified and was attributable to the pair redox Cu^{1+}/Cu^{0}.

$$Cu^{1+} + H^{+} + e^{-} \rightarrow Cu^{0} \qquad \text{(eq. 2.3)}$$

According to eq. 2.4, the production of gaseous hydrogen begins around -1.60 V vs Ag/AgCl. The recorded negative current in this area is because of this reaction.

$$2H_2 + 2e^{-} \rightarrow H_2 \qquad \text{(eq. 2.4)}$$

Besides, two anodic peaks in the range -0.4 and 0.05 V vs Ag/AgCl are also noticed. A peak approximately at -0.4 V is probably attributed to electrochemical OH adsorption of electrolyte solution[60], while the peak at 0.05 V is due to the equation reported in eq. 2.5:

$$Cu^{0} \rightarrow Cu^{1+} + H^{+} + e^{-} \qquad \text{(eq. 2.5)}$$

2.10 Electrochemical Surface Area

The electrochemical surface area (ESCA) is an important parameter typically used to characterize the surface of electrocatalysts. By using CV methods ECSA is estimated according the method of Qiao et al.[61].

Firstly, the double layer capacitance (C_{DL}) has to be determined. C_{DL} depends on the features of the interface electrolyte/electrode. Overall, C_{DL} was determined using the charge amount stocked on the electrode surface area. Usually, it is used to calculate the surface area by electrochemical measurement. Also, it is a quantitative measure of the surface area that the electrolyte ions may reach. In order to obtain C_{DL} via CV, several tests at different scan rates in a non-faradaic range were recorded[62]. T-Cu-O and T-Cu-L samples (having a geometric area=1.5 cm^2) were used as working electrodes to record CVs in a N_2-saturated solution of 0.1M $NaClO_4$.

As shown in figure 2.12 a,b, the studied non-faradic range is from 0.05 to -0.35 V vs Ag/AgCl at 10, 20, 50, 80, and 120 mV/s. The current in this potential range is considered to be generated due to double-layer charging. In order to calculate C_{DL} via CV measurement, the average current values from anodic and cathodic charging current at -0.35 V vs Ag/AgCl were acquired. Afterward, the average of these current values was plotted against the scan rate (figure 2.12 c,d).
According to eq. 2.6 it is possible to define the C_{DL}.

$$I = C_{DL} * v \qquad \text{(eq. 2.6)}$$

The results highlight a linear relationship between the two parameters, and as can be shown in equation 2.7, the C_{DL} value may be calculated by taking the absolute value of the slope of the regressed straight lines[63]. Once having determined the value of the C_{DL}, ECSA was calculated according to eq. 2.7[61]

$$\mathrm{ECSA} = \frac{C_{DL}}{C_s} \qquad \text{(eq. 2.7)}$$

C_s is the specific capacitance and in this used conditions is equal to 30 µF [64].

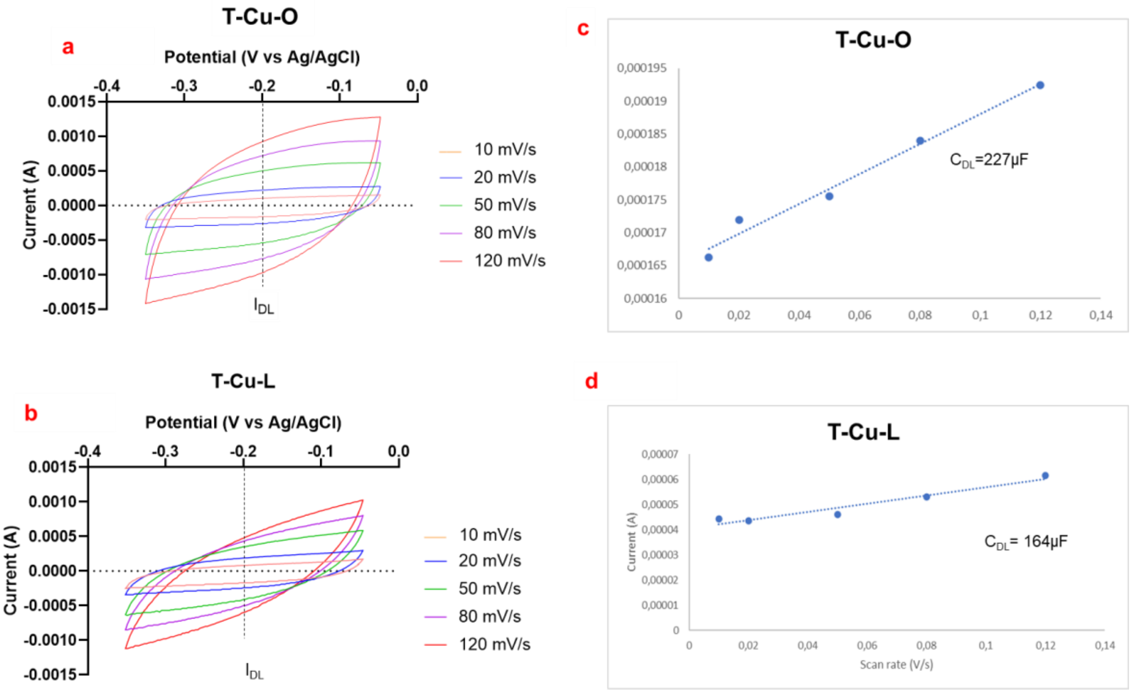

Figure 2.12: Cyclic voltammetry recorded in a range from 0.05 to -0.35 V vs Ag/AgCl of a) T-Cu-O and b) T-Cu-L at different scan rates (10, 20, 50, 80, and 120 mV/s). Average current values from anodic and cathodic charging current at -0.2 V vs Ag/AgCl against different scan rates (10, 20, 50, 80, and 120 mV/s). The slope of the regressed straight lines determines the value of the C_{DL}, c) T-Cu-O and d) T-Cu-L.

The as-calculated values of ECSA for each electrode are reported in table 2.4.

Table 2.4: Double layer capacitance and electrochemical surface area values for each working electrode.

Sample	**C_{DL} (µF)**	**ECSA (cm^2)**
T-Cu-O	227	7.6
T-Cu-L	164	5.5

T-Cu-O shows a higher surface area than T-Cu-L. It is il line with the previous findings, confirming that the orange peel leads to a more active catalyst for CO_2RR.

2.11 Results and discussion

The thermally treated samples were employed as electrocatalysts and investigated in an electrochemical CO_2 reduction in a 0.1M KOH, or $KHCO_3$ solution CO_2-saturated utilizing a three-electrode electrochemical cell (figure 2.3).

Figure 2.13 and Table 2.5 summarize the findings for the 2-hour testing at the applied potential of -1.8 V and -2 V versus Ag/AgCl.

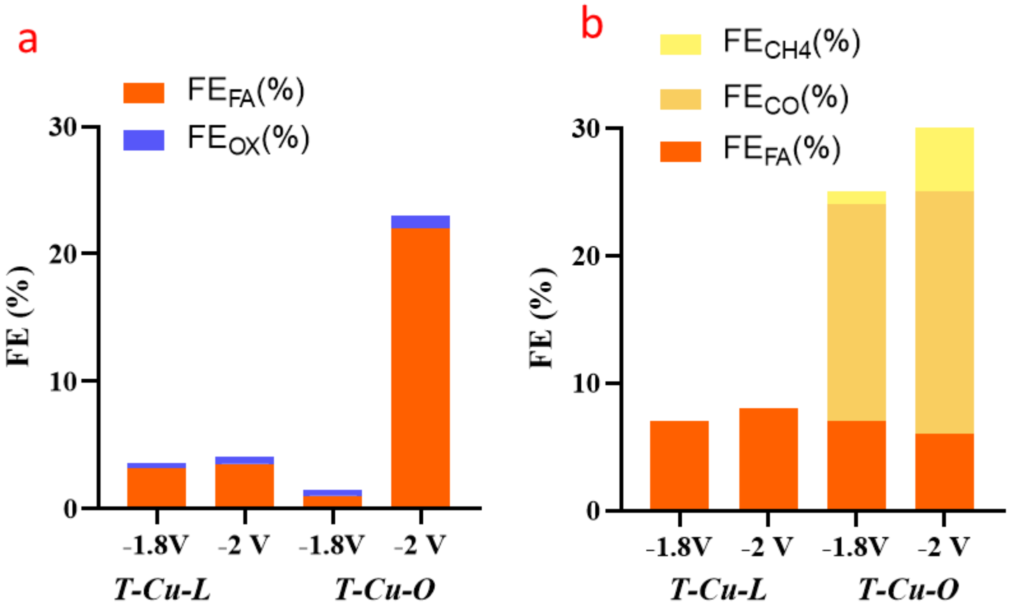

Figure 2.13: Faradaic efficiency (FE) to formate and oxalate a) in 0.1M KOH and b) in 0.1M $KHCO_3$ solution of the T-Cu-O and T-Cu-L electrodes, after 2 hours of testing.

At both potentials and for both electrocatalysts studied, the CO_2 reduction products in liquid phase are mainly formic acid (FA) and oxalic acid (OA). Unfortunately, due to the parasitic HER, the main gaseous product is H_2. Furthermore, traces of methane and ethylene were found at both potentials.

Table 2.5: Faradaic efficiency of formate (FA), oxalate (OX), carbon monoxide (CO), and methane (CH_4) of each tested working electrode at each potential (-1.8 and -2 V vs Ag/AgCl) and the current density.

KOH						
Sample	Potential (V)	FE_{FA}(%)	FE_{OX}(%)	FE_{CO}(%)	FE_{CH4}(%)	J (mA/cm^2)
T-Cu-L	-1.8	3	0,4	-	-	- 4.2
T-Cu-L	-2	4	0,6	-	-	-5.0
T-Cu-O	-1.8	1	0,5	-	-	- 4.0
T-Cu-O	-2	22	1	-	-	- 5.8
$KHCO_3$						
T-Cu-L	-1.8	7	-	-	-	- 3.0
T-Cu-L	-2	8	-	-	-	- 3.8
T-Cu-O	-1.8	7	-	17	1	- 2.9
T-Cu-O	-2	6	-	19	8	- 4.0

The performances of the T-Cu-L electrocatalyst do not vary appreciably at the two potentials examined, with a faradaic efficiency (FE) to FA slightly less than 5%. When the voltage is reduced to -2 V vs. Ag/AgCl, the T-Cu-O electrode performs substantially better, with FE_{FA} reaching 22%. According to a study on the effect of electrolytes, KOH was found to produce a low quantity of formate due to its high pH, which makes this reaction unfavorable[65]. Instead here, the combination of high pH effect, partial graphitization (Figure 2,8 b), or Cu surface decorating with a C overlayer (Figure 2.4 c, d) may result in a somewhat greater overpotential for FA generation[66].

Also, even better stability of T-Cu-O is found in a 3 h reaction, which leads to the synthesis of formic acid with a FE approaching 35%, while T-Cu-L is unstable after 3 h and its performance deteriorates dramatically. Generally, electrode degradation might occur in a long-term CO_2RR reaction[67]. This could be because of salt formation (carbonates) near the catalyst surface as the product of the reaction between CO_2 and KOH[68]. Therefore, the electrolyte solution and electrode would need to be changed after a few hours[69]. As a consequence, KOH results in a less favorable electrolyte in a long-term reaction because carbonates lead to an intricate mass transport problem that affects the diffusion of the reactive species close to the catalyst surface[70].

To study the behavior of catalysts in another electrolyte, the most used salt ($KHCO_3$) was employed. At both potentials (-1.8 and -2 V vs Ag/AgCl) for T-Cu-O, the CO_2 reduction products are formate, carbon monoxide, and methane, while for T-Cu-L the only product is formate. Even this time, the main product was H_2 generated from the HER side reaction. As reported in figure 2.13 and table 2.5, the best results were achieved by T-Cu-O at –2 V vs Ag/AgCl reaching a FE_{CH4} and FE_{CO} equal to 8% and 19%, respectively, while the FE_{FA} achieved by T-Cu-L at both potentials is steady at around 8%. The influence of electrolyte would seem to highlight that KOH has a better performance than $KHCO_3$ to produce C_2 (OX and a small amount of ethylene). As reported in the literature, KOH is useful in C_2 production thanks to the high pH that favors the coupling and also is more conductive (clearly shown by the current density in table 2.5) than $KHCO_3$[70]. Instead, the reaction in $KHCO_3$ leads only toward the production of C1 (methane, carbon monoxide, and formic acid). Anyway, in both electrolytes the best performance was reached by the T-Cu-O electrode.

Excessive Cu exposure, shown in this study, seems to be deleterious to CO_2 reduction while favoring the HER, suggesting that the carbon overlayer plays a crucial role in regulating selectivity. Indeed, in heterogeneous catalysis, the importance of the C overlayer in influencing the selectivity of metal NPs is well established[71]. Nonetheless, findings support the positive action of the orange peel ingredients, such as was shown during the electrocatalyst production, with effects on the CO_2RR performance.

During Cu-O synthesis, an improved particle size control was achieved, as well as superior stability on the resultant C support having a more favorable structure for electrocatalysis. For increased CO_2RR product productivity, good Cu dispersion is necessary; the carbon support has to be quite functionalized to stabilize the particles, and even be enough graphitic to allow electron conduction. Furthermore, heteroatoms on the C matrix with basic character, such as N, S, and O species, are often advantageous, especially when wet impregnation was used to immobilize the metal[72]. The distinct chemical speciation between the orange and lemon peel-derived systems is an intriguing result showing a chance for application-oriented tunability of the synthesis and the utilization of biomasses waste. The chemical speciation of the peels differed somewhat between the initial peels and after CuNPs immobilization, with the orange peel being more hydrophilic and exhibiting more and stronger reducing functions. The latter results in a marked difference in the nature of the species of the carbonaceous species, with Cu-L undergoing deoxygenation/dehydrogenation of the cellulose/lignin structural units, instead it progresses further on Cu-O up to aromatic ring condensation and extended π-conjugation.

Following Cu immobilization, thermal annealing of the sample can favor ring condensation and deoxygenation of the C support at a lower temperature for orange peel-derived samples than for lemon peel. However, post-synthesis heat treatments often have poor particle size control, whereas the application of capping agents in wet chemistry to avoid particle overgrowth produces generally superior outcomes[54,71].

Given the more hydrophilic nature of the orange peel than the lemon peel, and the optimum control of Cu particle size obtained in this system, one could hypothesize that the orange peel releases some of the water-soluble, low molecular weight compounds with reducing properties for Cu-solvated cations, as ascorbic acid. The idea was that the peel components may be used directly in the reduction of aqueous

Cu species in a one-pot synthesis without the need for any further additions. To explain this finding, a preliminary liquid chromatography–mass spectrometry (LC-MS) analysis of the aqueous supernatant after hydrothermal treatment of the peels with or without Cu sulfate reveals not only minor differences in the amount of ascorbic acid present, which we initially proposed as the primary reducing agent, but also a different composition of other naturally present antioxidant components (catechins) between the orange and lemon peel. Especially, a component correlated to epicatechin[73] is found only in the aqueous supernatant of the orange peel and is consumed in the hydrothermal synthesis of the Cu NPs indicating a potential advantage for these compounds in particle size control as well as the deoxygenation of the C matrix by these compounds. This means that the antioxidants are released into the solution first to reduce the Cu(II) aquo-sulphate-complex to produce nanoparticles, and afterwards adsorb them on the surface to inhibit further development[74]. Following thermal annealing, the deposited nanoparticles on the insoluble portion of the peel are preserved. On the other hand, the Cu(II) aquo-sulfate-species not reduced by the naturally present antioxidants, are adsorbed as atomically distributed species on the cellulose component of the peel and function as a nucleation center to form bigger sulfate particles after hydrothermal treatment and centrifugation.

2.12 Conclusion

To summarize, in this chapter, a synthesis of Cu electrocatalyst from biomass-derived precursors active in CO_2 electroreduction is successfully achieved. This work demonstrates the significance of the nanostructural properties of the electrode in boosting the performances of electrocatalysts with tunability, even when starting with biomass-derived carbonaceous precursors with intrinsically complicated chemical compositions. The multifactorial role of carbon support in electrocatalysis was identified (templating role in nanoparticle formation, electrical conductor, stabilization, and controlled metal exposure during electrocatalysis), as well as the unique opportunity provided by functionally complex chemical waste such as orange peel to realize this. The value of this contribution depends on the fact that it demonstrates the viability of using citrus waste directly to produce useful materials in a green manner without the addition of any templating or reducing agent; it offers a rational approach for tailored synthesis and thus a framework for effectively exploring this carbon source.

Taking everything into account, although the initial focus is on the CO_2 reduction reaction, the findings can be broadly applied to the preparation of orange peel derived C-supported metal electrocatalysts for other electrocatalytic reactions relevant in storage and energy conversion, as well as any applications requiring a homogeneous Cu distribution.

Bibliography

1. Xie, H., Wang, T., Liang, J., Li, Q. & Sun, S. Nano Today Cu-based nanocatalysts for electrochemical reduction of CO 2. *Nano Today* **21**, 41–54 (2018).
2. Ganji, P. *et al.* Toward Commercial Carbon Dioxide Electrolysis. **2000096**, 1–22 (2020).
3. Fan, L. *et al.* Strategies in catalysts and electrolyzer design for electrochemical CO 2 reduction toward C 2 + products. 1–17 (2020).
4. Zhu, D. D., Liu, J. L. & Qiao, S. Z. Recent Advances in Inorganic Heterogeneous Electrocatalysts for Reduction of Carbon Dioxide. 3423–3452 (2016) doi:10.1002/adma.201504766.
5. Birdja, Y. Y. *et al.* to fuels. *Nat. Energy* **4**, (2019).
6. Ruiz-López, E., Gandara-Loe, J., Baena-Moreno, F., Reina, T. R. & Odriozola, J. A. Electrocatalytic CO2 conversion to C2 products: Catalysts design, market perspectives and techno-economic aspects. *Renew. Sustain. Energy Rev.* **161**, (2022).
7. Zhang, L., Zhao, Z. & Gong, J. Nanostructured Materials for Heterogeneous Electrocatalytic CO 2 Reduction and their Related Reaction Mechanisms Angewandte. 11326–11353 (2017) doi:10.1002/anie.201612214.
8. Bharath, G. *et al.* Fabrication of Pd / MnFe 2 O 4 bifunctional 2-D nanosheets to enhance the yield of HCOOH from CO 2 cathodic reduction paired with anodic oxidation to CH 3 OH. *Fuel* **311**, 122619 (2022).
9. Back, S., Yeom, M. S. & Jung, Y. Active Sites of Au and Ag Nanoparticle Catalysts for CO2 Electroreduction to CO. *ACS Catal.* **5**, 5089–5096 (2015).

10. Wang, T. J. *et al.* Heterostructured Pd/PdO nanowires for selective and efficient CO2 electroreduction to CO. *J. Energy Chem.* **70**, 407–413 (2022).

11. Back, S., Kim, H. & Jung, Y. Selective heterogeneous CO2 electroreduction to methanol. *ACS Catal.* **5**, 965–971 (2015).

12. Yang, H. *et al.* Scalable Production of Efficient Single-Atom Copper Decorated Carbon Membranes for CO2 Electroreduction to Methanol. *J. Am. Chem. Soc.* **141**, 12717–12723 (2019).

13. Spurgeon, J. M. Environmental Science A comparative technoeconomic analysis of pathways for commercial electrochemical CO 2 reduction to liquid products †. 1536–1551 (2018) doi:10.1039/c8ee00097b.

14. Lin, R., Guo, J., Li, X., Patel, P. & Seifitokaldani, A. *Electrochemical Reactors for CO 2 Conversion*. (2020).

15. Wang, X., Zhao, Q., Yang, B., Li, Z. & Bo, Z. precious metal electrocatalysts for selective electrochemical CO 2 reduction to CO. 25191–25202 (2019) doi:10.1039/c9ta09681g.

16. Qiao, J., Liu, Y., Hong, F. & Zhang, J. *A review of catalysts for the electroreduction of carbon dioxide to produce low-carbon fuels*. *Chemical Society Reviews* vol. 43 (2014).

17. Kuhl, K. P. *et al.* Electrocatalytic Conversion of Carbon Dioxide to Methane and Methanol on Transition Metal Surfaces. (2014).

18. Whipple, D. T. & Kenis, P. J. A. Prospects of CO 2 Utilization via Direct Heterogeneous Electrochemical Reduction. 3451–3458 (2010) doi:10.1021/jz1012627.

19. Jhong, H. M., Ma, S. & Kenis, P. J. A. Electrochemical conversion of CO 2 to useful chemicals : current status , remaining challenges , and future

opportunities. *Curr. Opin. Chem. Eng.* **2**, 191–199.

20. Description, C. *Main Cell Components, Material Properties, and Processes*. *PEM Fuel Cells: Theory and Practice* (2012). doi:10.1016/B978-0-12-387710-9.00004-7.

21. Kim, S. *et al.* Fabrication and Performance Evaluation of a Cation Exchange Membrane Using Graphene Oxide/Polyethersulfone Composite Nanofibers. *Membranes (Basel).* **13**, 1–14 (2023).

22. Solonchenko, K., Kirichenko, A. & Kirichenko, K. Stability of Ion Exchange Membranes in Electrodialysis. *Membranes (Basel).* **13**, 1–18 (2023).

23. Siyu Ye, Miho Hall, and P. H. & Ballard. PEM Fuel Cell Catalysts: The Importance of Catalyst Support. **01**, 1–23 (2016).

24. Antolini, E. Carbon supports for low-temperature fuel cell catalysts. *Appl. Catal. B Environ.* **88**, 1–24 (2009).

25. Vassilev, S. V., Baxter, D., Andersen, L. K. & Vassileva, C. G. An overview of the chemical composition of biomass. *Fuel* **89**, 913–933 (2010).

26. Pantea, D., Darmstadt, H., Kaliaguine, S. & Roy, C. Electrical conductivity of conductive carbon blacks: Influence of surface chemistry and topology. *Appl. Surf. Sci.* **217**, 181–193 (2003).

27. Rafiee, R. & Moghadam, R. M. On the modeling of carbon nanotubes: A critical review. *Compos. Part B Eng.* **56**, 435–449 (2014).

28. Budai, A. *et al.* Biochar Carbon Stability Test Method : An assessment of methods to determine biochar carbon stability. *Int. Biochar Initiat.* 1–10 (2013).

29. Rosli, R. E. *et al.* A review of high-temperature proton exchange

membrane fuel cell (HT-PEMFC) system. *Int. J. Hydrogen Energy* **42**, 9293–9314 (2017).

30. Bhuvanendran, N. *et al.* Emerging Trends in Biomass-Derived Carbon-Supported Metal Nanostructures as Efficient Electrocatalysts for Critical Electrochemical Reactions in Low Temperature Fuel Cell Applications. *ACS Symp. Ser.* **1410**, 225–256 (2022).

31. Gawande, M. B. *et al.* Cu and Cu-Based Nanoparticles: Synthesis and Applications in Catalysis. *Chem. Rev.* **116**, 3722–3811 (2016).

32. Raciti, D. & Wang, C. Recent Advances in CO2 Reduction Electrocatalysis on Copper. *ACS Energy Lett.* **3**, 1545–1556 (2018).

33. Lee, S. Y. *et al.* Mixed Copper States in Anodized Cu Electrocatalyst for Stable and Selective Ethylene Production from CO 2 Reduction. *J. Am. Chem. Soc.* **140**, 8681–8689 (2018).

34. Moayedi, H., Aghel, B., Abdullahi, M. M., Nguyen, H. & Safuan A Rashid, A. Applications of rice husk ash as green and sustainable biomass. *J. Clean. Prod.* **237**, (2019).

35. Varma, R. S. Biomass-Derived Renewable Carbonaceous Materials for Sustainable Chemical and Environmental Applications. *ACS Sustain. Chem. Eng.* **7**, 6458–6470 (2019).

36. Kumar, A., Bhattacharya, T., Mozammil Hasnain, S. M., Kumar Nayak, A. & Hasnain, M. S. Applications of biomass-derived materials for energy production, conversion, and storage. *Mater. Sci. Energy Technol.* **3**, 905–920 (2020).

37. Zhang, M., Zhang, J., Ran, S., Sun, W. & Zhu, Z. Biomass-Derived sustainable carbon materials in energy conversion and storage applications: Status and opportunities. A mini review. *Electrochem. commun.* **138**,

107283 (2022).

38. Reza, M. S. *et al.* Advanced Applications of Carbonaceous Materials in Sustainable Water Treatment, Energy Storage, and CO2 Capture: A Comprehensive Review. *Sustain.* **15**, (2023).

39. Titirici, M. M. *et al.* Sustainable carbon materials. *Chem. Soc. Rev.* **44**, 250–290 (2015).

40. Raimondo, M. *et al.* Making virtue out of necessity: Managing the citrus waste supply chain for bioeconomy applications. *Sustain.* **10**, 1–20 (2018).

41. Sharma, K., Mahato, N., Cho, M. H. & Lee, Y. R. Converting citrus wastes into value-added products: Economic and environmently friendly approaches. *Nutrition* **34**, 29–46 (2017).

42. Loiudice, A. *et al.* Tailoring Copper Nanocrystals towards C 2 Products in Electrochemical CO 2 Reduction . *Angew. Chemie* **128**, 5883–5886 (2016).

43. Marepally, B. C. *et al.* Electrocatalytic reduction of CO2 over dendritic-type Cu- A nd Fe-based electrodes prepared by electrodeposition. *J. CO2 Util.* **35**, 194–204 (2020).

44. Gai, L., Li, J., Wang, Q., Tian, R. & Li, K. Evolution of biomass to porous graphite carbon by catalytic graphitization. *J. Environ. Chem. Eng.* **9**, 106678 (2021).

45. Jiang, P. *et al.* Experimental and theoretical investigation of the electronic structure of Cu2O and CuO thin films on Cu(110) using x-ray photoelectron and absorption spectroscopy. *J. Chem. Phys.* **138**, (2013).

46. Arrigo, R. *et al.* Dynamics over a Cu-graphite electrode during the gas-phase CO2 reduction investigated by APXPS. *Faraday Discuss.* **236**, 126–140 (2022).

47. Liu, B. H., Huber, M., van Spronsen, M. A., Salmeron, M. & Bluhm, H.

Ambient pressure X-ray photoelectron spectroscopy study of room-temperature oxygen adsorption on Cu(1 0 0) and Cu(1 1 1). *Appl. Surf. Sci.* **583**, 152438 (2022).

48. Ghodselahi, T., Vesaghi, M. A., Shafiekhani, A., Baghizadeh, A. & Lameii, M. XPS study of the Cu@Cu 2 O core-shell nanoparticles. *Appl. Surf. Sci.* **255**, 2730–2734 (2008).

49. Biesinger, M. C. Advanced analysis of copper X-ray photoelectron spectra. *Surf. Interface Anal.* **49**, 1325–1334 (2017).

50. Arrigo, R. *et al.* Dynamics at Polarized Carbon Dioxide–Iron Oxyhydroxide Interfaces Unveil the Origin of Multicarbon Product Formation. *ACS Catal.* **12**, 411–430 (2022).

51. Kuzmenko, V. *et al.* Cellulose-derived carbon nanofibers/graphene composite electrodes for powerful compact supercapacitors. *RSC Adv.* **7**, 45968–45977 (2017).

52. Wahlqvist, M. & Shchukarev, A. XPS spectra and electronic structure of Group IA sulfates. *J. Electron Spectros. Relat. Phenomena* **156–158**, 310–314 (2007).

53. Sir Elkhatim, K. A., Elagib, R. A. A. & Hassan, A. B. Content of phenolic compounds and vitamin C and antioxidant activity in wasted parts of Sudanese citrus fruits. *Food Sci. Nutr.* **6**, 1214–1219 (2018).

54. Arrigo, R. *et al.* Influence of Synthesis Conditions on the Structure of Nickel Nanoparticles and their Reactivity in Selective Asymmetric Hydrogenation. *ChemCatChem* **12**, 1491–1503 (2020).

55. Kumar, B. *et al.* Nanohybrid Cu@C: synthesis, characterization and application in enhancement of lubricity. *Compos. Interfaces* **27**, 777–794 (2020).

56. Suryawanshi, S. R. *et al.* 3D Hetero-architecture of GdB6 nanoparticles on lessened cubic Cu2O nanowires: Enhanced field emission behaviour. *CrystEngComm* **17**, 3936–3944 (2015).

57. Sugiawati, V. A., Vacandio, F., Galeyeva, A., Kurbatov, A. P. & Djenizian, T. Enhanced Electrochemical Performance of Electropolymerized Self-Organized TiO2 Nanotubes Fabricated by Anodization of Ti Grid. *Front. Phys.* **7**, 1–8 (2019).

58. Fabregat-Santiago, F., Mora-Seró, I., Garcia-Belmonte, G. & Bisquert, J. Cyclic voltammetry studies of nanoporous semiconductors. Capacitive and reactive properties of nanocrystalline TiO2 electrodes in aqueous electrolyte. *J. Phys. Chem. B* **107**, 758–768 (2003).

59. Makivić, N. *et al.* Evidence of Bulk Proton Insertion in Nanostructured Anatase and Amorphous TiO2Electrodes. *Chem. Mater.* **33**, 3436–3448 (2021).

60. Caballero-Briones, F., Artés, J. M., Díez-Pérez, I., Gorostiza, P. & Sanz, F. Direct observation of the valence band edge by in situ ECSTM-ECTS in p-type Cu2O layers prepared by copper anodization. *J. Phys. Chem. C* **113**, 1028–1036 (2009).

61. Qiao, J., Jiang, P., Liu, J. & Zhang, J. Formation of Cu nanostructured electrode surfaces by an annealing-electroreduction procedure to achieve high-efficiency CO2 electroreduction. *Electrochem. commun.* **38**, 8–11 (2014).

62. Connor, P., Schuch, J., Kaiser, B. & Jaegermann, W. The Determination of Electrochemical Active Surface Area and Specific Capacity Revisited for the System MnOx as an Oxygen Evolution Catalyst. *Zeitschrift fur Phys. Chemie* **234**, 979–994 (2020).

63. Li, X. *et al.* Titanium dioxide nanotubes as model systems for

electrosorption studies. *Nanomaterials* **8**, (2018).

64. de Sousa, L., Harmoko, C., Benes, N. & Mul, G. Optimizing the Ink Formulation for Preparation of Cu-Based Gas Diffusion Electrodes Yielding Ethylene in Electroreduction of CO 2 . *ACS ES&T Eng.* **1**, 1649–1658 (2021).

65. Kim, H. Y. *et al.* Analysis on the effect of operating conditions on electrochemical conversion of carbon dioxide to formic acid. *Int. J. Hydrogen Energy* **39**, 16506–16512 (2014).

66. Ren, D. *et al.* Selective Electrochemical Reduction of Carbon Dioxide to Ethylene and Ethanol on Copper(I) oxide catalysts. *ACS Catal.* **5**, 2814–2821 (2015).

67. Popović, S. *et al.* Stability and Degradation Mechanisms of Copper-Based Catalysts for Electrochemical CO2 Reduction. *Angew. Chemie - Int. Ed.* **59**, 14736–14746 (2020).

68. Leonard, M. E., Clarke, L. E., Forner-Cuenca, A., Brown, S. M. & Brushett, F. R. Investigating Electrode Flooding in a Flowing Electrolyte, Gas-Fed Carbon Dioxide Electrolyzer. *ChemSusChem* **13**, 400–411 (2020).

69. Dinh, C. T., García De Arquer, F. P., Sinton, D. & Sargent, E. H. High rate, selective, and stable electroreduction of co2 to co in basic and neutral media. *ACS Energy Lett.* **3**, 2835–2840 (2018).

70. Jing-Jing Lv, Matthew Jouny, Wesley Luc, Wenlei Zhu, Jun-Jie Zhu, and F. J. Highly Porous Copper Electrocatalyst for Carbon Dioxide Reduction Jing-Jing. *J. JSEE* **64**, 1_66-1_66 (2016).

71. Arrigo, R. *et al.* Pd Supported on Carbon Nitride Boosts the Direct Hydrogen Peroxide Synthesis. *ACS Catal.* **6**, 6959–6966 (2016).

72. Arrigo, R. & Schuster, M. E. On the high structural heterogeneity of fe-

impregnated graphitic-carbon catalysts from fe nitrate precursor. *Catalysts* **9**, (2019).

73. Escobar-Avello, D. *et al.* Phenolic profile of grape canes: Novel compounds identified by LC-ESI-LTQ-orbitrap-MS. *Molecules* **24**, 1–21 (2019).

74. Miah,T. et al. Orange-Peel Biomass-derived Carbon Supported Cu Electro-catalysts Active in the CO2-Reduction to Formic Acid ChemPhysChem **202200589**, (2023). Doi: doi.org/10.1002/cphc.202200589

CHAPTER 3

3.1 Electrochemical conversion of CO_2 to C_2 product

As became clear from the previous chapter, breaking the carbon-oxygen bonds of a CO_2 molecule requires a lot of energy. One of the main issues in energy chemistry is the manufacture of high-value compounds by electrocatalytic reduction of CO_2 in order to promote a chemical industry free of fossil fuels and based on renewable energy sources[1,2].

However, only a small number of C_2 products (mainly C_2H_4, C_2H_5OH, and CH_3COOH) may be produced by directly electro-catalytically reducing CO_2. Therefore, the expansion of the value chain in the use of CO_2 can be achieved by addressing new possibilities related to the formation of C_2.

For example, C_1 products of CO_2 reduction, such as CO[3], CH_3OH[4], and HCOOH[5] are easily produced with high efficiency, and they allow the production of C_2 and C_3 (multicarbon) fuels, and chemicals.

In recent years, many initiatives have been sponsored inside the European Union with the goal of both creating new CCU technologies and maturing and improving those that are already available, bringing them closer to the commercial scale. Among these was the OCEAN project (ID 767798), which was part of the Horizon 2020 program and featured both academic and industry partners. It is schematically depicted in figure 3.1.

This chapter is based on:

De Luca, F., Passalacqua, R., Abramo, F. P., Centi, G., Abate, S.
$g\text{-}C_3N_4$ Decorated TiO_2 Nanotube Ordered Thin Films as Cathodic Electrodes for the Selective Reduction of Oxalic Acid, Chemical Engineering Transactions **84**, 37–42 (2021). 10.3303/CET2184007

Passalacqua, R., Abate, S., De Luca, F., Perathoner, S., Centi, G.
Graphitic Layered Structures Enhancing TiNT Catalyst Photo-Electrochemical Behavior, Coatings **13**, 358 (2023). https://doi.org/10.3390/coatings13020358

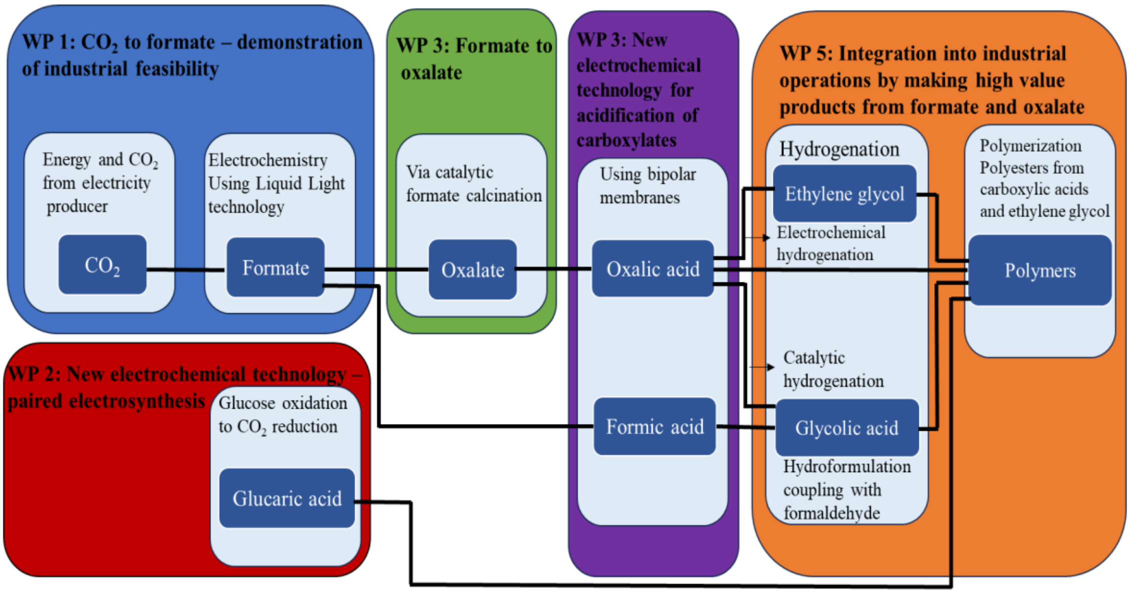

Figure 3.1: Schematic representation of the OCEAN project.

The OCEAN project intends to build an integrated method for producing high-value C_2 compounds from carbon dioxide, by using electrochemistry. This will be accomplished by 1) enhancing and optimizing a carbon dioxide-to-formate conversion technology. The OCEAN project will take this technology one step closer to commercialization by proving it at an industrial power provider's location, converting 250 g of CO_2 each hour. The energy efficiency will be increased by linking the cathodic reaction to the anodic oxidation of glucose, which will be accomplished by the use of a revolutionary technology that will match the kinetics of the processes at both electrodes. 2) The formate obtained will be transformed to oxalate, creating novel electrochemical methods to convert formate and oxalate to formic acid and oxalic acid, respectively. 3) New electrochemical techniques for converting oxalic acid to glycolic acid and other high-value C_2-products will be developed and compared to traditional hydrogenation. 4) Incorporating electrochemical technology into a manufacturing process for high-value C_2 products and polymers. 5) Demonstrating economic feasibility through market study, business case development, and exploitation plan. Overall, the OCEAN project aims to address the critical elements that are currently impeding the introduction of new electrochemical processes by targeting high-value products with the corresponding production margins, lowering power costs, and a trans-disciplinary approach that is required for the introduction of these advanced technologies.

In particular, at the University of Messina, scientific research was performed by focusing on the 3rd step: development and improvement of working electrode (cathode) synthesis for the reduction of oxalic acid.

3.2 Oxalic acid

Oxalic acid is currently used mostly for its capacity to capture metal cations, as a whitening agent, and as a preservative for agri-food items[6]. It is also being studied for use as solid CO_2 storage to prevent the transmission of liquid or supercritical anhydride carbon through ducts[7]. A considerable potential exists, however, in the variety of C_2, high interest industrial items that may be obtained from its reduction.

3.3 Electrocatalytic reduction of oxalic acid

According to literature[8,9], the major metals utilized as cathode were Hg and Pb. Because of the severe toxicity of these species, researchers are looking for alternative electrodes that adhere to green chemistry ideals.

Recently, the most used cathode is based on Ti, thanks to its features such as selectivity in redox processes, high stability, ease of synthesis and its environmental compatibility. The first catalysts used for this reaction had unordered TiO_2 nanoparticles on the surface. Afterwards, Zhao et al.[9] showed that a roughened TiO_2 film electrode, prepared by an anodic oxidation method, is a selective material in OX reduction. Nowadays, for improving the electrodes, titanium oxide nanotube arrays (TiNT) were synthesized.

The advantages are:

- Higher surface area: the ordered 3D structure permits the increase of the electrochemically active area of the electrode.

- Lower resistivity: TiNTs have higher conductivity than the oxide layer of the same thickness, in particular if calcinated to obtain anatase crystalline phase[10].

TiO_2 has several crystalline phases, which can result in significant changes in catalytic activity. Anatase and rutile are the two most prevalent phases. Rutile is the most stable phase thermodynamically, but as proven by Watanabe et al.[11], it is also the least effective in the reduction of oxalate in electrocatalytic processes, with anatase having the highest activity. This can be attributed to both structural and electronic factors. Because rutile and anatase have distinct conduction bands, the reduction potential of the electrons present in that band differs between the two crystalline phases. As seen in figure 3.2, the potential of the conduction band in rutile is somewhat lower than that of H^+ reduction, resulting in a stronger predisposition to the production of H_2 than anatase.

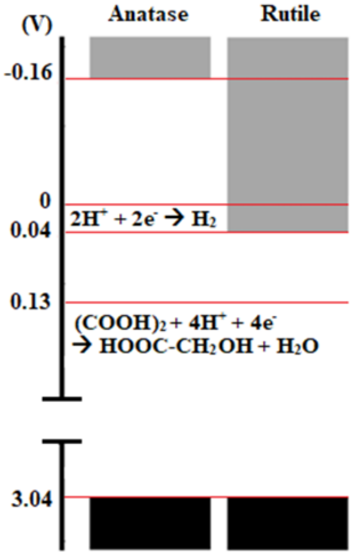

Figure 3.2: Energetic diagram of valence and conduction band of titanium oxide correlate to reduction potential of H_2 and oxalic acid.

Furthermore, the differing crystalline structure of the two phases causes the most exposed faces on the electrode surface to vary. In the case of rutile, it is primarily

(110), but in anatase (101), these two faces interact with the oxalate in a different way because the oxalate preferentially binds with just one carboxyl group on the face (101) of the anatase, making the other open to the reduction process.

3.4 Oxalic acid reduction reaction

The electrocatalytic reduction of OX is a four-electrons reduction reaction in which the electrons derive from the oxidation of water. Nevertheless, the reduction to GC occurs in two consecutive steps: first the OX is reduced into glyoxylic acid (GO) by acquiring two electrons, and then latter it is reduced into glycolic acid (GC) by two other electrons, shown in figure 3.3.

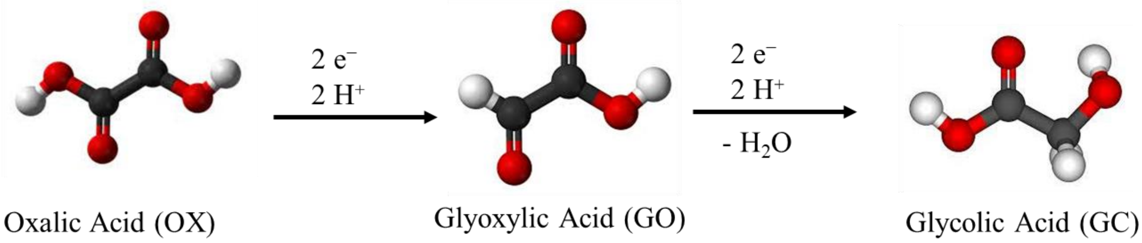

Figure 3.3: Consecutive steps for the reduction of Oxalic acid to Glycol acid.

By applying a potential equal to or greater than -1.1 V it is possible for the reaction to take place.

Cathode: $(COOH)_2 + 4H^+ + 4e^- \rightarrow HOOC\text{-}CH_2OH + H_2O$ +0.13 V vs RHE

Anode: $2H_2O \rightarrow 4H^+ + 4e^- + O_2$ +1.23 V vs RHE

Overall: $(COOH)_2 + H_2O \rightarrow HOOC\text{-}CH_2OH + O_2$ -1.1 V

The mechanism by which TiO_2 reduces OX is connected to the formation on the electrode surface of Ti^{3+} species, which allows the reduction of the species in solution while returning Ti^{3+} to Ti^{4+}. Zhao et al.[12,13] validated the occurrence of these species by comparing cyclic voltammetry in oxalic acid solution and electrolyte solution. There was no peak of interest observed in the first. Instead, an irreversible decreased peak of -1.1 V was linked with the reaction:

$$TiO_2 + H_2O + H^+ + e^- \leftrightarrow Ti(OH)_3 \qquad \text{(eq 3.1)}$$

This suggests that Ti^{3+} is rapidly oxidized by oxalic acid which is reduced to GO and then GC. This will be highlighted in cyclic voltammetry discussed later.

3.5 Product selectivity

It is feasible to adjust the selectivity of the process towards a certain reaction product (Glycolic acid or Glyoxylic acid) by changing the morphology of the electrode.

According to Zhao et al. [9], using an anodized titanium sheet formed of H_2SO_4, whose active phase is a thin layer of TiO_2, directs the reaction to GO. The same research group[13] later synthesized a TiO_2 catalyst functionalized with nanotubes (TiNT), getting higher performance but always with a glyoxylic acid predominance. In both cases, the electrocatalyst was not calcinated following anodic oxidation, which suggests that the amorphous phase may impede the advancement of OX reduction to GC.

Im et al.[14], for example, revealed that a possible feature of selectivity control is the length of the NTs. A shorter nanotube length would reduce the persistence of the substrate at the active surface, limiting the possibility of further reduction, particularly if accompanied by intense agitation.

Farkhondehfal et al.[15] studied three different TiO_2 nanostructures (nanotubes, nanoflames, and commercial nanopowder), in order to select the most performing catalyst in activity and selectivity for the oxalic acid reduction reaction. Among the different nanostructures, the best one was identified in TiO_2 nanotubes, reaching a Faradaic efficiency to GC of about 50% at a cell potential equal to 3 V.

Abramo et al. [16] determined that the presence of small amounts of amorphous TiO_2 on the surface of nanotubes is critical because:

- it increases the number of Ti^{3+} sites that are active in the reduction of OX due to its greater reducibility.
- it precludes sintering phenomena that would reduce the number of active sites.

The catalyst with the most selectivity towards GO was the one with a higher concentration of oxide on the surface, more difficult to release, and, in general, a little electrocatalytic activity.

In this framework, the effect of surface doping of titanium nanotubes by deposition of graphitic carbon nitrides (g-C_3N_4) was investigated.

3.6 Synthesis of electrocatalysts

The g-C_3N_4/TiNT composites were synthesized in two steps (see figure 3.4) using a method described in detail by Passalacqua et al.[17,18].

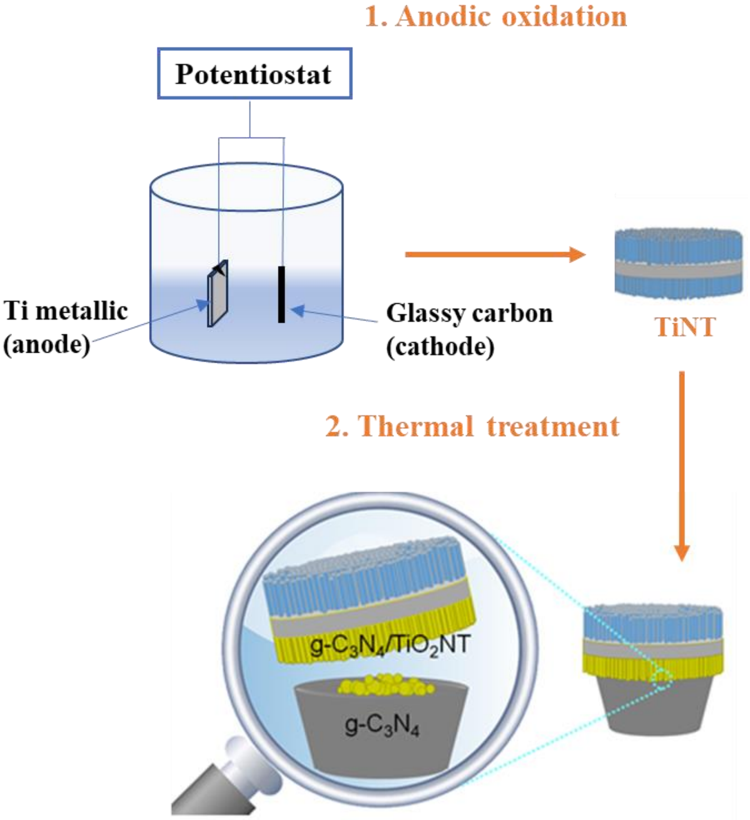

Figure 3.4: Schematic description of the two-step synthesis of g-C_3N_4/TiNT nanocomposites[19].

In the first stage, TiNT was synthesized via controlled anodic oxidation (AO) of a titanium foil[17]. Their synthesis is carried out in a room-temperature stirred electrochemical cell containing ethylene glycol, 0.3 wt% NH_4F, and 2 vol.% H_2O. A titanium foil (0.025 mm thickness, 35 mm diameter, 99.9% purity) was cleaned via sonication in deionized water, acetone, and isopropyl alcohol, then dried in an air stream before being anodized at 50V for 1 hour. The synthesis of anodized TiNT occurs through the simultaneous action of the electrochemical oxidation of Ti to TiO_2 (eq. 3.2) and the F^- driven chemical dissolution of TiO_2 (eq. 3.3), both caused by the electric field[20].

$$Ti + 2H_2O \rightarrow TiO_2 + 4H^+ + 4e^- \qquad \text{(eq 3.2)}$$

$$TiO_2 + 4H^+ + 6F^- \rightarrow [TiF_6]^{2-} + 2H_2O \qquad \text{(eq 3.3)}$$

The mechanism by which the TiNT synthesis takes place is divided into several phases and can be monitored by recording the change in current over time, as shown in figure 3.5.

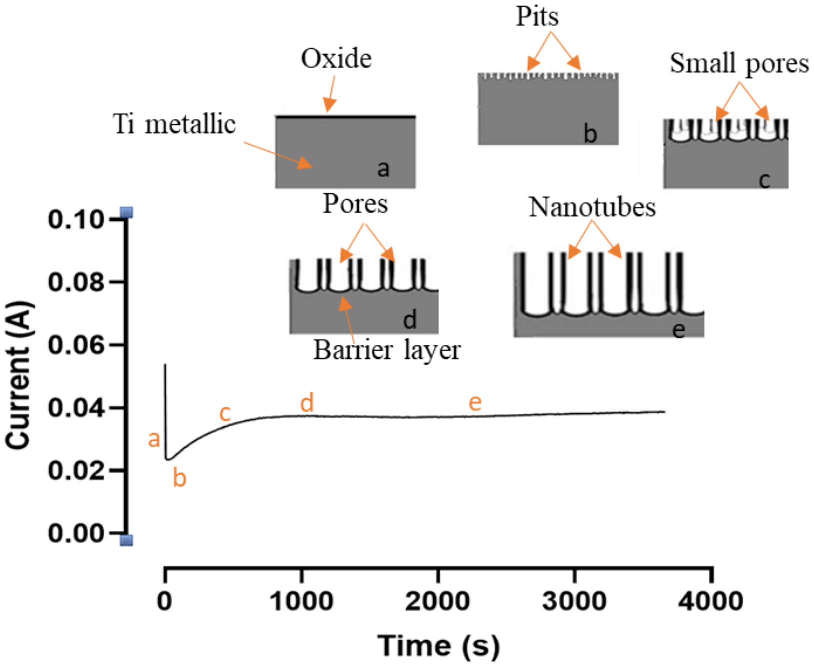

Figure 3.5: Change in current over time during the anodizing process and schematization of the nanotube production process.

Initially (figure 3.5 a) due to the applied electric field, there is the formation of a dense layer of non-conductive oxide on the plate that causes a sudden lowering of the current. The newly formed oxide layer is chemically attacked by F^- and small pores are formed very close to each other and arranged irregularly (figure 3.5 b). This phase is accompanied by an increase in the current due to the dissolution of the oxide. As the oxide layer thins, the depth of the pores increases both the intensity of the electric field, and thus the dissolution rate of the TiO_2, and the concentration of H^+ ions. Gradually the F^- ions, under influence of the electric field, first dissolve the walls of the small pores, obtaining others of greater diameter (figure 3.5 c), then dig the bottom of the pores obtaining voids and a tubular structure thanks to the simultaneous oxidation of Ti (figure. 3.5 d). When the speed of the two reactions is similar, the nanotubes no longer grow (figure 3.5 e)[21,22]. In this last phase there is a small fall of current due to the formation of irregular oxide particles on the top of the nanotubes[22]. As a result, self-organized TiNT layers grow on both sides of the metallic disc, which remains and provides the substrate conductivity to function as an electrode.

In the second step, the anodized TiNT was decorated with $g\text{-}C_3N_4$ using a direct chemical vapor deposition (CVD) process with melamine, urea, or a 1:1 combination of melamine and urea as the precursor. A certain amount of precursor ($6, 12, 18, 24\text{x}10^{-3}$ mol) was placed in a clean ceramic crucible with the anodized disk serving as a covering. The crucible was then heated in a muffle in air at 550 °C for 3 hours (heating rate 5° C/min) obtaining the deposition of the $g\text{-}C_3N_4$ polymer onto the top of the crystalline structure of TiNT.

3.7 Testing protocol

The setup of the electrochemical cell, where the experiments take place, is depicted in figure 2.3. A 0.2 M Na_2SO_4 solution with OX (oxalic acid) concentration of 0.03M (pH=2.7) is used to perform the reaction in the cathodic compartment, while the electrolyte solution (0.2 M Na_2SO_4) is used for the anodic compartment. In the latter, the pH was adjusted adding small amounts of a 1 M H_2SO_4 solution, to get the same pH of the cathode side. The cathode tank containing the electrolytic solutions are flowed with argon (20 ml/min) flow for 30 minutes to push the O_2 out, before starting the reaction. The electrolytic solutions are flushed to both compartments by using a peristaltic pump. The solution volume (cathode + external tank + tubes) is 35 ml and the net volume in the cathodic compartment is 7 ml, the same as in the anode. The experiments were performed by using the electrocatalysts reported in table 3.1 and as working electrode (WE), its geometric surface is about 6 cm^2.

Table 3.1: Tested electrocatalysts and their characteristics.

Sample name	**Chemical components**	**AO parameters**	**g-C_3N_4 precursors**
TiNT	TiO_2/Ti	50 V 1h	-
TiNTM6	g-C_3N_4 - TiO_2/Ti	50 V 1h	Melamine 6x10^{-3} mol
TiNTM12	g-C_3N_4 - TiO_2/Ti	50 V 1h	Melamine 12x10^{-3} mol
TiNTM18	g-C_3N_4 - TiO_2/Ti	50 V 1h	Melamine 18x10^{-3} mol
TiNTM24	g-C_3N_4 - TiO_2/Ti	50 V 1h	Melamine 24x10^{-3} mol
TiNTU6	g-C_3N_4 - TiO_2/Ti	50 V 1h	Urea 6x10^{-3} mol
TiNTU12	g-C_3N_4 - TiO_2/Ti	50 V 1h	Urea 12x10^{-3} mol
TiNTU18	g-C_3N_4 - TiO_2/Ti	50 V 1h	Urea 18x10^{-3} mol
TiNTU24	g-C_3N_4 - TiO_2/Ti	50 V 1h	Urea 24x10^{-3} mol
TiNTMU6	g-C_3N_4 - TiO_2/Ti	50 V 1h	1:1 Melamine-Urea 6x10^{-3} mol
TiNTMU12	g-C_3N_4 - TiO_2/Ti	50 V 1h	1:1 Melamine-Urea 12x10^{-3} mol
TiNTMU18	g-C_3N_4 - TiO_2/Ti	50 V 1h	1:1 Melamine-Urea 18x10^{-3} mol
TiNTMU24	g-C_3N_4 - TiO_2/Ti	50 V 1h	1:1 Melamine-Urea 24x10^{-3} mol

Cyclic voltammetry (CV) in the potential range from 0 to -2 V and scan rate of 10 mV/sec was carried out in electrolyte solutions with and without OX substrate, respectively. By these CV experiments the onset potential of OX reduction on the WE was evaluated and used as fixed potential for the amperometric detection experiments.

The amperometric detection experiments were performed at constant applied voltage in the range of -1.1 ÷-1.3 V vs Ag/AgCl, monitoring the current density. In the anodic compartment, the H^+ are generated in situ by water co-electrolysis. They move through the Nafion membrane to reach the cathodic side where the reduction reaction occurs. The test was carried out for 2 hours per each potential investigated. The products were analyzed using an ion chromatograph. The analyses were performed on a Metrohm ion chromatograph with a mobile phase of H_2SO_4 0.05 mm, a flow rate of 0.05 ml/min, and an average pressure of 5 MPa, and a stationary phase of a column for organic acids 25 cm long and with an internal diameter of 7.8 mm, preceded by a Metrosep Organic Acid Guard pre-column 50 mm long and 4 mm thick. At 215 nm, a 944 professional UV/vis Detector Vario detector was utilized to detect the products.

3.8 Cyclic voltammetry

The electrodes were investigated by CV[23–25] to define their redox behavior. Figure 3.6 shows the cyclic voltammetry in blank solution (0,2M Na_2SO_4, and some drops of H_2SO_4 to reach pH=2.7) of pristine TiNT and a representative g-C_3N_4 sample (TiNTM6), considering that all CVs are similar among them.

According to eq 3.4, a reversible reduction peak at -1.2 V vs Ag/AgCl was identified and was attributable to the redox pair $Ti^{4+/}Ti^{3+.}$

$$TiO_2 + H_2O + H^+ + e^- \rightarrow Ti(OH)_3 \qquad \text{(eq. 3.4)}$$

According to eq 3.5, the production of gaseous hydrogen begins around -1.60 V vs Ag/AgCl. The recorded negative current in this area is because of this reaction.

$$2H_2 + 2e^- \rightarrow H_2 \qquad \text{(eq. 3.5)}$$

Also, an anodic peak between -0.8 and -0.9 V vs Ag/AgCl is noticed, which is ascribed to Ti^{3+} oxidation to Ti^{4+}. The peak intensity might indicate the number of Ti^{3+} species.

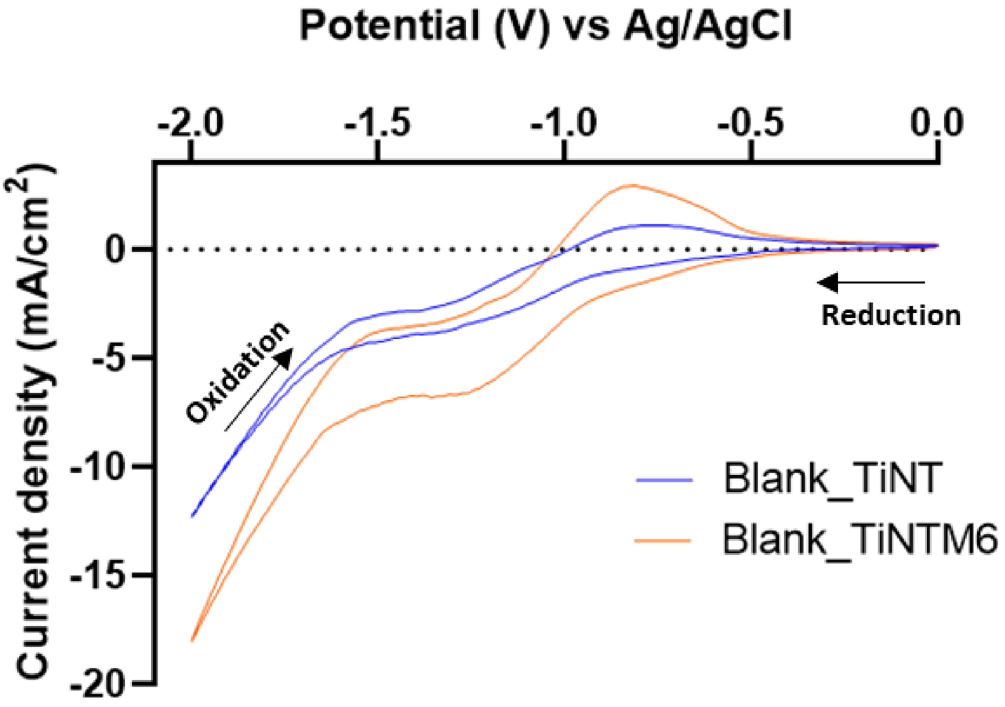

Figure 3.6: Cyclic Voltammograms recorded from 0V to -2V vs Ag/AgCl in blank solution (0,2M Na_2SO_4, and some drops of H_2SO_4 to reach pH=2.7) of pristine TiNT (blue curve), and TiNTM6 (orange curve) at 50 mV/s.

CVs recorded in OX solution (0.03 M oxalic acid, and 0,2M Na_2SO_4), depicted in figure 3.7, show that the anodic peaks become much less intense due to the decreased oxidation of Ti^{3+} species, while the cathodic current somewhat rises.

According to Zhao et al.[9], who found comparable behavior on a rough TiO_2 layer, a probable explanation for the decrease in Ti^{3+} in oxalic acid solution is that the electrogenerated Ti^{3+} species lowers OX because it is the active site of reduction.

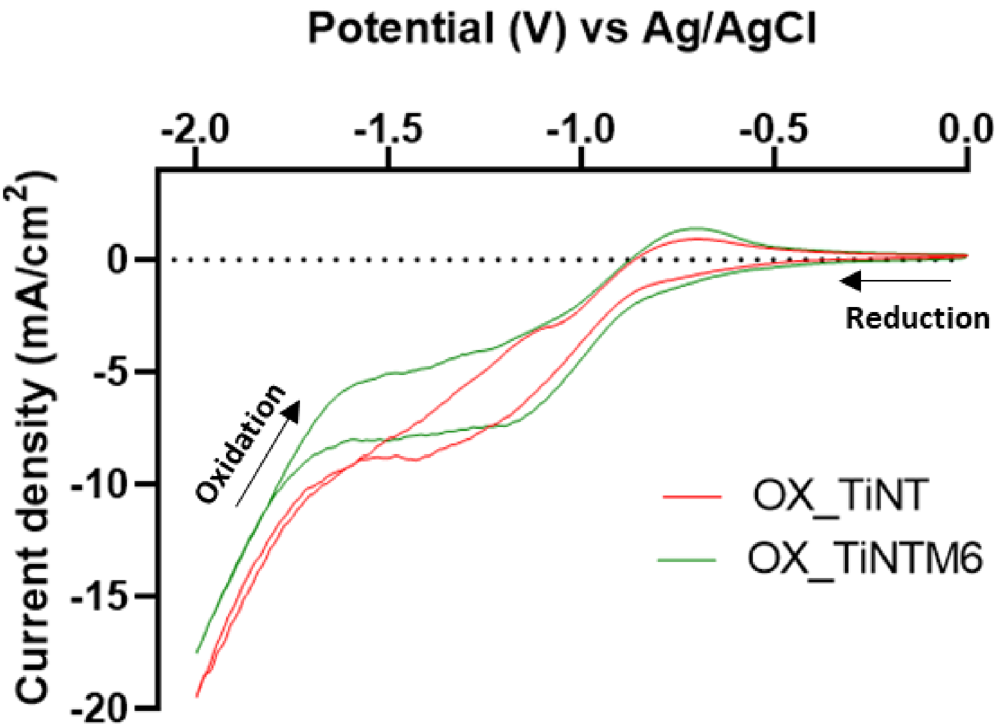

Figure 3.7: Cyclic Voltammograms recorded from 0V to -2V in OX solution (0,03M oxalic acid, and 0.2M Na_2SO_4 - pH=2.7) of pristine TiNT (red curve), and TiNTM6 (green curve) at 50 mV/s.

3.9 Characterization of the g-C_3N_4/TiNT composite material

The crystallographic phases of the g-C_3N_4/TiNT composites were determined by X-ray diffraction (XRD). The XRD spectra of thin film samples of nanotubes covered with graphitic carbon nitride were obtained using a Philips X'Pert 3710 instrument using Cu K radiation (λ= 0.154178 nm, 30 kV, and 40 mA) at a glancing angle of 2°. Lower angles were employed for a smaller sampling depth of the X-rays to increase the intensity of reflections deriving from the thin film while minimizing the contribution related to the underlying Ti substrate. Diffractograms were acquired in the 2θ angle from 10 to 80°. Except for urea-derived species, the yellow powders of g-C_3N_4 collected in the crucible after thermal treatment were also analyzed by a Bruker D2 Phaser desktop X-ray diffraction system (Bruker AXS GmbH, Karlsruhe, Germany) operating with the conventional Bragg-Brentano geometry. Diffraction peaks were identified by comparing them to patterns in the JCPDS database of reference chemicals.

To evaluate the morphology of the composites and related CN_x powders, micrographs of the composites and CN_x powders were acquired using a Phenom benchtop SEM.

X-ray photoelectron spectroscopy (XPS) provided evidence about the production of carbon nitride polymers as well as additional insights into the nature of the surface of the g-C_3N_4/TiO_2 composites. PHI Versa Probe II equipment was used for XPS measurements. The survey C1s, O1s, N1s, and Ti2p spectra were obtained using an Al K α (1486.6 eV) X-ray source and an analyzer pass energy of 23.5 eV and 117 eV, respectively, for the high-resolution core-level spectra and the survey spectrum.

3.10 Results and discussion

TiNTs were grown using a previously established method[17,18]. The g-C_3N_4/TiNT composites were synthesized using the polycondensation technique in a single synthesis step that included pyrolysis and condensation of nitrogen precursors as well as crystallization of the titania nanotube film. In the initial step of anodic oxidation of the metallic titanium substrate, the latter layer was formed in an amorphous form. Melamine rearrangements produced tris-s-triazine at around 390° C, and condensation of this unit to the final polymeric C_3N_4 species happened at around 520 °C [26].

The crystallographic phases and structure of the synthesized materials were determined by X-ray diffraction, which confirmed the production of the usual graphite-like stacking of C_3N_4 layers in all samples[27,28]. The XRD patterns of (i) MU24 and (ii) M24 produced from g-C_3N_4 powders, (iii) M18, (iv) MU18, and (v) U18 of g-C_3N_4/TiNT composites, and (vi) TiO_2 nanotubes array formed on Ti are shown in Figure 3.8.

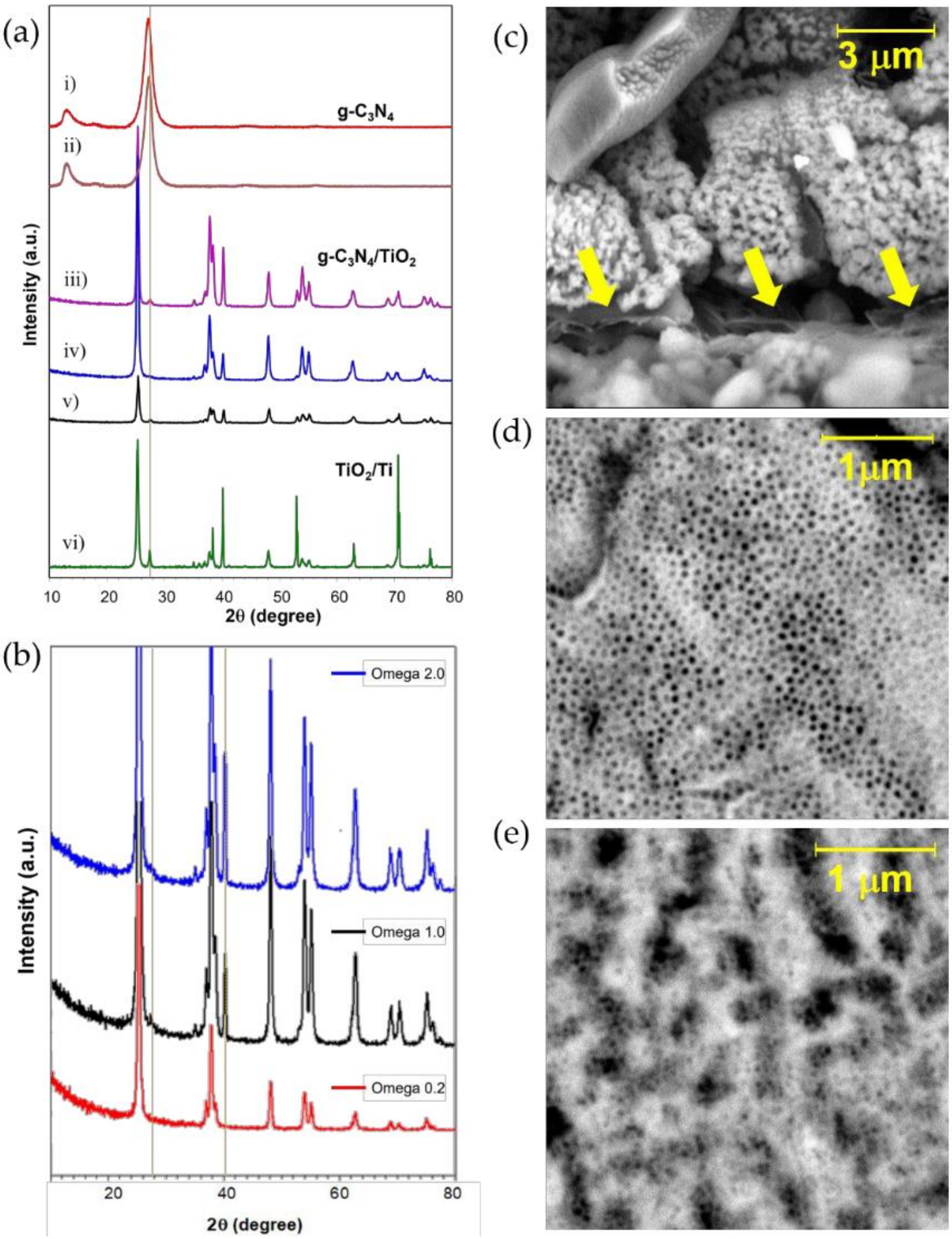

Figure 3.8 (a) XRD profiles. (i and ii) g-C_3N_4 MU24 and M24 precursor powders after the thermal treatment; (iii–v) Melamine-, Melamine–Urea-, and Urea-derived g-C_3N_4/TiNT-U18 composites recorded with a 2° glancing angle; (vi) TiNT support[18]; (b) GAXRD patterns of the TiNT-MU18 electrode were acquired by decreasing the incident angle ω from 2.0 to 0.2°. (c) SEM micrograph of g-C_3N_4 powder obtained from M18 precursor. The arrows in (c) indicate the layered graphitic structures. SEM micrographs of (d) TiNT and (e) TiNT-M18 sample.

The nanotube arrays are mostly anatase phase. A small amount of rutile is present, and it is mostly situated at the interface between the TiNTs bottom and the Ti substrate, as demonstrated in Figure 3.8 b by the comparison of XRD recorded in glancing angle mode. In fact, in the MU18-TiNT pattern, by reducing the incidence angle from 2.0° to 0.2° and hence the depth of X-ray penetration, the rutile phase diffraction peaks at 27.5° and 40° disappear. The XRD patterns of melamine, urea (not reported), and the equimolar ratio of the melamine-urea sample recovered in the crucible coupled with the appropriate composites revealed two peaks in bare g-C_3N_4 powders. The tri-s-triazine ring's in-plane structural packing motif was ascribed to the first peak at 13.08°. For graphitic materials, it was indexed to the (100) diffraction plane. The conjugated aromatic system's interlayer stacking was connected to the greatest peak at 27.36° classified as (002) diffraction plane. The peaks in graphitic C_3N_4 produced from 1:1 melamine-urea were somewhat displaced towards lower angles, 12.92° and 27.26°, with a substantial widening and a minor drop in overall intensity.

These characteristics are typical of g-C_3N_4 MU-derived species with conjugated aromatic layers that are well separated as compared to single precursor samples TiNT-M18 and TiNT-U18, resulting in higher photocatalytic activity. The main peak at 25.38, 25.42, and 25.34 in the composite diffraction pattern can be indexed to the (101) crystal plane of anatase (JCPDS file No. 21-1272), while the reflection of lower intensity found at 2 values of 27.50, 27.54, and 27.50, for M-, U-, and MU- derivatives, respectively, can be indexed to the (110) crystal plane of rutile (JCPDS card No. 21-1276). Rutile diffraction signals were low in intensity, while graphitic carbon signals were practically the same value of 2θ, suggesting that the two diffraction peaks might overlap. A thorough analysis revealed that the rutile peak was at 27.50° and that of the g-C_3N_4 system, which was associated with the unusual peak of the (002) crystal plane, was at 27.36°.

Scanning electron microscopy (SEM) was used to characterize the morphology of the materials (see Figure 3.8 d for the TiNT-M18 composite and Figure 3.8e for the corresponding TiNT substrate). When the micrographs were compared, it was discovered that the clean titania substrate had tubes with open tops. Simultaneously, the composites were covered by layered graphitic materials that appeared as veiled top surfaces. In the bulk powder, the characteristic CN_x layered structures were more clearly evident, as illustrated in Figure 3.8 c and indicated by arrows.

To confirm the chemical composition and valence states of the prepared samples, XPS measurements were used to analyze the electronic structure of the g-C_3N_4/TiNT composite materials. The survey spectra revealed the presence of Ti, O, C, and a trace of N in all of the processed samples (see Figure 3.9), demonstrating that the preparation procedure's aim was met.

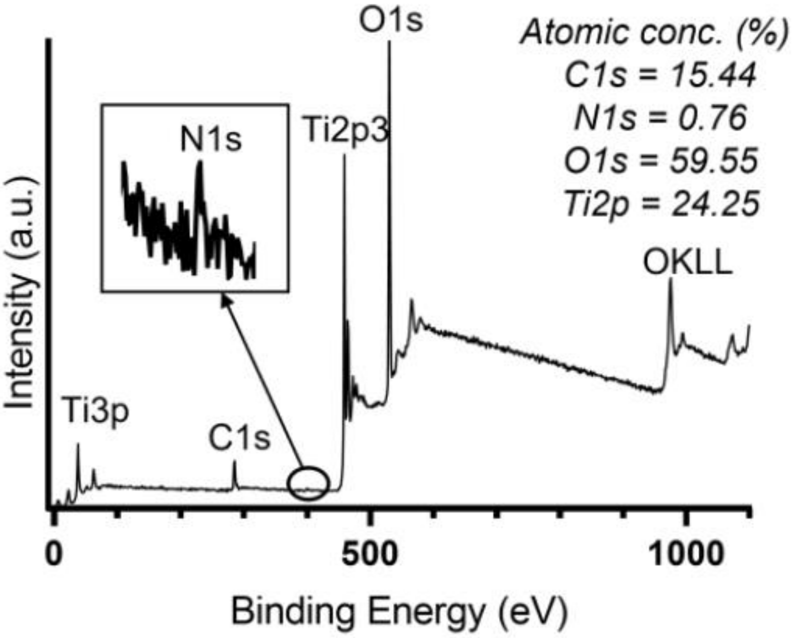

Figure 3.9: Survey XPS spectrum of the TiNT-U24 sample.

Figure 3.9 depicts the survey spectrum obtained for the TiNT-U24 sample, together with the atomic percentages for the single components C, N, O, and Ti. All of the other samples exhibited identical behavior, although their spectra are not included here for clarity.

The level of nitrogen in all of the samples tested was less than 1% wt. The electrical structure of the powder generated during the preparation of the composite electrodes was also studied for the highest precursor amount (24x10^{-3} mol) for which sufficient powder was recovered after synthesis. The fitted C1s and N1s spectra of the powder samples are shown in Figures 3.10 a, b.

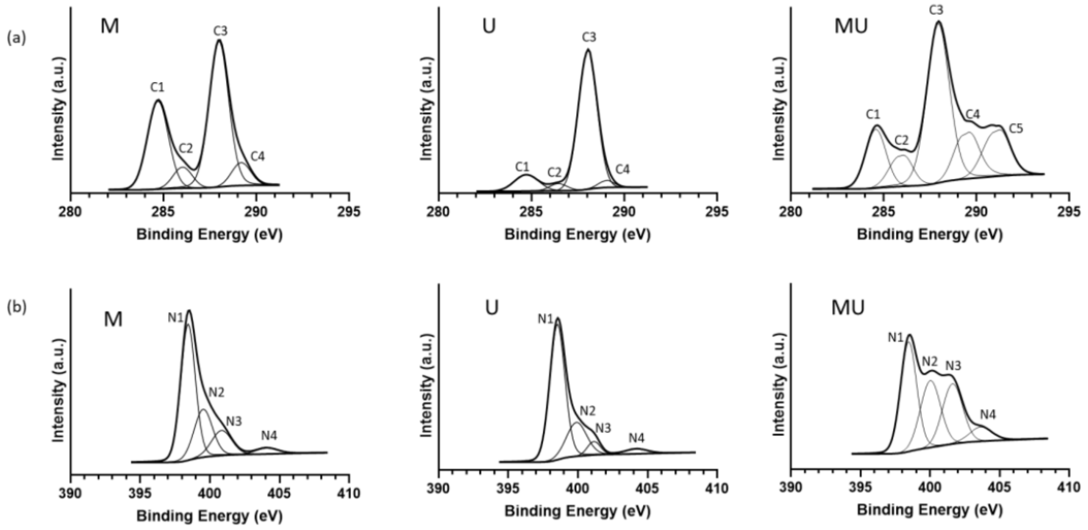

Figure 3.10: XPS spectra of powder prepared from 24x10^{-3} mol Melamine (M), Urea (U), and mixed (MU) precursors: (a) C1s and (b) N1s.

Carbon nitride with the chemical formula C_3N_4 is used to define the species nature. All C1s spectra revealed an asymmetric peak (C1) with a binding energy of 284.7 eV, which was ascribed to graphitic carbon C=C bonds. The N=C-N groups of triazine rings were responsible for the big and stronger peak (C3) at 288.1 eV[29,30]. The existence of C atoms in severely deficient sp^2 carbon phase and edge terminated C=N or C=O species was suggested by the significant full width at half maximum (FWHM) (1.35) of the C1 component[30]. Analyzing samples obtained with a single precursor yielded two weak peaks. The first, at 286.2 eV, is ascribed to C=N or C=O in graphitic carbon, while the second, at 289.1 eV, is due to C-O, which is presumably generated by oxidation of the sample exposed to air[29,31].

The related N1s (Figure 3.10 b) revealed four components: pyridine-like C=N species (N1 at 398.5 eV), conjugated amine C=N-H species (N2 at 399.8 eV), quaternary N (N3 at 401 eV), and a NOx species (N4 at 404 eV). According to the literature[30], the examined material was a dispersed heptazine-based carbon nitride. When a mixed precursor was utilized, the C1s spectra revealed the presence of a new component C5 at 291.0 eV, which was ascribed to a shake-up satellite found in samples with high defective carbon sp2 content[32]. The N1s spectra suggested an important rise in the amount of C=N-H and quaternary N species despite a decrease of pyridine-like species C=N in the synthesized sample with a single precursor, highlighting that a mixed precursor produced a more equally distributed N-species with an elevated percentage of defective sp^2 carbon phase. The Ti2p spectra for the composites prepared with the greatest precursor amount (24x10^{-3} mol) are shown in Figure 3.11 a in comparison to the reference TiNT array.

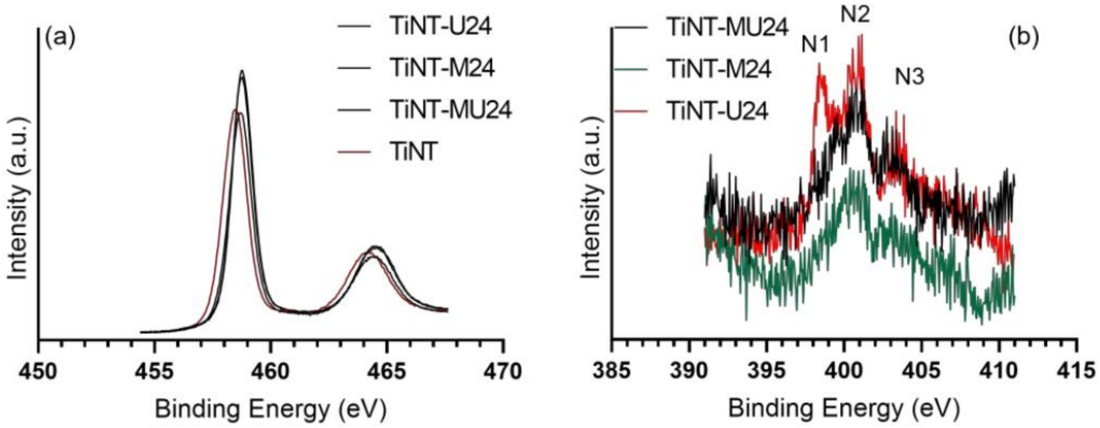

Figure 3.11: Comparison of (a) Ti2p and (b) N1s high-resolution XPS spectra of composites prepared from 24*10^{-3} mol of precursors.

A shift in higher binding energy to pure TiNT was found in all of the composite materials, demonstrating an interaction between the CN$_x$ and TiNT. The observed shift in the Ti signal in the composites showed contact between g-C_3N_4 and TiNTs, as well as an enhanced electron density on Ti consistent with a transfer of charge from the electron-rich g-C_3N_4 surface to the empty orbital of Ti^{4+}[33]. The observed shift in the Ti2p spectra in the composite materials with regard to TiNT shows that depending on the employed precursor, a distinct interaction between nanotubes and g-C_3N_4 was produced. This finding supports the interaction of the two components and, as a result, the successful formation of the heterojunctions. The shift was around 0.23 eV with regard to TiNT for both the TiNT-UM24 and TiNT-U24 samples, and 0.17 eV compared to the TiNT reference for the TiNT-M24 sample.

The deconvolution of N1s spectra was not performed because of the low quantity of N and hence poor signal strength. Nonetheless, the spectra shown in Figure 3.11 b demonstrate the three primary components detected in the g-C_3N_4 powder, N1, N2, and N3. It is crucial to note that these results are consistent with those obtained in our earlier research by utilizing a lower amount of the precursors[34] and with those published in the literature for similar systems[33,35].

The as-prepared g-C_3N_4-TiNT samples, reported in table 3.1, were tested in the three-electrodes electrochemical cell, depicted in figure 2.3, for the electrocatalytic reduction of oxalic acid. They performed as selective cathodic electrodes, forming glyoxylic acid (GO) and glycolic acid (GC). The OX reduction reaction occurs in two steps. (i) OX is reduced to GO in a two-electron transfer, and then (ii) GC is produced from GO in a second two-electron reduction step. The used electrons came from the water oxidation reaction that occurs at the anode side.

Figure 3.12 shows an overview of the results at applied potentials (-1.1 V, -1.2, and -1.3 V against Ag/AgCl).

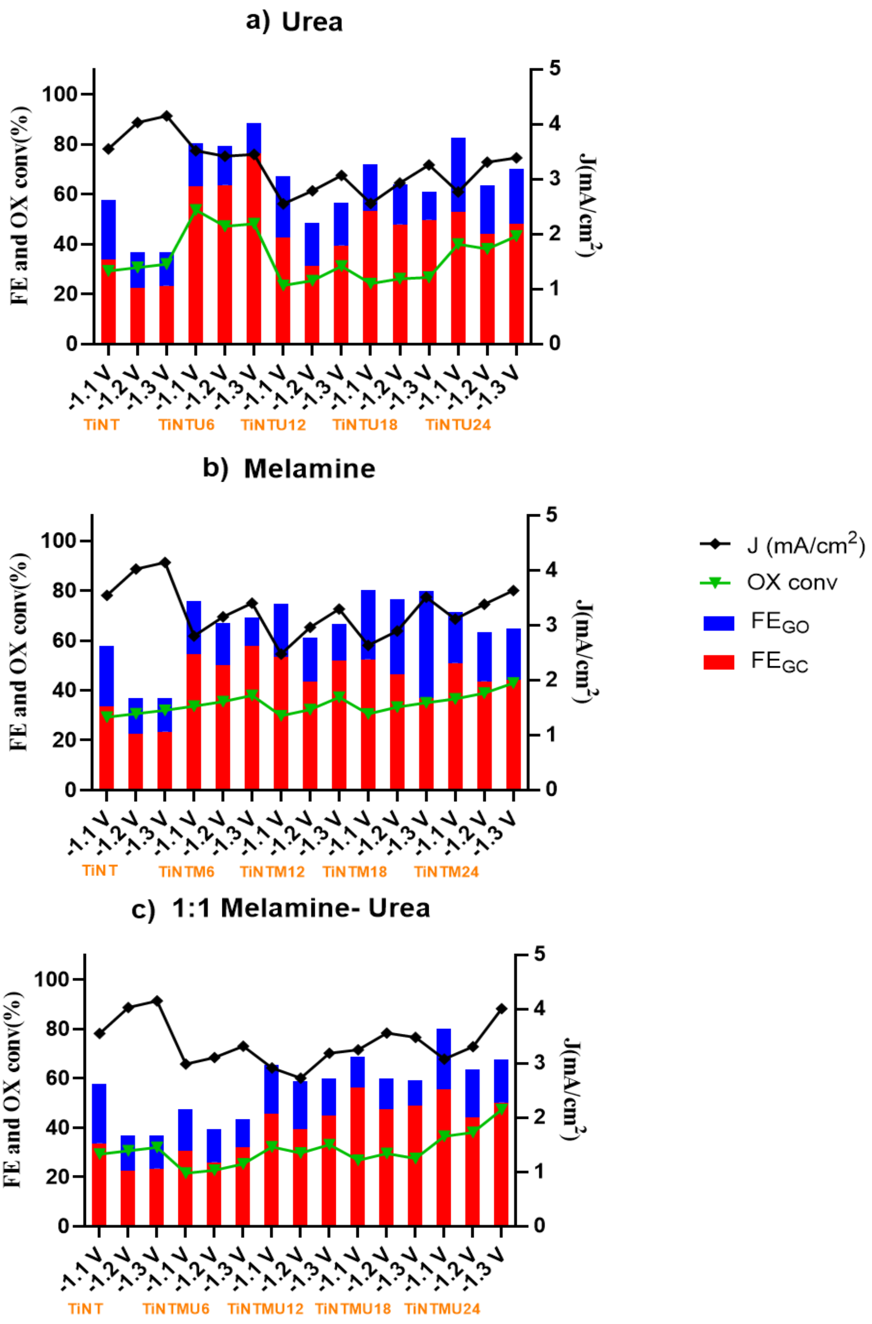

Figure 3.12: Faradaic efficiency to GO and GC, Ox conversion and current density of g-C_3N_4/TiNT composites and TiNT reference sample at the potential of -1.1 V, -1.2 V, and -1.3 V vs Ag/AgCl after 2 h of reaction. a) TiNTUx composites compared with pristine TiNT data, b) TiNTMx composites compared with pristine TiNT data, and c) TiNTMUx composites compared with pristine TiNT data.

After 2 hours of reaction, the faradaic efficiencies (FE) for each examined potential are given and compared to those produced by pristine TiNT. The faradaic efficiencies of pristine TiNT are similar for GO (FE_{GO}) and GC (FE_{GC}), with yields of around 24% and 34%, respectively. For all the investigated electrodes, as clearly shown in figure 3.12 a, b and c, an increase in FE_{GC} is seen after deposition of g-C_3N_4, while FE_{GO} remains comparable or decreases with respect to the pristine TiNT at the tested potentials. Except for the TiNTU6, which has the greatest FE_{GC} =76.3% and extremely low FE_{GO} =12.3% at an applied potential of -1.3 V, the best FE performances were found at an applied potential of -1.1 V.

In terms of best performance, the impact of using different precursors may be stated as follows:

TiNTU6 > TiNTMU18 > TiNTM6

For a better understanding of the data, they are listed in table 3.2.

These findings highlight the ability of the g-C_3N_4 dispersed layer to affect the selectivity of composite materials in favor of the GC as the principal product of the OX reduction reaction. In addition, the current density for the tested electrodes is slightly lower than for the pristine TiNT (Figure 3.12 a,b, and c), indicating that g- C_3N_4 acts primarily as a selectivity modifier rather than as a catalytic element.

The graphs, in Figure 3.13, correlate the FE_{GO}, FE_{GC} and OX conversion with the different precursors and amount (from $6x10^{-3}$ to $24x10^{-3}$ mol).

For example, the melamine-urea (MU) precursor is shown in Figure 3.13 a. By increasing the MU precursor amount, both FE_{GC} and OX conversion rise, but FE_{GO} remains relatively steady. This indicates that when the amount of MU precursor increases, additional selection sites are formed. The graphs in figure 3.13 b and c show an opposite trend for the urea (U) and melamine (M) precursors, respectively. When the M or U amount is increased, the FE_{GC} decreases while the EF_{GO} increases, implying that when a single precursor is utilized, a very low amount is necessary to tune the selectivity to GC. U precursor is more performing at low load.

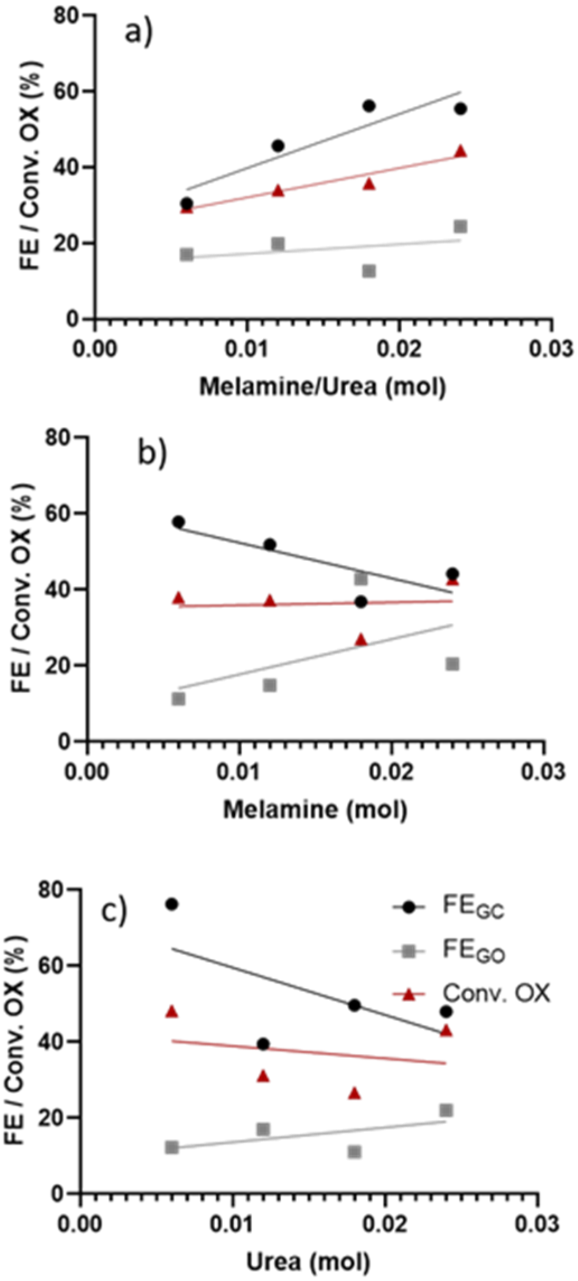

Figure 3.13: Attempts at correlation between FE_{GO}, FE_{GC}, and OX conversion as a function of precursor amount, a) Melamine/Urea, b) Melamine, and c) Urea.

Table 3.2: Results of tested working electrodes

WE	**E (V vs Ag/AgCl)**	**FE$_{GC}$ (%)**	**FE$_{GO}$ (%)**	**OX conv (%)**	**J (mA/cm^2)**
TiNT	-1,1	33,7	24,1	29,3	-3,55
TiNT	-1,2	22,4	14,5	30,7	-4,03
TiNT	-1,3	23,4	13,5	32	-4,15
TiNTU6	-1,1	63,1	17,4	53,7	-3,52
TiNTU6	-1,2	63,7	15,5	47,2	-3,42
TiNTU6	-1,3	76,3	12,3	48,2	-3,45
TiNTU12	-1,1	42,6	24,7	23,5	-2,55
TiNTU12	-1,2	31,3	17,2	25,4	-2,79
TiNTU12	-1,3	39,5	17	31,2	-3,07
TiNTU18	-1,1	53,1	18,9	24,2	-2,56
TiNTU18	-1,2	47,9	16	26,2	-2,93
TiNTU18	-1,3	49,7	11,1	26,7	-3,26
TiNTU24	-1,1	52,8	29,8	40	-2,77
TiNTU24	-1,2	45,7	25,2	43,1	-3,24
TiNTU24	-1,3	48	22	43,2	-3,39
TiNTM6	-1,1	54,6	21,1	33,7	-2,81
TiNTM6	-1,2	50,2	16,7	35,5	-3,16
TiNTM6	-1,3	57,9	11,3	38	-3,41
TiNTM12	-1,1	53,6	21,2	29,8	-2,48
TiNTM12	-1,2	43,4	17,7	32,3	-2,97
TiNTM12	-1,3	51,9	14,9	37,3	-3,3
TiNTM18	-1,1	52,5	27,8	30,6	-2,64
TiNTM18	-1,2	46,3	30,2	33,3	-2,9
TiNTM18	-1,3	36,9	42,9	35,1	-3,52
TiNTM24	-1,1	51	20,3	36,6	-3,12
TiNTM24	-1,2	43,7	19,6	38,9	-3,39
TiNTM24	-1,3	44,2	20,5	42,9	-3,64
TiNTMU6	-1,1	30,5	17	21,6	-2,99
TiNTMU6	-1,2	26	13,5	22,8	-3,11
TiNTMU6	-1,3	31,9	11,6	25,3	-3,32
TiNTMU12	-1,1	45,7	19,9	32,2	-2,92
TiNTMU12	-1,2	39,5	19,5	29,7	-2,73
TiNTMU12	-1,3	45	15,1	33,1	-3,19
TiNTMU18	-1,1	56,2	12,7	26,8	-3,25
TiNTMU18	-1,2	47,3	12,8	29,6	-3,56
TiNTMU18	-1,3	49	10,1	27,5	-3,48
TiNTMU24	-1,1	55,5	24,4	36,5	-3,08
TiNTMU24	-1,2	44	19,5	38,1	-3,31
TiNTMU24	-1,3	50,2	17,5	47,3	-4,01

3.11 Conclusion

In summary, the results demonstrate the capacity of the composite materials g-C_3N_4 dispersed layer to affect the selectivity toward GC as the principal product in the oxalic acid electrocatalytic reduction reaction. Notably, the sample TiNTU6 (obtained by employing a lower urea load of $6*10^{-3}$ mol) exhibits the highest FE_{GC} of about 76%, but the FE_{GO} is decreased approximately to 12%, when compared to the pristine TiNT, which exhibits FE_{GO} and FE_{GC} of around 24% and 34%, respectively. The XPS results show that the interaction between the g-C_3N_4 and TiNT is substantially dependent on the precursor and its amount, implying that the electroreduction of oxalic acid is dependent on this component. These findings are highly encouraging, given that comparable values are normally only achievable at a higher applied potential[36,37]. These results have aided in the identification of cathodic materials with properties suited for electrocatalytic reduction of oxalic acid.

Bibliography

1. Lanzafame, P. *et al.* Beyond Solar Fuels: Renewable Energy-Driven Chemistry. *ChemSusChem* **10**, 4409–4419 (2017).
2. Mustafa, A., Lougou, B. G., Shuai, Y., Wang, Z. & Tan, H. Current technology development for CO2 utilization into solar fuels and chemicals: A review. *J. Energy Chem.* **49**, 96–123 (2020).
3. Abdel-Mageed, A. M. & Wohlrab, S. Review of CO2 reduction on supported metals (Alloys) and single-atom catalysts (SACs) for the use of green hydrogen in power-to-gas concepts. *Catalysts* **12**, (2022).
4. Zhang, G. *et al.* Selective CO2 electroreduction to methanol via enhanced oxygen bonding. *Nat. Commun.* **13**, 1–11 (2022).
5. Li, L., Ma, D. K., Qi, F., Chen, W. & Huang, S. Bi nanoparticles/Bi 2 O 3 nanosheets with abundant grain boundaries for efficient electrocatalytic CO 2 reduction. *Electrochim. Acta* **298**, 580–586 (2019).
6. Pan, X., Wu, H., Lv, Z., Yu, H. & Tu, G. Recovery of valuable metals from red mud: A comprehensive review. *Sci. Total Environ.* **904**, 166686 (2023).
7. Breunig, H. M., Rosner, F., Lim, T. H. & Peng, P. Emerging concepts in intermediate carbon dioxide emplacement to support carbon dioxide removal. *Energy Environ. Sci.* 1821–1837 (2023) doi:10.1039/d2ee03623a.
8. Huang, T., Chen, S. P., Zhou, Z. Y. & Sun, S. G. Investigation of electrocatalytic reduction of oxalic acid on Pb electrode through in situ FTIR reflection spectroscopy. *Guang Pu Xue Yu Guang Pu Fen Xi/Spectroscopy Spectr. Anal.* **28**, 547–550 (2008).
9. Zhao, F., Yan, F., Qian, Y., Xu, Y. & Ma, C. Roughened TiO 2 film electrodes for electrocatalytic reduction of oxalic acid to glyoxylic acid. *J. Electroanal. Chem.* **698**, 31–38 (2013).

10. Tighineanu, A., Ruff, T., Albu, S., Hahn, R. & Schmuki, P. Conductivity of TiO2 nanotubes: Influence of annealing time and temperature. *Chem. Phys. Lett.* **494**, 260–263 (2010).

11. Watanabe, R., Yamauchi, M., Sadakiyo, M., Abe, R. & Takeguchi, T. CO2-free electric power circulation via direct charge and discharge using the glycolic acid/oxalic acid redox couple. *Energy Environ. Sci.* **8**, 1456–1462 (2015).

12. Sadakiyo, M., Hata, S., Fukushima, T., Juhász, G. & Yamauchi, M. Electrochemical hydrogenation of non-aromatic carboxylic acid derivatives as a sustainable synthesis process: From catalyst design to device construction. *Phys. Chem. Chem. Phys.* **21**, 5882–5889 (2019).

13. Electrode, S. T. N., Yang, Q., Fengming, Z., Qingqing, Q. & Chun-an, M. Electrocatalytic Hydrogenation Of Oxalic Acid To Glyoxylic Acid On A Self-Organized Tio 2 Nanotube Electrode Qian Yang, Zhao Fengming, Qiu Qingqing and Ma Chun-an*. **936**, 965–969 (2014).

14. Im, S., Saad, S. & Park, Y. Electrochemistry Communications Facilitated series electrochemical hydrogenation of oxalic acid to glycolic acid using TiO 2 nanotubes. *Electrochem. commun.* **135**, 107204 (2022).

15. Farkhondehfal, M. A., Savino, U., Chiodoni, A., Pirri, C. F. & Sacco, A. Electrocatalytic Reduction of Oxalic Acid Using Different Nanostructures of Titanium Oxide. *Electrocatalysis* **14**, 195–201 (2023).

16. Abramo, F. P. *et al.* Electrocatalytic production of glycolic acid via oxalic acid reduction on titania debris supported on a TiO2 nanotube array. *J. Energy Chem.* **68**, 669–678 (2021).

17. Passalacqua, R., Ampelli, C., Perathoner, S. & Centi, G. Self-standing TiO2 nanotubular membranes for sustainable production of energy. *Chem. Eng. Trans.* **41**, 319–324 (2014).

18. Passalacqua, R., Abate, S., Perathoner, S. & Centi, G. Improved nanocomposite photoanodes by controlled deposition of g-C3N4 on titania nanotube ordered films. *Chem. Eng. Trans.* **84**, 25–30 (2021).

19. Passalacqua, R., Abate, S., Luca, F. De, Perathoner, S. & Centi, G. Graphitic Layered Structures Enhancing TiNT Catalyst Photo-Electrochemical Behaviour. 1–18 (2023).

20. Centi, G. *et al.* Oxide thin films based on ordered arrays of 1D nanostructure. A possible approach toward bridging material gap in catalysis. *Phys. Chem. Chem. Phys.* **9**, 4930–4938 (2007).

21. Bai, J. *et al.* The formation mechanism of titania nanotube arrays in hydrofluoric acid electrolyte. *J. Mater. Sci.* **43**, 1880–1884 (2008).

22. Ampelli, C. *et al.* Synthesis of TiO2 thin films: Relationship between preparation conditions and nanostructure. *Top. Catal.* **50**, 133–144 (2008).

23. Sugiawati, V. A., Vacandio, F., Galeyeva, A., Kurbatov, A. P. & Djenizian, T. Enhanced Electrochemical Performance of Electropolymerized Self-Organized TiO2 Nanotubes Fabricated by Anodization of Ti Grid. *Front. Phys.* **7**, 1–8 (2019).

24. Fabregat-Santiago, F., Mora-Seró, I., Garcia-Belmonte, G. & Bisquert, J. Cyclic voltammetry studies of nanoporous semiconductors. Capacitive and reactive properties of nanocrystalline TiO2 electrodes in aqueous electrolyte. *J. Phys. Chem. B* **107**, 758–768 (2003).

25. Makivić, N. *et al.* Evidence of Bulk Proton Insertion in Nanostructured Anatase and Amorphous TiO2Electrodes. *Chem. Mater.* **33**, 3436–3448 (2021).

26. Schlo, R. *et al.* Graphitic carbon nitride materials : variation of structure and morphology and their use as metal-free catalysts. 4893–4908 (2008) doi:10.1039/b800274f.

27. Satyabadi Martha, Amtul Nashim, K. M. P. Facile synthesis of highly active g-C3N4 for efficient hydrogen production under visible light. *J. Mater. Chem. A* **1**, 7816–7824 (2013).

28. Chem, J. M. Graphene oxide modified g-C 3 N 4 hybrid with enhanced photocatalytic capability under visible light irradiation. 2721–2726 (2012) doi:10.1039/c1jm13490f.

29. Yue, B., Li, Q., Iwai, H., Kako, T. & Ye, J. Hydrogen production using zinc-doped carbon nitride catalyst irradiated with visible light. *Sci. Technol. Adv. Mater.* **12**, (2011).

30. Large, A. I. *et al.* Investigations of carbon nitride-supported mn3 o4 oxide nanoparticles for orr. *Catalysts* **10**, 1–19 (2020).

31. Martin, D. J. *et al.* Highly efficient photocatalytic H2 evolution from water using visible light and structure-controlled graphitic carbon nitride. *Angew. Chemie - Int. Ed.* **53**, 9240–9245 (2014).

32. Chen, X., Wang, X. & Fang, D. A review on C1s XPS-spectra for some kinds of carbon materials. *Fullerenes Nanotub. Carbon Nanostructures* **0**, 1048–1058 (2020).

33. Liu, C. *et al.* Efficient photoelectrochemical water splitting by g-c3n4/tio2 nanotube array heterostructures. *Nano-Micro Lett.* **10**, 1–13 (2018).

34. De Luca, F., Passalacqua, R., Abramo, F. P., Centi, G. & Abate, S. g-C 3 N 4 Decorated TiO 2 Nanotube Ordered Thin Films as Cathodic Electrodes for the Selective Reduction of Oxalic Acid. **84**, 37–42 (2021).

35. Ampelli, Claudio, Gabriele Centi, R. P. and S. P. Synthesis of solar fuels by a novel photoelectrocatalytic approach. *Energy Environ. Sci.* **3**, 253 (2010).

36. Fukushima, T., Higashi, M., Kitano, S., Sugiyama, T. & Yamauchi, M. Multiscale design for high-performance glycolic acid electro-synthesis cell: Preparation of nanoscale-IrO2-applied Ti anode and optimization of cell

assembling. *Catal. Today* **351**, 12–20 (2020).

37. Yamauchi, M. *et al.* Catalytic enhancement on Ti-Zr complex oxide particles for electrochemical hydrogenation of oxalic acid to produce an alcoholic compound by controlling electronic states and oxide structures. *Catal. Sci. Technol.* **9**, 6561–6565 (2019).

CHAPTER 4

4.1 Introduction

Nowadays, the overuse of fossil fuels, and global warming are two critical challenges for the world. Consequently, reducing atmospheric CO_2 concentrations has become a major focus point for sustainable development, and governments throughout the world have shown their concern by raising their investment in research to face this issue. Because of the large amount of CO_2 in the atmosphere, this gas can be regarded as a possible C_1 feedstock for the synthesis of chemicals and fuels, by carbon capture and utilization. Next to the CO_2 in the atmosphere, which is very diluted, an easier strategy is to convert the CO_2 from point sources. In this thesis, these issues are addressed by studying CO_2 as an alternative and economic raw material. For example, chapter 2 presents an experimental study on Cu supported by biomass of citrus peels used as electrocatalyst in the conversion of CO_2 into value-added products (C_1). As widely reported in literature[1–5], copper (Cu)-based catalysts have been identified as the main catalyst for CO_2 reduction. Unfortunately, Cu-based catalysts have low selectivity, and several products, such as carbon monoxide[6], methane[7], methanol[8], etc., can be produced. Therefore, it is crucial to develop Cu-based catalysts that have high selectivity, enhanced activity, and good stability, that provide the desired reduction products.

This chapter is based on:

Cai, Y., Michiels, R., De Luca, F., Neyts, E., Tu, X., Bogaerts, A., Gerrits N.
Improving Molecule-Metal Surface Reaction Networks Using the Meta-Generalized Gradient Approximation: CO_2 Hydrogenation. (Submitted)

Among these reduction reactions, the conversion of CO_2 to methanol (CH_3OH) is widely studied, because industrial demand is constantly increasing, and research efforts are currently being directed toward the production of it[9]. Methanol synthesis is most likely the most profitable CO_2 reduction reaction. It is recommended as an essential renewable energy transporter and storage chemical in the perspective of sustainability because it is a carbon-neutral source for the synthesis of fuels. Since the 1990s, Nobel laureate George A. Olah has supported the methanol economy[10,11] because atmospheric CO_2 may be utilized as a feedstock for methanol synthesis, and it has the potential to contribute to global warming mitigation[12]. Also, methanol is a vital chemical building block, and its demand is expected to rise steadily in the future[13]. Another advantage is that methanol is a convenient feedstock for the production of olefins, such as ethylene and propylene, currently produced from fossil resources, important synthetic products in the chemical industry[14]. Also, methanol is a low-flammable liquid, has the potential to be one of the main alternatives for fossil fuels, and it could be supplied using existing petroleum infrastructure and utilized with fuel cells to create energy. Despite the industrialization of this technology and a plethora of theorical papers[15–18] concerning the CO_2 reduction reaction to methanol, the active site of the catalyst and the mechanisms are currently debated. Due to the importance of this reaction, theoretical simulations can help interpret experimental findings and yield insights that would be impossible or difficult to obtain through experimental investigation. From this perspective, this chapter introduces the theoretical methods used to study the elementary reaction steps of the CO_2 reduction reaction to methanol on a Cu(111) catalyst.

4.2 CO_2 reduction to methanol

Methanol is an essential C_1 chemical and is currently industrially synthesized mostly from syngas (CO, CO_2, and H_2) derived from fossil resources such as natural gas, and coal[12,19]. The overall reaction is:

$$CO_2 + 3\ H_2 \rightarrow CH_3OH + H_2O$$

The reaction has an enthalpy change of ΔH = -57.86 kJ/mol[16]. CO_2 conversion to methanol is an exothermic reaction, according to Le Chatelier's principle, optimizing reaction conditions such as high pressure and low temperature thermodynamically favors CO_2 conversion to methanol. However, due to the chemical inert nature of CO_2, the high bond energy of the C=O double bond (750 kJ/mol)[20], a reaction temperature greater than 240 °C that favors CO_2 activation and methanol production is commonly used[21,22]. Badische Anilin Soda and Fabrik (BASF) created the first commercial syngas-based methanol synthesis method in the 1920s, which worked under strong reaction conditions (300-400 °C, 25-30 MPa) over ZnO-Cr_2O_3 catalysts. Since the 1960s, the technique developed by Imperial Chemical Industries (ICI) has dominated the industrial marketed methanol synthesis at less harsh reaction conditions (220-300 °C, 5-10 MPa) using $Cu/ZnO/Al_2O_3$ catalysts[23,24] Nonetheless, the catalytic performance of $Cu/ZnO/Al_2O_3$ catalysts was inadequate; the generation of water by-products increased ZnO agglomeration and oxidation of active Cu species, resulting in severe deactivation of the catalysts[25]. In light of the catalytic kinetics, the development of highly effective Cu-based catalysts in terms of activity, selectivity, water tolerance, and stability are required for the hydrogenation of CO_2 to methanol. Hence, novel Cu-based catalytic materials need to be developed to realize this conversion pathway of technological interest. According to the literature[17,18,26], the reaction of CO_2 to methanol on copper catalysts can proceed through several possible pathways: the formate path (HCOO*) through H_2COO^* or HCOOH*, the carboxyl path (COOH*) through CO* or COHOH* and the CO_2 dissociation path, as reported in figure 4.1. In the formate path, CO_2 reacts with adsorbed atomic H to generate formate (HCOO*). It then progressively converts into dioxomethylene (H_2COO^*), H_2COOH^*, formaldehyde (H_2CO^*), methoxy (CH_3O^*), and methanol (CH_3OH^*). The formate pathway has also been suggested to proceed through formic acid (HCOOH*) rather than dioxomethylene (H_2COO*).[21,27]

In the carboxyl pathway, CO_2* is hydrogenated to COOH*, which can either dissociate to CO* and OH* or be hydrogenated to COHOH*. Finally, CO_2* can dissociate into CO* and O* in the CO_2 dissociation route without passing through another intermediate.

Methanol synthesis via the carboxyl – CO* path, on the other hand, begins with the transformation of CO_2 into COOH*, which then dissociates into CO* and OH*.

In the CO_2 dissociation pathway, in green, CO_2* dissociates into CO* and O* without going through another intermediate first.

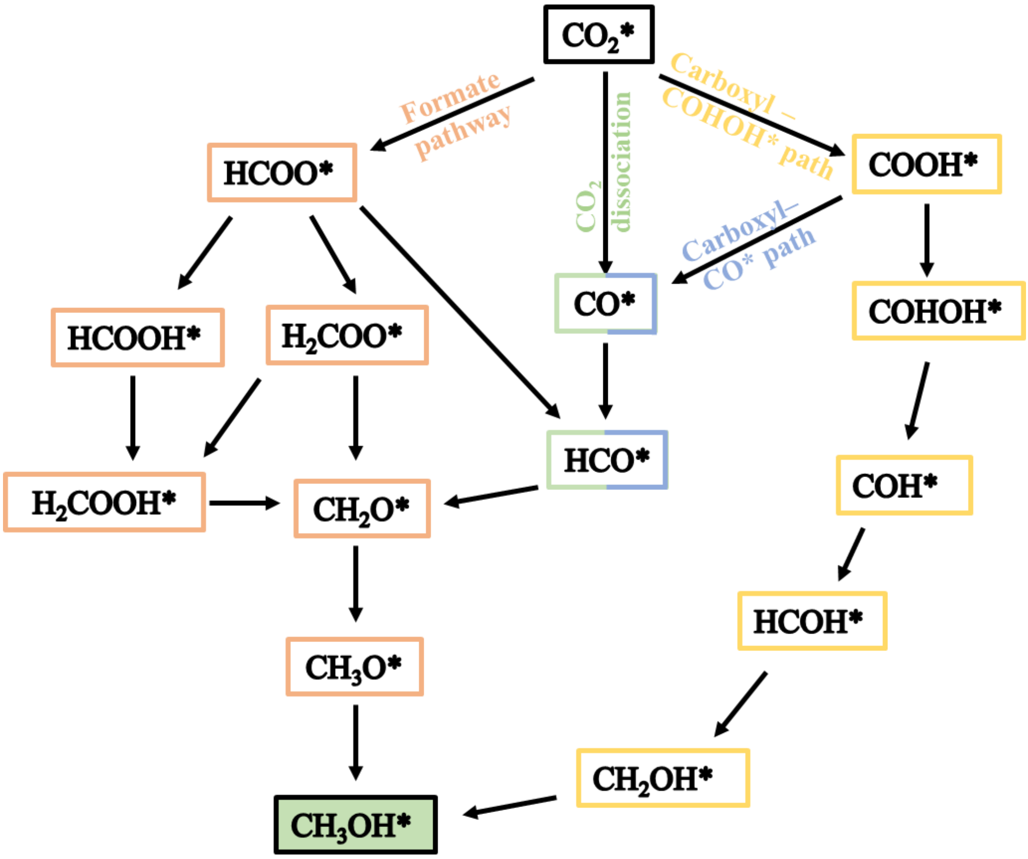

Figure 4.1: Pathways of CO_2 reduction to methanol, the formate path (orange), the carboxyl -CO* path (blue), the carboxyl – COHOH* path (yellow), and CO_2 dissociation (green).

The reaction pathways described above can however be influenced by a variety of parameters, including catalyst characteristics and reaction conditions.

4.3 Computational details

The Vienna Ab initio Simulation Package (VASP, version 6.2.1)[28–30] was used to perform periodic plane-wave density functional theory (DFT) simulations. To account for non-local correlation effects, the regularized made-simple RPBE-like (rMS-RPBEl)[31] MGGA DF was employed in conjunction with the rVV10[32] DF. The choice of using mGGA DFs is to avoid the limitations of generalized gradient approximation (GGA) DFs, such as underestimating the energy of the metal surface or barrier heights[33]. The projector augmented wave method[34,35] was used to characterize the core electrons. The plane-wave basis set had a kinetic energy cutoff of 600 eV, and the energy in the self-consistent field was converged to within 10^{-7} eV.

The Cu lattice constant is enhanced by employing a Γ-centered 20×20×20 k-point mesh. The optimization process ensured that the force on each atom was converged to within 0.005 eV/Å. The resulting lattice constant, determined using the rMS-RPBEl-rVV10 density functional, is 3.52 Å. This value aligns with the one reported by Smeets et al.[36] and corresponds well with the experimental value of 3.60 Å[37].

The Cu (111) surface is represented as a 3x3 periodic 6-layer slab with a 16 Å vacuum area added between periodic images of the slab in the z-direction. The three top layers and adsorbates are relaxed during the computations, whereas the bottom layers stay fixed at equilibrium bulk locations. For both slabs, the Brillouin zone is sampled using a Γ-centered 20x20x20 k-point mesh. The force on each atom has been converged to 0.01 eV/Å. With these parameters, the interlayer distance is optimized first. Only the z-coordinate of the atoms in the top three layers of the Cu(111) slab is permitted to relax, while the x- and y-coordinates remain fixed. All coordinates are relaxed in all other computations. The calculated interlayer distance between the first two top layers of the Cu(111) slab reveals a 1.8% increase, employing the rMS-RPBEl-rVV10 functional, which demonstrates good agreement with observations reported by Smeets et al.[36].

The procedure to be able to calculate the reaction energy (ΔE) and activation energy (E_a) is as follows: (i) searching the elementary steps of the formate pathway, (ii) creating a slab Cu model, (iii) geometric optimization of reactants and products of each reaction, (iv) finding the transition state by using two different methods (i.e., Nudge Elastic Band and dimer), and finally (v) the vibrational frequency analysis.

The Nudge Elastic Band (NEB) method is used to get a starting point for the dimer calculation. The NEB calculation is not completely converged, as it is only used to get a starting point for the dimer calculation.

The dimer technique, as implemented in the VASP Transition State Tools (VTST)[38–40] package, is used to determine transition states (TS), which are confirmed to be first-order saddle points by confirming that there is just one imaginary frequency in the normal mode analysis.

The adsorption energy of species, E_{ads}, is defined as:

$$E_{ads} = E_{adsorbate+surface} - (E_{surface} + E_{adsorbate}) \qquad \text{(eq. 5.1)}$$

Where $E_{adsorbate+surface}$, $E_{surface}$, and $E_{adsorbate}$ are the total energies of the adsorbate on the slab, the clean Cu slab and the gaseous adsorbate, respectively. The energy of the obtained Cu slab is equal to 370.84 eV.

4.4 Formate path

In the present thesis, only the formate path was explored for CO_2 hydrogenation to methanol on the Cu (111) surface. All of the investigated elementary steps are listed in table 4.1.

Table 4.1: Investigated elementary steps of the formate path.

Elementary steps
$CO_2 + H^* \rightarrow HCOO^* +^*$
$HCOO^* + ^* \rightarrow HCO^* + O^*$
$HCO^* + H^* \rightarrow CH_2O^* + ^*$
$HCOO^* + H^* \rightarrow H_2COO^* + ^*$
$H_2COO^* + H^* \rightarrow H_2COOH^* + ^*$
$HCOO^* + H^* \rightarrow HCOOH^* + ^*$
$HCOOH^* + H^* \rightarrow H_2COOH^* + ^*$
$H_2COOH^* + ^* \rightarrow CH_2O^* + OH^*$
$CH_2O^*+ H^* \rightarrow CH_3O^*$
$CH_3O^* + H^* \rightarrow CH_3OH^*$

Three possible catalytic sites (bridge step, top step, threefold hollow) have been considered as sites for adsorption, see figure 4.2.

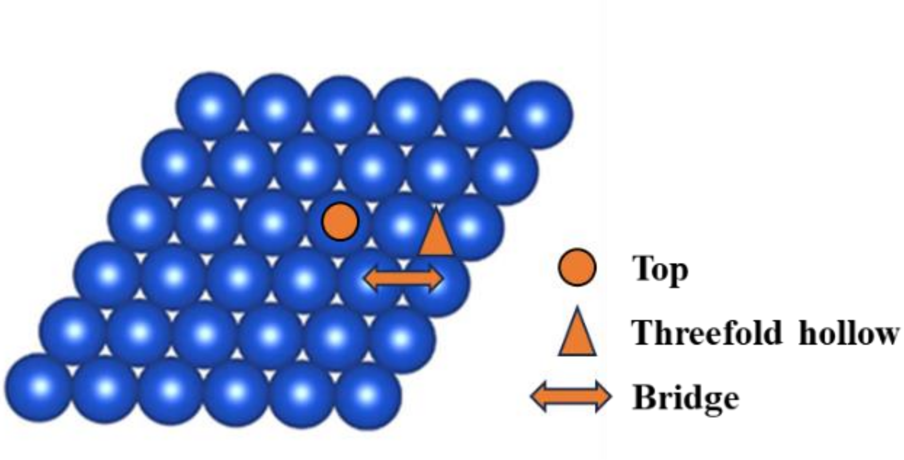

Figure 4.2: Possible catalytic sites of adsorption of reaction intermediates.

4.5 Results and discussion

Geometry optimization consists in finding the most stable configuration of each adsorbed species and the favored binding sites on the Cu (111) surface, i.e., the binding site at which the species has the lowest adsorption energy.

The adsorption energy, distance between Cu (111) surface and the adsorbate atom, and favorable adsorption sites of the stable molecules involved in the formate path are summarized in Table 4.2.

Table 4.2: Species, adsorption energy, corresponding distances between Cu and the relevant atom of the adsorbates, and adsorption site of stable molecules.

Species	**E_{ads} (eV)***	**Cu-A**	**Å**	**Site**
CO_2*	-0.12	d(Cu-C)	4.08	Physiosorbed
H*	/	d(Cu-H)	1.75	Threefold hollow
O*	/	d(Cu-O)	1.91	Threefold hollow
OH*	/	d(Cu-O)	2.03	Threefold hollow
HCOO*	/	d(Cu-O)	2.00	Top
HCOOH*	-0.38	d(Cu-O)	2.15	Top
H_2COO*	/	d(Cu-O) d(Cu-O)	1.99 2.03	O bridge O bridge
HCO*	/	d(Cu-C) d(Cu-O)	2.09 2.12	C bridge O top
H_2CO*	-0.25	d(Cu-O) d(Cu-C)	2.05 2.07	O bridge C top
H_2COOH*	/	d(Cu-O) d(Cu-O)	2.02 2.30	O bridge O top
H_3CO*	/	d(Cu-H)	2.03	Threefold hollow
H_3COH*	-0.38	d(Cu-H)	2.23	Top

*Adsorption energies are only calculated for stable molecules.

The optimized structures of reaction intermediates on Cu (111) shown in the side view are reported in figure 4.3.

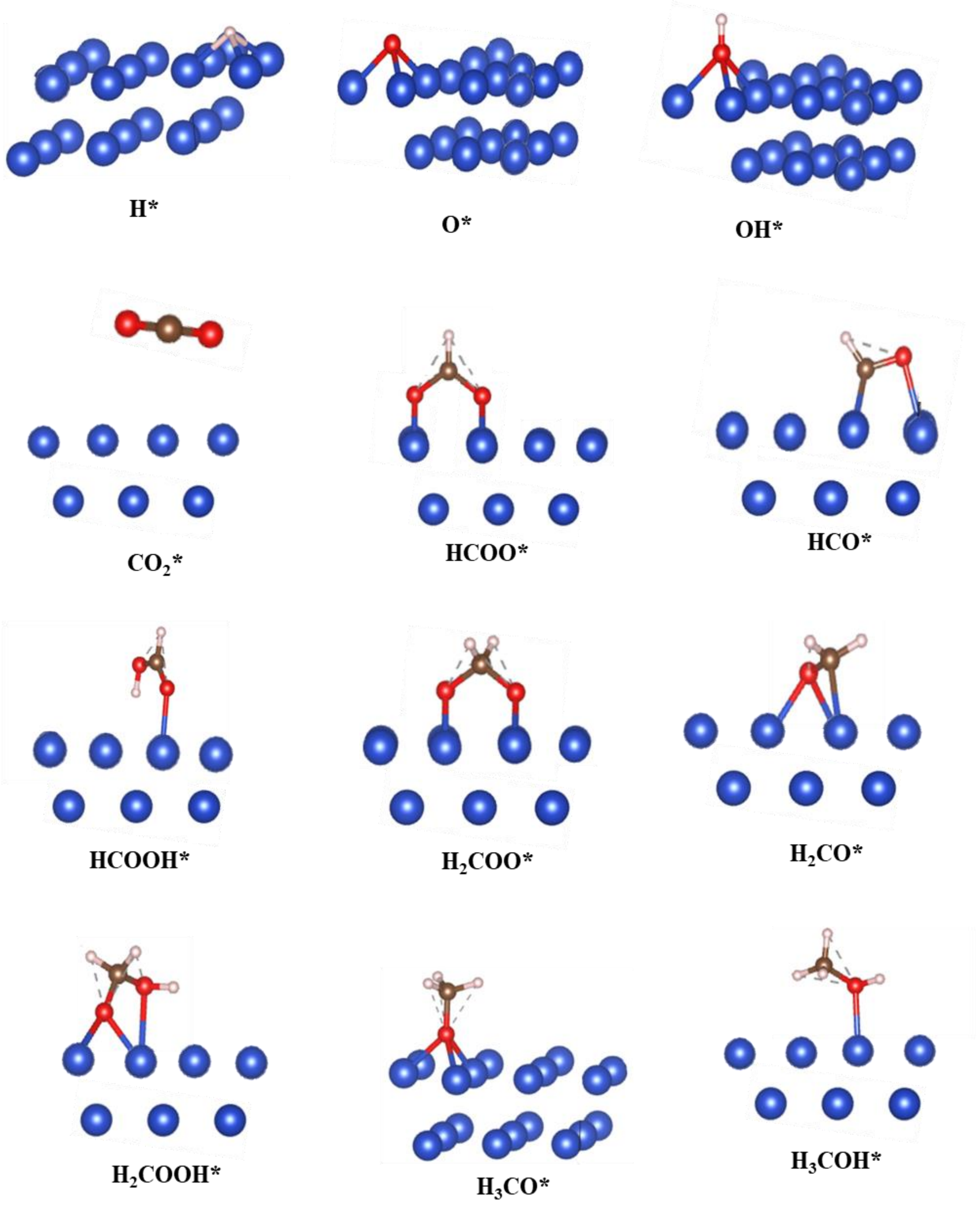

Figure 4.3. Optimized geometries for intermediates and products of CO_2 reduction to methanol on the Cu(111) surface.

As depicted in the figure 4.3, it is clearly highlighted that CO_2 shows physisorption characteristics, and interacts weakly with the Cu (111) surface, with an adsorption energy of about -0.12 eV , in line with literature[41,42]. The CO_2 molecule retains its linear structure, and the C-O bond length is about 1.18 Å, which is nearly identical to the experimental observation of 1.16 Å[43].

H*, O* OH* and prefer binding at threefold hollow sites on Cu (111).

Adsorbed formate (HCOO*) prefers bidentate configuration with oxygen atoms at top sites. The optimized Cu–O bond lengths are equal to 2 Å, consistent with the experimental values of 1.92 Å[44].

By hydrogenating HCOO*, two possible intermediates can be produced, i.e., formic acid (HCOOH*) and dioxymethylene (H_2COO*).

On Cu (111), HCOOH* binds at the top site by oxygen with a single Cu–O bond (2.15 Å). The binding energy of the optimized adsorbed HCOOH* is -0.38 eV.

The most stable configuration of H_2COO*, the other hydrogenation product, is with both O atoms bonded at bridge sites. The optimized Cu–O bond lengths are about 1.99 and 2.03 Å.

By decomposition of formate, formyl (HCO*) is produced. It prefers binding by carbon in bridge and oxygen in top. In the optimized configuration, shown in figure 4.3, the Cu–C and Cu–O bond lengths are 2.09 and 2.12 Å, respectively.

By hydrogenation of HCO*, formaldehyde (H_2CO*) can be produced. The binding energy of H_2CO* on Cu(111) is very weak (-0.25 eV), which is consistent with other theoretical calculations, reported in literature[45].

On Cu (111), H_2CO* binds at a top site through carbon and a bridge site by oxygen, with Cu-C and Cu-O bond length of about 2.05 and 2.07 Å, respectively.

Hydroxymethoxy (H_2COOH*) adsorbs at a bridge site via one oxygen atom and top-bonded with the other oxygen. The optimized Cu–O bond lengths are about 2.02 Å for the bridge site and 2.30 Å for the top site.

Methoxy (H_3CO^*) is produced by hydrogenation of formaldehyde. On Cu (111), its optimized geometrical configuration prefers adsorbing at a threefold hollow site through the O atom with a Cu–O bond length of 2.03 Å.

As the final desired product of CO_2 hydrogenation, methanol (CH_3OH) interacts with Cu(111) via the Cu–O bond (2.23 Å). The calculated binding energy is – 0.38 eV and its most stable structure binds via oxygen at a top site.

The total energy, characterized by the interaction adsorbate-surface, combines contributions from energies associated with surface binding (Van der Waals, ionic, covalent) with those associated with changes in intramolecular adsorbate binding. From theoretical results, it is known that the adsorption of organic molecules at metal surfaces shows different binding mechanisms depending on the adsorbate, substrate material, and the surface facets [46–48].

All the optimized adsorbates on Cu(111) surface and the total energy are listed in table 4.3.

Table 4.3: Adsorbates on Cu (111) surface and corresponding total energies.

Species	**E (eV)**
H^*	367.10
O^*	364.42
OH^*	360.26
CO_2^*	348.08
$HCOO^*$	343.96
HCO^*	352.09
$HCOOH^*$	340.70
H_2COO^*	340.89
H_2CO^*	348.15
H_2COOH^*	336.99
H_3CO^*	343.52
H_3COH^*	339.89

After the optimization of the reagents and products, the transition state of each elemental reaction has to be investigated. To identify the transition states, the NEB method and the dimer method were combined. A guess for the starting point of the dimer method is obtained by NEB, an example is depicted in figure 4.4.

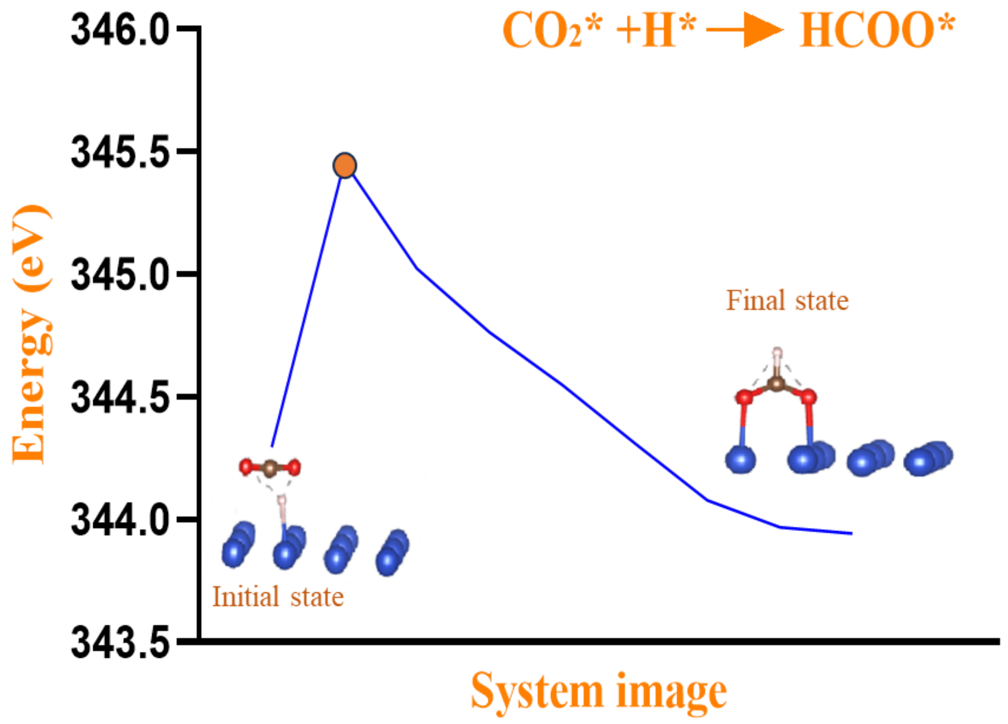

Figure 4.4: Guess of minimum energy path for the reaction CO_2* + H* → HCOO*.

The highest energy geometry is used as the initial geometry for the dimer calculation, this image is indicated by an orange circle in figure 4.4. The other images are used to estimate the direction of the maximal negative curvature. Finally, the transition state energy, listed in table 4.4, identified with the dimer method, is verified by analyzing that the vibrational frequency analysis only yields a single negative/imaginary frequency. These calculations are useful to verify the saddle point of the first order, i.e. a TS, that must only have one imaginary frequency.

Table 4.4: Transition states on Cu (111) surface with corresponding total transition state energies calculated with rMS-RPBEl-rVV10.

Elementary steps	**E (eV)**
$CO_2 + H^* \rightarrow HCOO^* + *$	345.18
$HCOO^* + * \rightarrow HCO^* + O^*$	342.54
$HCO^* + H^* \rightarrow H_2CO^* + *$	348.94
$HCOO^* + H^* \rightarrow H_2COO^* + *$	341.62
$H_2COO^* + H^* \rightarrow H_2COOH^* + *$	338.20
$HCOO^* + H^* \rightarrow HCOOH^* + *$	341.37
$HCOOH^* + H^* \rightarrow H_2COOH^* + *$	337.95
$H_2COOH^* + * \rightarrow CH_2O^* + OH^*$	337.77
$H_2CO^* + H^* \rightarrow CH_3O^*$	344.77
$CH_3O^* + H^* \rightarrow CH_3OH^*$	341.06

Thanks to the determination of the total transition state energy, it is possible to calculate the activation energy of each elementary step. These data and reaction energies are listed in table 4.5 in addition, they are compared with results obtained by Liu et al.[49] and Yang et al.[18]. Their calculations were performed using Perdew–Burke-Ernzerhof (PBE) and Perdew-Wang density functional, respectively.

Table 4.5. Reaction and activation energies of each step of CO_2 hydrogenation to methanol (formate pathway) on Cu (111).

Reactions			**Ref value**[18,49]	
Formate path	**ΔE (eV)**	**E_a (eV)**	**ΔE (eV)**	**E_a (eV)**
$CO_2 + H^* \rightarrow HCOO^* +^*$	-0.36	0.85	0.40	0.74
$HCOO^* + ^* \rightarrow HCO^* + O^*$	1.78	2.05	1.63	1.80
$HCOO^* + H^* \rightarrow HCOOH^* + ^*$	0.47	1.16	-0.22	0.34
$HCOO^* + H^* \rightarrow H_2COO^* + ^*$	0.67	1.40	0.34	1.32
$HCOOH^* + H^* \rightarrow H_2COOH^* + ^*$	0.04	1.00	-0.01	0.95
$H_2COO^* + H^* \rightarrow H_2COOH^* + ^*$	0.16	1.06	0.17	1.69
$H_2COOH^* + ^* \rightarrow CH_2O^* + OH^*$	0.61	0.78	0.60	0.82
$HCO^* + H^* \rightarrow CH_2O^* + ^*$	-0.19	0.59	-0.21	0.54
$H_2CO^* + H^* \rightarrow CH_3O^*$	-0.88	0.83	-0.82	0.28
$CH_3O^* + H^* \rightarrow CH_3OH^*$	0.11	1.29	-0.05	0.73

The first elementary step for CO_2 hydrogenation in the formate path on Cu (111) is to form HCOO*; it has an activation energy of about 0.85 eV, showing a higher value than the reference value that is equal to 0.74 eV.

HCOO* can undergo either dissociation or hydrogenation. The dissociation reaction leads to HCO* showing a higher energy reaction, approximately 2.05 eV, compared to the reference value equal to 1.80 eV. On the other hand, during hydrogenation, $HCOO^*$ can transform into either H_2COO^* or $HCOOH^*$, with activation energies of 1.40 eV and 1.16 eV, respectively. The reference values of both reactions are equivalent to 1.32 eV and 0.34 eV, respectively. As per activation energy, the $HCOOH^*$ formation seems to be more favorable than H_2COO^* production.

The produced $HCOOH^*$ may undergo hydrogenation to produce H_2COOH^*, with activation energies of 1.00 eV, slightly higher than reference value equal to 0.95 eV.

In turn, H_2COOH^* can undergo decomposition to CH_2O^* and OH^* with an activation energy of about 0.78 eV lower than the reference value that is equivalent to 0.82 eV.

The formation of CH_2O^* is crucial for methanol production, and it may undergo further hydrogenation to CH_3O^*. This reaction exhibits an activation energy of 0.83 eV. The activation energy is higher than the reference value equal to 0.28 eV.

Finally, the last elementary step in methanol formation involves the hydrogenation of CH_3O^* with an activation energy of 1.29 eV, significantly higher compared to the reference value equal to 0.73 eV.

In addition to the path through $HCOOH^*$, another path through H_2COO^* is known. H_2COO^* may undergo hydrogenation to produce H_2COOH^*. The reaction shows activation energy of about 1.06 eV, showing a lower value than the reference which is equivalent to 1.69 eV.

The activation energies are then compared with similar studies[18,49], but their calculations are performed using GGA functionals. By the comparison, it is highlighted that rMS-RPBEl-rVV10 usually predicts higher energy activation for surface reactions than GGA-level DFs[33] and indicates the potential for more accurate predictions of CO_2 hydrogenation processes for the formate route on the Cu (111) surfaces.

In figure 4.5 the potential energy diagram of the formate pathway on Cu(111)for both paths is shown.

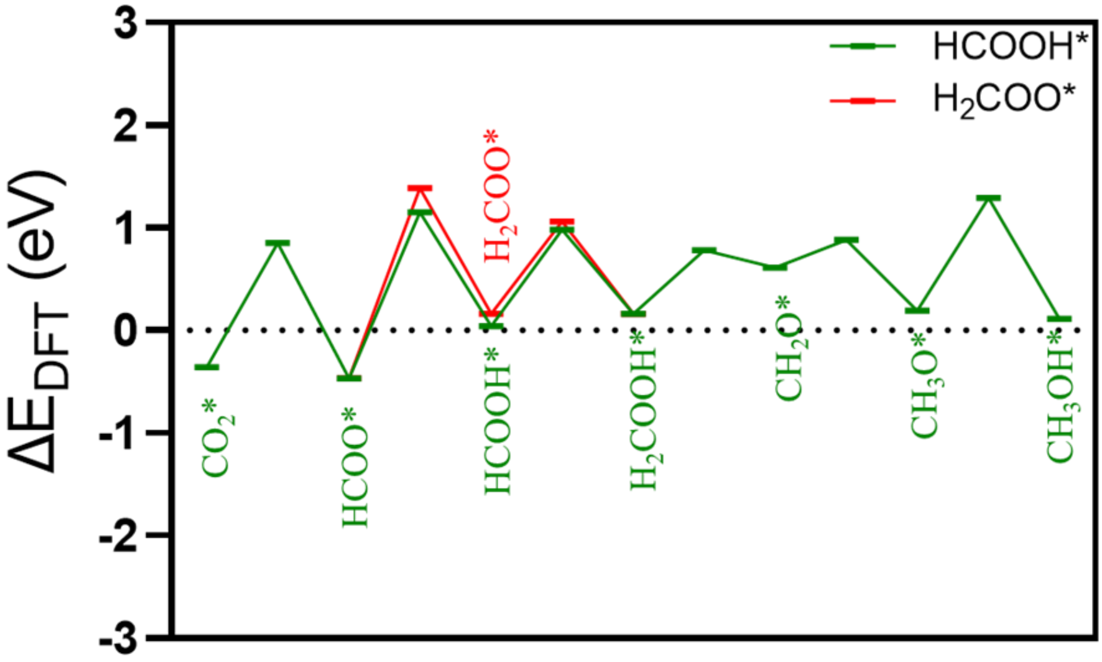

Figure 4.5: Potential energy diagram of the formate pathway on Cu(111), in red the path through H_2COO^* and in green the path via HCOOH*.

The potential energy diagram illustrates both variants of the formate pathway on Cu(111) surface, in green through HCOOH* and in red H_2COO^*. The reaction energies of the hydrogenation of HCOO* to H_2COO^* and HCOOH* on Cu(111) are both endothermic and have reaction energies of 0.67 eV and 0.47 eV, respectively. However, the formation of H_2COO^* has an energy activation higher (disagreement is approximately 0.27 eV) than the energy for HCOOH* formation. This suggests a preference for the reaction to HCOOH*. Also, the successive HCOOH* hydrogenation to H_2COOH^* has a slightly lower energy activation than H_2COO^* hydrogenation. Therefore, on the Cu(111) surface, the favorable pathway involves HCOOH* as an intermediate. Finally, the rate-controlling step on Cu(111) is CH_3O^* hydrogenation.

4.6 Conclusion

In summary, a systematic study was conducted to determine the activation energies for elementary reactions involved in the conversion of CO_2 to methanol on the Cu(111) surface, utilizing the rMS-RPBEl-rVV10 functional. The obtained activation energies were compared with calculations performed using the GGA density functionals, namely, Perdew–Burke-Ernzerhof (PBE) and Perdew-Wang (PW91 DF). A noticeable discrepancy in activation energies emerged across various elementary reactions, particularly highlighting the potential for more accurate predictions in CO_2 hydrogenation processes along the formate route on Cu (111) surfaces. The choice of using mGGA DFs is to avoid the limitations of GGA DFs. These DFs are recognized to struggle in offering precise forecasts for both molecular gas-phase and metal surface energies[50] concurrently, a requirement essential for investigating reactions occurring at metal surfaces. More precisely, GGA DFs that demonstrate proficiency in characterizing adsorption energies typically underestimate the energy associated with the metal surface and overestimate the metal lattice constant. Conversely, GGA DFs that exhibit effectiveness in modeling metallic systems often overstate adsorption energies[51]. Additionally, GGA DFs consistently display a tendency toward underestimating activation energy systematically[33].

Upon further analysis of the potential energy diagram (refer to Figure 4.5), it becomes evident that the rate-controlling step is the hydrogenation of CH_3O^*. In conclusion, the formate pathway on Cu(111) unfolds through $HCOOH^*$ intermediates and can be summarized as follows:$CO_2^* \rightarrow HCOO^* \rightarrow HCOOH^* \rightarrow H_2COOH^* \rightarrow CH_2O^* \rightarrow CH_3O^* \rightarrow CH_3OH^*$.

Bibliography

1. Rodriguez, J. A. *et al.* Hydrogenation of CO2 to Methanol: Importance of Metal-Oxide and Metal-Carbide Interfaces in the Activation of CO2. *ACS Catal.* **5**, 6696–6706 (2015).

2. Ou, L. Chemical and electrochemical hydrogenation of CO2 to hydrocarbons on Cu single crystal surfaces: Insights into the mechanism and selectivity from DFT calculations. *RSC Adv.* **5**, 57361–57371 (2015).

3. Jia, Y., Li, F., Fan, K. & Sun, L. Cu-based bimetallic electrocatalysts for CO2 reduction. *Adv. Powder Mater.* **1**, 100012 (2022).

4. Ren, D. *et al.* Selective Electrochemical Reduction of Carbon Dioxide to Ethylene and Ethanol on Copper(I) oxide catalysts. *ACS Catal.* **5**, 2814–2821 (2015).

5. Nitopi, S. *et al.* Progress and Perspectives of Electrochemical CO2 Reduction on Copper in Aqueous Electrolyte. *Chem. Rev.* **119**, 7610–7672 (2019).

6. Dinh, C. T., García De Arquer, F. P., Sinton, D. & Sargent, E. H. High rate, selective, and stable electroreduction of co2 to co in basic and neutral media. *ACS Energy Lett.* **3**, 2835–2840 (2018).

7. Dai, Y. *et al.* Manipulating local coordination of copper single atom catalyst enables efficient CO2-to-CH4 conversion. *Nat. Commun.* **14**, (2023).

8. Yang, H. *et al.* Scalable Production of Efficient Single-Atom Copper Decorated Carbon Membranes for CO2 Electroreduction to Methanol. *J. Am. Chem. Soc.* **141**, 12717–12723 (2019).

9. Etim, U. J., Song, Y. & Zhong, Z. Improving the Cu/ZnO-Based Catalysts for Carbon Dioxide Hydrogenation to Methanol, and the Use of Methanol As a Renewable Energy Storage Media. *Front. Earth Sci.* **8**, 1–26 (2020).

10. Olah, G. A., Goeppert, A. & Prakash, G. K. S. Chemical recycling of carbon dioxide to methanol and dimethyl ether: From greenhouse gas to renewable, environmentally carbon neutral fuels and synthetic hydrocarbons. *J. Org. Chem.* **74**, 487–498 (2009).

11. Olah, G. A., Prakash, G. K. S. & Goeppert, A. Anthropogenic chemical carbon cycle for a sustainable future. *J. Am. Chem. Soc.* **133**, 12881–12898 (2011).

12. Goeppert, A., Czaun, M., Jones, J. P., Surya Prakash, G. K. & Olah, G. A. Recycling of carbon dioxide to methanol and derived products-closing the loop. *Chem. Soc. Rev.* **43**, 7995–8048 (2014).

13. Sehested, J. Industrial and scientific directions of methanol catalyst development. *J. Catal.* **371**, 368–375 (2019).

14. Ye, M., Tian, P. & Liu, Z. DMTO: A Sustainable Methanol-to-Olefins Technology. *Engineering* **7**, 17–21 (2021).

15. Guan, Y. *et al.* Insights on the Catalytic Active Site for CO2 Reduction on Copper-based Catalyst: A DFT study. *Mol. Catal.* **511**, 111725 (2021).

16. Grabow, L. C. & Mavrikakis, M. Mechanism of Methanol synthesis on Cu through CO2 and CO hydrogenation. 365–384 (2011).

17. Azhari, N. J. *et al.* Methanol synthesis from CO2: A mechanistic overview. *Results Eng.* **16**, 100711 (2022).

18. Yang, Y., Evans, J., Rodriguez, J. A., White, M. G. & Liu, P. Fundamental studies of methanol synthesis from CO2 hydrogenation on Cu(111), Cu clusters, and Cu/ZnO(0001). *Phys. Chem. Chem. Phys.* **12**, 9909–9917 (2010).

19. Bertau, M., Offermanns, H., Plass, L., Schmidt, F. & Wernicke, H. J. Methanol: The basic chemical and energy feedstock of the future: Asinger's

vision today. *Methanol Basic Chem. Energy Feed. Futur. Asinger's Vis. Today* i–xxxi (2014) doi:10.1007/978-3-642-39709-7.

20. Kar, S., Goeppert, A. & Prakash, G. K. S. Catalytic Homogeneous Hydrogenation of CO2 to Methanol. *Co* 89–112 (2021) doi:10.1002/9783527824113.ch4.

21. Zhong, J. *et al.* State of the art and perspectives in heterogeneous catalysis of CO2 hydrogenation to methanol. *Chem. Soc. Rev.* **49**, 1385–1413 (2020).

22. Ma, J. *et al.* A short review of catalysis for CO2 conversion. *Catal. Today* **148**, 221–231 (2009).

23. Bart, J. C. J. & Sneeden, R. P. A. Copper-zinc oxide-alumina methanol catalysts revisited. *Catal. Today* **2**, 1–124 (1987).

24. Waugh, K. C. Methanol Synthesis. *Catal. Today* **15**, 51–75 (1992).

25. Jiang, X. Y. *et al.* Formic acid assisted synthesis of Cu-ZnO-Al2O3 catalyst and its performance in CO2 hydrogenation to methanol. *Ranliao Huaxue Xuebao/Journal Fuel Chem. Technol.* **51**, 120–128 (2023).

26. Mandal, S. C., Rawat, K. S., Garg, P. & Pathak, B. Hexagonal Cu(111) Monolayers for Selective CO2 Hydrogenation to CH3OH: Insights from Density Functional Theory. *ACS Appl. Nano Mater.* 7686–7695 (2019) doi:10.1021/acsanm.9b01751.

27. Pei, Y., Zhong, H. & Jin, F. A brief review of electrocatalytic reduction of CO2—Materials, reaction conditions, and devices. *Energy Sci. Eng.* **9**, 1012–1032 (2021).

28. Kresse, G. & Hafner, J. Ab initio molecular dynamics for liquid metals. *Phys. Rev. B* **47**, 558–561 (1993).

29. Kresse, G. & Hafner, J. Ab initio molecular-dynamics simulation of the

liquid-metalamorphous- semiconductor transition in germanium. *Phys. Rev. B* **49**, 14251–14269 (1994).

30. Kresse, G. & Furthmüller, J. Efficiency of ab-initio total energy calculations for metals and semiconductors using a plane-wave basis set. *Comput. Mater. Sci.* **6**, 15–50 (1996).

31. Smeets, E. W. F., Voss, J. & Kroes, G. J. Specific Reaction Parameter Density Functional Based on the Meta-Generalized Gradient Approximation: Application to H2 + Cu(111) and H2 + Ag(111). *J. Phys. Chem. A* (2019) doi:10.1021/acs.jpca.9b02914.

32. Sabatini, R., Gorni, T. & De Gironcoli, S. Nonlocal van der Waals density functional made simple and efficient. *Phys. Rev. B - Condens. Matter Mater. Phys.* **87**, 4–7 (2013).

33. Gerrits, N. *et al.* Density Functional Theory for Molecule-Metal Surface Reactions: When Does the Generalized Gradient Approximation Get It Right, and What to Do if It Does Not. *J. Phys. Chem. Lett.* **11**, 10552–10560 (2020).

34. Kresse, G. & Hafner, J. Norm-conserving and ultrasoft pseudopotentials for first-row and transition elements. *J. Phys. Condens. Matter* **6**, 8245–8257 (1994).

35. Kresse, G., Joubert, D. From ultrasoft pseudopotentials to the projector augmented-wave method. *Phys. Rev. B - Condens. Matter Mater. Phys.* **59**, 1758–1775 (1999).

36. Smeets, E. W. F. & Kroes, G. J. Performance of made simple meta-GGA functionals with RVV10 nonlocal correlation for H2 + Cu(111), D2 + Ag(111), H2 + Au(111), and D2 + Pt(111). *J. Phys. Chem. C* **125**, 8993–9010 (2021).

37. Haas, P., Tran, F. & Blaha, P. Calculation of the lattice constant of solids with

semilocal functionals. *Phys. Rev. B - Condens. Matter Mater. Phys.* **79**, 1–10 (2009).

38. Heyden, A., Bell, A. T. & Keil, F. J. Efficient methods for finding transition states in chemical reactions: Comparison of improved dimer method and partitioned rational function optimization method. *J. Chem. Phys.* **123**, (2005).

39. Kästner, J. & Sherwood, P. Superlinearly converging dimer method for transition state search. *J. Chem. Phys.* **128**, (2008).

40. Xiao, P., Sheppard, D., Rogal, J. & Henkelman, G. Solid-state dimer method for calculating solid-solid phase transitions. *J. Chem. Phys.* **140**, 1–6 (2014).

41. Zuo, Z. J., Wang, L., Han, P. De & Huang, W. Methanol synthesis by CO and CO 2 hydrogenation on Cu/γ-Al 2 O 3 surface in liquid paraffin solution. *Appl. Surf. Sci.* **290**, 398–404 (2014).

42. Gokhale, A. A., Dumesic, J. A. & Mavrikakis, M. On the mechanism of low-temperature water gas shift reaction on copper. *J. Am. Chem. Soc.* **130**, 1402–1414 (2008).

43. Hargittai, M. & Hargittai, I. Experimental and computed bond lengths: The importance of their differences. *Int. J. Quantum Chem.* **44**, 1057–1067 (1992).

44. Sotiropoulos, A., Milligan, P. K., Cowie, B. C. C. & Kadodwala, M. Structural study of formate on Cu(111). *Surf. Sci.* **444**, 52–60 (2000).

45. Lim, K. H., Chen, Z. X., Neyman, K. M. & Rösch, N. Comparative theoretical study of formaldehyde decomposition on PdZn, Cu, and Pd surfaces. *J. Phys. Chem. B* **110**, 14890–14897 (2006).

46. Niu, J. *et al.* Comprehensive review of Cu-based CO2 hydrogenation to CH3OH: Insights from experimental work and theoretical analysis. *Int. J. Hydrogen Energy* **47**, 9183–9200 (2022).

47. Chutia, A. *et al.* Adsorption of formate species on Cu(h,k,l) low index surfaces. *Surf. Sci.* **653**, 45–54 (2016).

48. Peng, G., Xu, L., Glezakou, V. A. & Mavrikakis, M. Mechanism of methanol synthesis on Ni(110). *Catal. Sci. Technol.* **11**, 3279–3294 (2021).

49. Liu, Y. M. *et al.* Reaction mechanisms of methanol synthesis from CO/CO2 hydrogenation on Cu2O(111): Comparison with Cu(111). *J. CO2 Util.* **20**, 59–65 (2017).

50. Peverati, R.; Truhlar, D.G. Quest for a universal density functional: the accuracy of density functionals across a broad spectrum of databases in chemistry and physics. *Philos. Trans. R. Soc. A*, *372*, (2014).

51. Schimka, L.; Harl, J.; Stroppa, A. Accurate surface and adsorption energies from many-body perturbation theory. *Nat. Mater.*, *9*, 741-744 (2010).

CHAPTER 5

5.1 Introduction

To ensure an efficient energy transition towards a low-carbon economy, the interest of the scientific community in technologies for using carbon dioxide (carbon capture utilization and storage, CCUS) has increased in recent years. For this purpose, a catalytic process and an electrocatalytic process for the production of glycolic acid (GC) are compared in this chapter. According to Polaris market research, the worldwide glycolic acid market is valued at USD 327 million in 2022, and it is predicted to reach USD 450 million by 2027, with an increase compound annual growth rate (CAGR) of 6.5% in the forecast period. The reason for the huge glycolic acid market is found in its several applications: the textile industry as a dyeing and tanning agent; in food processing as a flavoring agent and as a preservative; often used in emulsion polymers, as additive for ink and paint to improve flow properties; in the pharmaceutical industry as a skin care agent, etc. According to this massive market, new routes for glycolic acid production are crucial. Here, two processes are considered (i) oxidation of ethylene glycol, and (ii) reduction of CO_2. To model and predict the performance of these two different processes, the commercial software Aspen Plus 11 from AspenTech Inc. is used. This study was carried out during a 6-month collaboration with NextChem Tech S.p.A (Rome).

5.2 Catalytic process simulation

The simulated catalytic process is reported in the literature[1] and it is considered the benchmark process. It is simulated in Aspen Plus using the non-random two-liquid model (NRTL) to calculate the equilibrium phase.

According to the paper[1], the oxidation of ethylene glycol to glycolic acid is the last part of a process that involves 5 steps: (i) biomass gasification, (ii) methanol synthesis reaction, (iii) dimethyl oxalate synthesis reaction, (iv) dimethyl oxalate hydrogenation, and (v) oxidation of ethylene glycol to glycolic acid. In the simulation, the only analyzed step is the last one. To boost the catalytic performance for the selective oxidation of ethylene glycol to glycolic acid (GC) a bimetallic catalyst (Pt-Mn/MCM-41) is employed[2]. 1.5wt% of Pt and 1% in Mn are loaded on MCM-41 support.

As shown in figure 5.1, EG and O_2 are initially mixed and heated approximately at 60°C. Afterward, the feedstocks are sent into a Rstoich reactor for a selective oxidation reaction. Because the involved reactions are exothermic, cold water is used to keep the reactor at 60°C thus favoring the formation of products.

The selective oxidation of ethylene glycol to glycolic acid involves several reactions:

- $C_20_2H_6 + 2.5\ O_2 \rightarrow 2\ CO_2 + 3\ H_2O$ (Carbon dioxide)
- $C_20_2H_6 + 1.5\ O_2 \rightarrow CO_2H_2 + H_2O$ (Formic acid)
- $C_20_2H_6 + 0.5\ O_2 \rightarrow C_2O_2H_4 + H_2O$ (Glycolaldehyde)
- $C_20_2H_6 + O_2 \rightarrow C_2O_3H_4 + H_2O$ (Glycolic acid)

The ethylene glycol conversion is about 92.1%. The selectivities are the following: 94% to glycolic acid, 3.4% to formic acid, 2.4% to glycolaldehyde, and 0.1% to carbon dioxide.

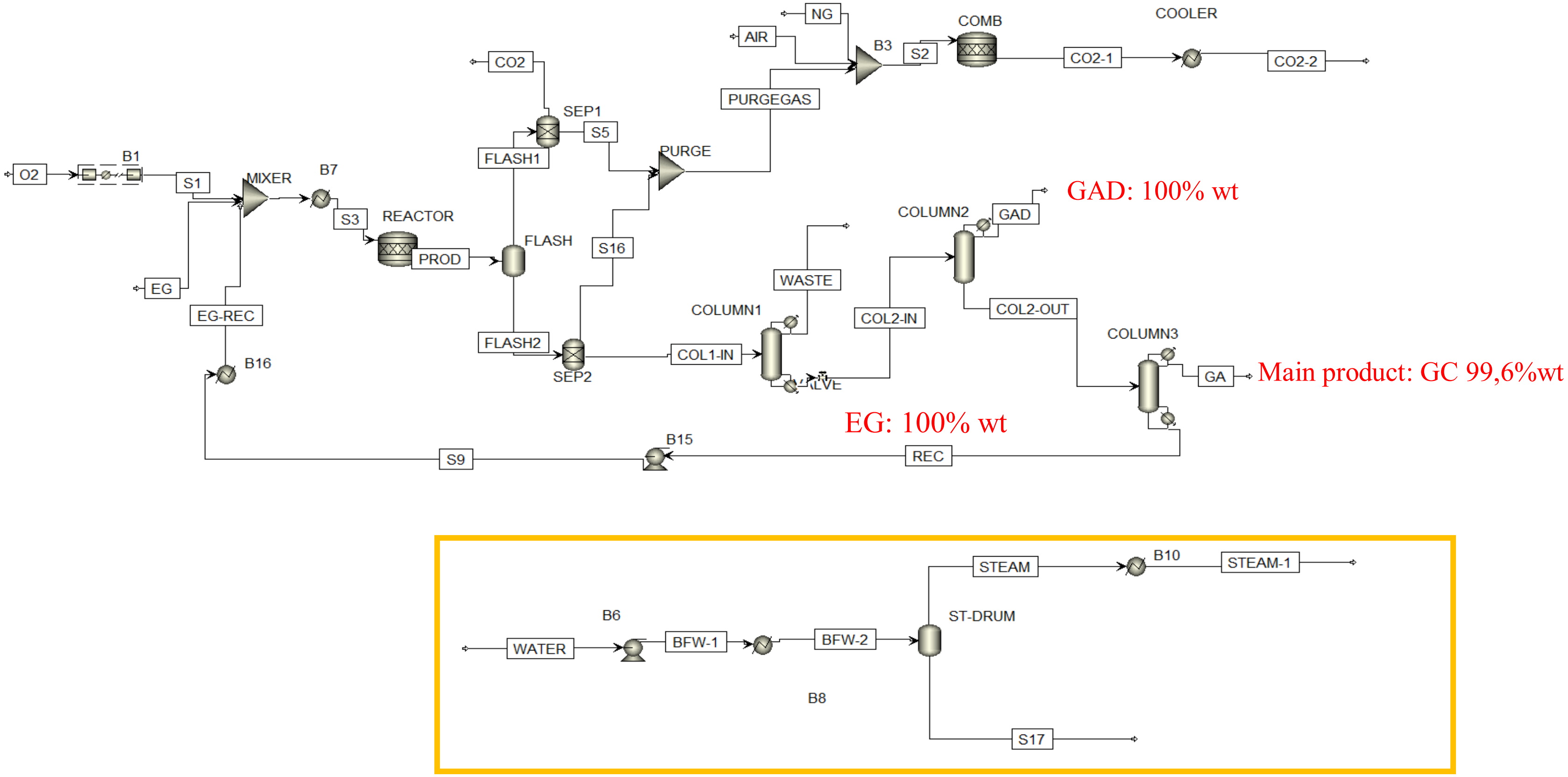

GAD: 100% wt

Main product: GC 99,6%wt

EG: 100% wt

Figure 5.1: Simulation flowsheet for the oxidation of ethylene glycol performed by Aspen Plus.

To summarize, the ethylene glycol conversion, the product selectivities, and molar fraction are listed in table 5.1.

Table 5.1: Conversion, products selectivities and molar fraction of ethylene glycol conversion.

	Conversion EG	Selectivity (%)	Molar fraction
Ethylene glycol	92.1	-	-
Glycolic acid	-	94	0.864
Formic acid	-	3.4	0.0335
Glycolaldehyde	-	2.5	0.023
Carbon dioxide	-	0.1	0.0005

The as-obtained products from Rstoich reactor are sent into the flash separator for the initial split of liquid and gaseous compounds. Lighter compounds, i.e., CO_2 and formic acid, and O_2 are sent in a purge stream. Here, they are mixed with a certain amount of air and natural gas before being burned (at 1110°C) to balance the energy needed. The required quantities of air and natural gas are calculated at the end of the simulation process to have the necessary heat to produce steam used in distillation column reboilers. Figure 5.1, in the yellow rectangle, shows that the needed quantity of heat is determined. A certain amount of water, calculated by:

$$\text{Steam} = \frac{Heat\ duty}{Latent\ enthalpy\ of\ vaporization} \qquad \text{(eq.5.1)}$$

is pumped and heated to produce the steam. Finally, the necessary heat is determined and the amount of natural gas to burn is calculated.

On the other hand, the liquid products, from the flash tank, are then fed into the vacuum dividing wall distillation column. The latter improve the energy efficiency and separation capabilities compared to traditional distillation columns. Also, it enhances the separation of thermally sensitive and easily decomposed substances and yield high-purity products[3] . It is the main reason for its use because glycolic acid and the byproduct glycolaldehyde have similar chemical-physical properties. In particular, they may undergo decomposition at a temperature above 86°C. By using divided wall distillation columns, it is possible to keep a low temperature and avoid product degradation. The distillation columns employed in the simulation have a configuration with 35, 30, and 45 stages, respectively. The temperature is always kept under 86°C and the pressure is approximately $8x10^{-3}$ bar.

This allows to obtain glycolaldehyde from the first distillation column with 100 wt.% purity, while from the second one, glycolic acid is collected with purity of 99.6 wt.%. Finally, most of the unconverted ethylene glycol is separated to be subsequently recycled.

The detailed mass data and parameters of the ethylene glycol oxidation process are listed in Table 5.2. It should be noticed that the stream names correlate to the simulation flowsheet depicted in figure 5.1.

Table 5.2: Mass data and parameters of ethylene glycol oxidation to glycolic acid.

BENCHMARK PROCESS															
Stream Name	**O2**	**EG**	**MIX**	**PROD**	**PURGE**	**CO2**	**COL1-IN**	**WASTE**	**COL2-IN**	**GAD**	**COL2-OUT**	**GA**	**REC**	**S2**	**CO2-2**
Temperature (°C)	60	30	60	60	56	72	72	100	74	51	76	75	83	25	150
Pressure (bar)	1.1	1.1	1.1	1.1	1.1	1.1	1.1	1.1	0.008	0.008	0.008	0.008	0.008	1.1	1.1
Mass Flows (kg/h)	511.98	980.68	1492.66	1492.66	87.15	0.62	1404.89	257.82	1147.07	28.66	1147.07	1041.06	77.34	49831.3	49831.3
Carbon dioxide	0	0	0	0.69	0.071	0.62	0	0	0	0	0	0	0	0.07	7188.54
Oxygen	511.98	0	511.98	48.59	48.59	0	0	0	0	0	0	0	0	10418.4	0.49
Glycolic acid	0	0	0	1038	0.34	0	1037.86	0	1037.86	0	1037.86	1037.84	0.01	0.34	0
Formic acid	0	0	0	33.45	33.45	0	0	0	0	0	0.0	0	0	33.45	0
Glycolaldehyde	0	0	0	31.88	0.048	0	31.83	0	31.83	28.65	31.83	3.18	0	0.048	0
Water	0	0	0	262.47	4.63	0	257	257.82	0.018	0.018	0.018	0	0	4.63	5876.5
Ethylene glycol	0	980.68	980.68	77.37	0.02	0	77.35	0	77.36	0	77.36	0.027	77.33	0.16	0
Natural gas	0	0	0	0	0	0	0	0	0	0	0	0	0	2608.55	0
Nitrogen	0	0	0	0	0	0	0	0	0	0	0	0	0	36765.8	63397.5

5.3 Electrocatalytic process simulation

The electrocatalytic process is simulated by using the electrolyte non-random two-liquid model (ELECNRTL) to calculate the equilibrium phase.

Most of the reactions to convert CO_2 to glycolic acid are taken from the "Oxalic acid from CO_2 using electrochemistry at demonstration scale" (OCEAN) project H2020. Its goal is to produce polymers starting from CO_2 following, approximately, these steps: (i) conversion of CO_2 to formate, (ii) coupling of formates into oxalate, (iii) acidification of oxalate to oxalic acid, (iv) conversion of oxalic acid to glycolic acid and other high-value C_2-products, and (v) the manufacturing process for polymers.

Figure 5.2 shows the process simulation to convert CO_2 mainly by electrocatalysis. The involved reactions are:

1st step: Formate production

$CO_2 + 2\,H^+ + 2\,e^- \rightarrow COOH^-$ (formate)

2nd step: Formate coupling

$2\,COOH^- \rightarrow (COOH^-)_2$ (oxalate)

3rd step: Glycolic acid production

$(COOH^-)_2 + 2\,H^+ \rightarrow H_2C_2O_4$ (oxalic acid)

$H_4C_2O_2 + 4\,H^+ + 4\,e^- \rightarrow H_4C_2O_3$ (glycolic acid)

CO_2 flow is inserted in an aqueous solution of $KHCO_3$ at 25°C and 2.2 bar. Then, CO_2 is converted to potassium formate (KFA) in the cathodic compartment of the first electrochemical cell (green rectangle). The potassium ion is provided by potassium bicarbonate ($KHCO_3$) which is consumed in the cell forming CO_2 and water. The salt mixture of $KHCO_2$/$KHCO_3$ is also functioning as electrolyte to allow ionic current in the cell. The electrochemical cell is a three-electrodes setup cell with a working electrode (cathode) based on a gas diffusion layer (GDL) covered by the catalyst, that is Bi/Bi_2O_3[4]. The faradaic efficiency of potassium formate is around 93% and the CO_2 conversion is about 20%. The anode side is based on an aqueous solution of $KHCO_3$. In this compartment occurs the oxidation of water that provides electrons to the cathode. The two sides of the electrochemical cell are divided by a proton exchange membrane that allows the H^+ to move on the cathodic side to hydrogenate CO_2, but a side reaction of H_2 production could occur. However, the potassium formate is then separated.

Solid potassium formate is heated in the presence of KOH (5 wt.%)[5] at 200 °C and 1.8 bar in N_2 ambient (orange rectangle). The KOH is used as catalyst for the thermal coupling of potassium formate to potassium oxalate. The reaction proceeds in a timescale of minutes with high conversion per pass (97%). The potassium oxalate product is separated from the produced H_2 and N_2.

Subsequently, oxalate is mixed with an aqueous solution of H_2SO_4 to transform it into oxalic acid and reach a pH of about 2.7. At the same time, the produced K_2SO_4 works as electrolyte in the cathodic side to allow the ionic current. Oxalic acid is then reduced in the cathodic compartment of a three-electrodes setup electrochemical cell (blue rectangle). The cathode used as catalyst is titanium nanotube array (TiNT) that promotes the reduction reaction of oxalic acid to glycolic acid. The reaction is carried out at 25 °C and 1.5 bar with oxalic acid conversion of 56% and a faradaic efficiency to glycolic acid approximately of 80%. The anode side is based on an aqueous solution of K_2SO_4. In this compartment occurs the oxidation of water that provides electrons and proton that through cation exchange membrane move to the cathode side.

This simulation allows to obtain glycolic acid as the main product with high purity, and in addition, O_2, produced by co-electrolysis, and glyoxylic acid (intermediate of oxalic acid in the third step) can be recovered. Finally, the unconverted CO_2 and oxalic acid are separated to be subsequently recycled.

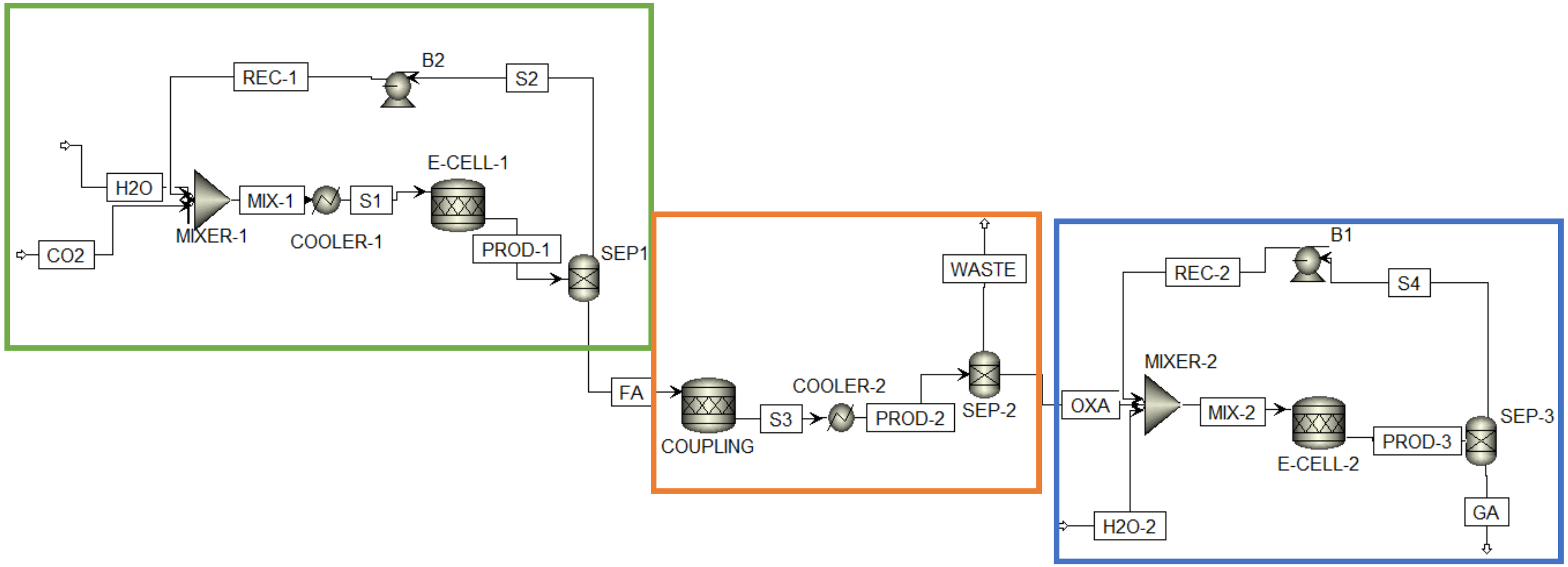

Figure 5.2: Simulation flowsheet of the CO_2 reduction to glycol acid process performed by Aspen Plus.

To summarize, the CO_2 conversion to glycolic acid chain, catalysts, faradaic efficiencies (FE), and conversion are listed in table 5.3.

Table 5.3: Catalysts, faradaic efficiencies, conversion, time of each step and mole of CO_2 conversion chain to glycolic acid.

Catalyst	FE (%)	Conversion (%)	Time (h)	Reference
1st step: CO_2 reduction to potassium formate				
Bi/Bi_2O_3-GDL	93	20	8	3
2nd step: potassium formate to potassium oxalate				
KOH (5 wt.%)	-	97	0,03	4
3rd step: oxalic acid reduction to glycolic acid				
TiNT	80	56	8	Experimental data

In addition, the detailed mass data and parameters of the CO_2 reduction process are listed in Table 5.4. It should be noticed that the stream names are correlated to the simulation flowsheet depicted in figure 5.2.

Table 5.4: Mass data and parameters of the CO_2 conversion chain to glycolic acid.

ELECTROCATALYTIC PROCESS										
Stream Name	**H2O**	**CO2**	**REC-1**	**PROD-1**	**FA**	**PROD-2**	**WASTE**	**H2O-2**	**REC-2**	**GA**
Temperature (°C)	25	25	25	25	25	25	25	25	25	25
Pressure (bar)	2.2	2.2	2.2	1.9	1.9	1.6	1.6	1.6	1.4	1.2
Mass Flows (kg)	889	5966	5172.92	6420.77	1247.85	1247.85	63.94	240	1293	1000.04
Carbon dioxide	0	5966	4772.8	4772.8	0	0	0	0	0	0
Water	889	0	400	400	0	0	0	0	627.07	0
Formate	0	0	0	1247.85	1247.85	37.43	37.43	0	0	0
Oxalate	0	0	0	0	0	1183.91	0	0	0	0
Oxalic acid	0	0	0	0	0	0	0	0	665.95	0
Glycolic acid	0	0	0	0	0	0	0	0	0	1000.04
Glyoxylic acid	0	0	0	0	0	0	0	0	0	0
Hydrogen	0	0	93	93	0	26.5	26.5	0	0	0

5.4 Economic analysis

To establish the financial viability of an industrial initiative, an economic analysis is required. To assess the economic effect of the building and operation of a chemical plant, technical information such as instrument specifications, size, and predicted operating conditions must be expected.

The feasibility or convenience of a process cannot be determined only by technical examination. While several process configurations may be technically possible, they may be substantially different commercially.

The costs of the plant are separated into two categories: operational costs and investment costs. Operating costs are the expenses incurred to maintain the facility throughout a specific period. The overall cost of planning, building, and installing the facility, on the other hand, is represented by investment expenses.

Operating expenses are divided as follows:

- Direct costs: production-related costs such as raw materials, wastewater treatment, services, work, and maintenance.
- Fixed expenses: costs that are not modified by output volume, such as plant and building depreciation, taxes, insurance, and general plant costs.
- General expenses including operational costs, distribution and sales costs, and research and development.

Investment expenses can be divided as follows:

- Direct project expenses: equipment costs, material, and labor costs (for installation and testing), control and instrumentation costs, pipeline, and electrical system costs
- Indirect project expenses: transportation, insurance, and taxation, as well as construction overhead and engineering costs.
- Surplus costs and fees

- Expenditure on ancillary facilities: expenditure on land, construction of auxiliary buildings, and expenditure on the development of off-site facilities and services.

The American Association AACE (Association for the Advancement of Cost Engineering) has identified five classes based on the level of design definition and required accuracy. The aim is to produce a cost estimate typical of the feasibility study phase for which the accuracy is 30%.

5.5 Operating expense

The operating expense (OPEX) represents the cost necessary to produce a product. Here, the costs considered for the synthesis of 1 ton of glycolic acid, by both processes, are the electricity, raw materials and CO_2 tax. In tables 5.5 the OPEX of the two processes are compared.

Table 5.5: Operating expenses of a) catalytic process, and b) electrocatalytic process to glycol acid (GC).

a) CATALYTIC PROCESS					
Feed and utilities	ton/ton GC	€/ton GC	kW/ton GC	€/ton GC	Total cost (€)
Ethylene glycol	0.94	47100	-		
Oxygen	0.48	24.3	-		
Natural gas	2.6	1300	-		
Carbon dioxide	7.5	725.35	-		
Demi water	23.4	46.8	-		
Electric power	-	-	107.28	13.95	
					2581.40

Electric power: 0,13 €/kWh; Ethylene glycol: 500 €/ton; Oxygen 70 €/ton; Natural gas 500 €/ton; Demi water: 2 €/m^3; CO_2 tax: 100 €/ton.

b) ELECTROCATALYTIC PROCESS					
Feed and utilities	ton/ton GC	€/ton GC	kW/ton GC	€/ton GC	Total cost (€)
Carbon dioxide	5.97	-	-	-	
Demi water	1.76	3.52	-	-	
$KHCO_3$	0.124	74.4	-	-	
K_2SO_4	0.035	6.96	-	-	
Electric power	-	-	6240	1039	
					1124.10

Electric power: 0,13 €/kWh; Green electric power: 0,14 €/kWh; Demi water: 2 €/m^3; $KHCO_3$ 600 €/ton: K_2SO_4 200 €/ton

For calculating the OPEX, mass (except for electrolytes $KHCO_3$ and K_2SO_4) and electric power data are determined by Aspen Plus. It is important to highlight that to make this process sustainable, it is hypothesized that the electric power is combination of green and fossil electricity.

As clearly shown in tables 5.5, the operational cost of the electrocatalytic process (1,124.1 €) is 56,5%lower than for the catalytic process (2,581.40€). Therefore, to compare them in-depth a capital expense (CAPEX) investigation is needed.

5.6 Capital expense

There are several methods for calculating the overall investment cost. Here, the Chilton method[6] is employed.

This approach requires previous knowledge of the cost of equipment procurement, which allows for the calculation of all other variable costs based on the kind of plant, taking into consideration the multiplier factors. The expenses of pipes, instruments, buildings, structures, supplementary services, and external lines are calculated in this manner. The total of all these approximates the direct expenses. After identifying the direct costs, the indirect costs may be estimated as a percentage of the direct costs.

To assess the cost of purchasing equipment, the analytical reports indicated in the book "Analysis, synthesis and design of chemical processes"[6] are used. The cost of individual equipment is given by:

$$C_p = C_P^0 * F_P * F_m \qquad \text{(eq. 5.2)}$$

Where C_P^0 stands for basic cost of equipment, F_P is the corrective factor used to take into account the pressure variation applied, and F_m is the corrective factor to consider materials used for the construction.

The base cost, C_P^0, is obtained from the following equation:

$$\log_{10} C_P^0 = K_1 + K_2 * \log_{10} A + K_3 * (\log_{10} A)^2 \qquad \text{(eq. 5.3)}$$

Where A is the representative size of equipment (kW), and K_1, K_2, K_3 are parameters that vary depending on the equipment.

The equation for the calculation of the pressure factor F_P is:

$$\log_{10} F_P = C_1 + C_2 * \log_{10} P + C_3 * (\log_{10} P)^2 \qquad \text{(eq. 5.4)}$$

Where P is the working pressure expressed in barg, and C_1, C_2, C_3 are parameters that vary depending on the pressure range.

Equipment prices calculated by these relations are for 2001 and should be reported to the current year using a cost index that considers the economic conditions different from when the data are collected. One of the most used indices is the CEPCI (Chemical Engineering Plant Cost Index). By knowing the index value in the reference year (I_1) and in the year of interest (I_2), and the equipment cost in the reference year (C_1), the cost in the year of interest (C_2) can be derived from the relation:

$$C_2 = C_1 * \frac{I_2}{I_1} \qquad \text{(eq. 5.5)}$$

For the period in which the data are collected (May/September 2001), the average value of CEPCI is 397; for 2023, the most recent index value is 798.

Therefore, the adjusted prices of the equipment of both processes are listed in table 5.6.

Table 5.6: Equipment and adjusted prices of catalytic and electrocatalytic processes.

Catalytic process		**Electrocatalytic process**	
Equipment	Adjusted price (€)	Equipment	Adjusted price (€)
Compressor	220,337	Pump	9,935
Pump	10,745	Pump	6,965
Pump	7,679	E-cell 1	925,000
Reactor	1,781,250	E-cell 2	2,000,000
Column 1	7,194	Vessels	294,190
Column 2	6,025	Heat exchangers	294,190
Column 3	604,068	**Total cost**	**3,530,280**
Columns steel	411,889		
Vessels	1,007,641		
Heat exchangers	1,007,641		
Total cost	**11,292,469**		

The total volume of the reactor is about 0.19 m^3. ^{B}y knowing the carbon steel density (ρ = 7500 kg/m^3) the needed steel kilos are calculated, and the final price is determined by multiplying them with the price of carbon steel (1250 €/ton).

Instead, the cost of electrochemical cells is determined by considering a price of 5000 €/$m^2$of cell, multiplied by the total area required. The latter is calculated proportionally to the productivity and the area of electrocatalyst on lab scale. Subsequently, the values are correct by dividing for the electrical efficiency.

The energy efficiency (EE) is obtained from the following equation[7]:

$$\mathrm{EE} = \frac{E^0 * FE}{E_{cell}} * 100 \qquad \text{(eq. 5.6)}$$

Where E^0 is the standard potential, FE is the faradaic efficiency and E_{cell} is the cell potential. Data to calculate the electrical efficiency are listed in table 5.7.

Table 5.7: Standard potential, faradaic efficiency, cell potential, energy efficiency and total area of the reactions CO_2 to formate and oxalic acid to glycolic acid.

	CO_2 to formate	**Oxalic acid to glycolic acid**
E^0	-1.43	-1.1
FE	93%	80%
E_{cell}	5 V	4.5 V
EE	26.6%	19.5%
Tot area	185 m^2	400 m^2

After the assessment of the equipment price for both processes, the overall cost of plants, building, and installing the facility can be determined (table 5.8).

Table 5.8: Comparison of investment cost between a) catalytic and b) electrocatalytic process.

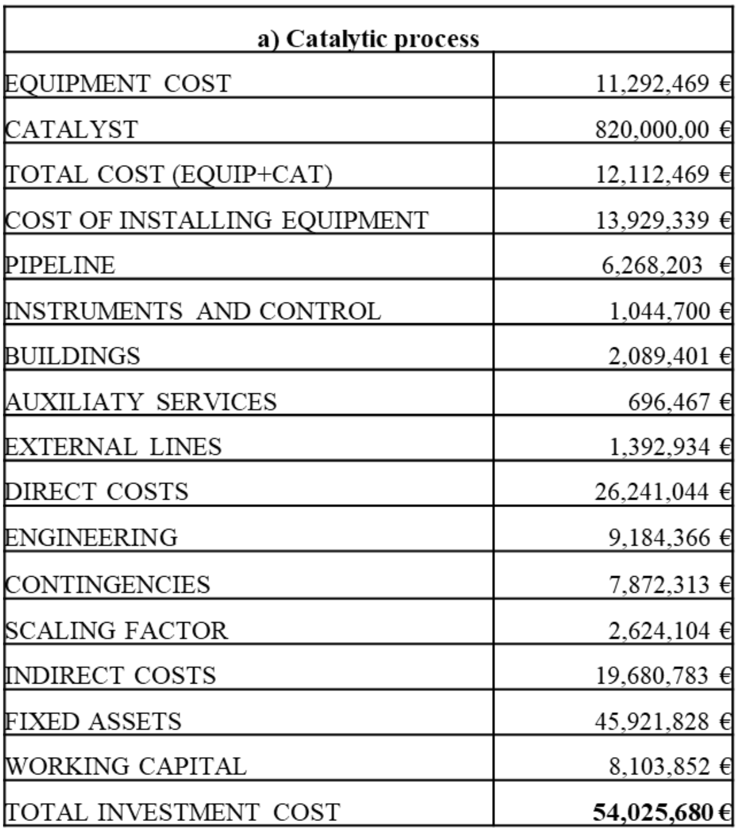

a) Catalytic process	
EQUIPMENT COST	11,292,469 €
CATALYST	820,000,00 €
TOTAL COST (EQUIP+CAT)	12,112,469 €
COST OF INSTALLING EQUIPMENT	13,929,339 €
PIPELINE	6,268,203 €
INSTRUMENTS AND CONTROL	1,044,700 €
BUILDINGS	2,089,401 €
AUXILIATY SERVICES	696,467 €
EXTERNAL LINES	1,392,934 €
DIRECT COSTS	26,241,044 €
ENGINEERING	9,184,366 €
CONTINGENCIES	7,872,313 €
SCALING FACTOR	2,624,104 €
INDIRECT COSTS	19,680,783 €
FIXED ASSETS	45,921,828 €
WORKING CAPITAL	8,103,852 €
TOTAL INVESTMENT COST	**54,025,680 €**

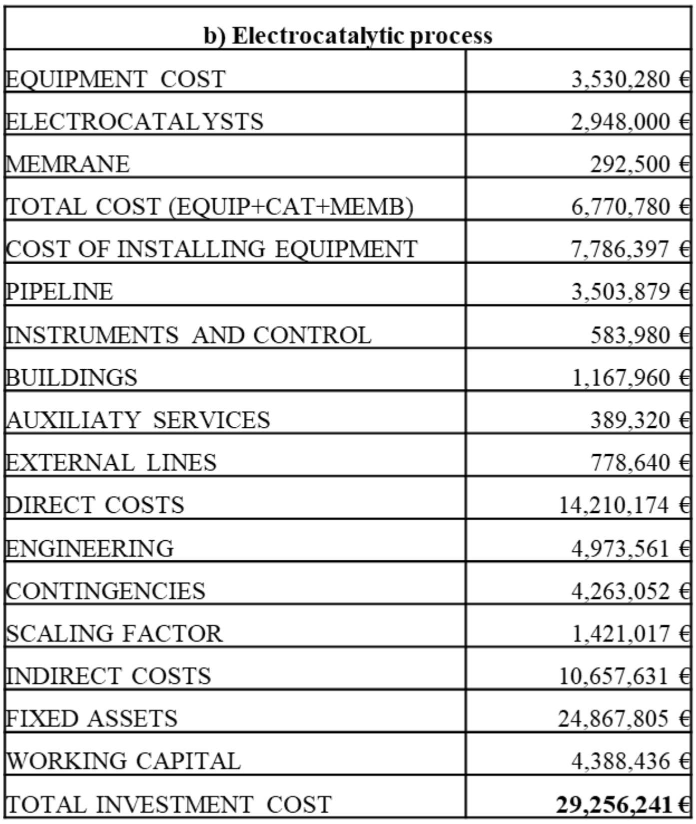

b) Electrocatalytic process	
EQUIPMENT COST	3,530,280 €
ELECTROCATALYSTS	2,948,000 €
MEMRANE	292,500 €
TOTAL COST (EQUIP+CAT+MEMB)	6,770,780 €
COST OF INSTALLING EQUIPMENT	7,786,397 €
PIPELINE	3,503,879 €
INSTRUMENTS AND CONTROL	583,980 €
BUILDINGS	1,167,960 €
AUXILIATY SERVICES	389,320 €
EXTERNAL LINES	778,640 €
DIRECT COSTS	14,210,174 €
ENGINEERING	4,973,561 €
CONTINGENCIES	4,263,052 €
SCALING FACTOR	1,421,017 €
INDIRECT COSTS	10,657,631 €
FIXED ASSETS	24,867,805 €
WORKING CAPITAL	4,388,436 €
TOTAL INVESTMENT COST	**29,256,241 €**

As with the operating cost, the investment cost of the electrocatalytic process (€29,256,241) is also 46% lower than that of the catalytic process (€54,025,680). In tables 5.9, a further comparison between the two processes is shown.

Table 5.9: Comparison of depreciation, maintenance and operation, and cost of the product between the a) catalytic and b) electrocatalytic process. The orange rectangle stands for the detailed maintenance costs for a period of 1-year of the catalytic process, while the blue and green rectangles show the detailed maintenance costs for a period of 100 h and 1 year, respectively, of the electrocatalytic process.

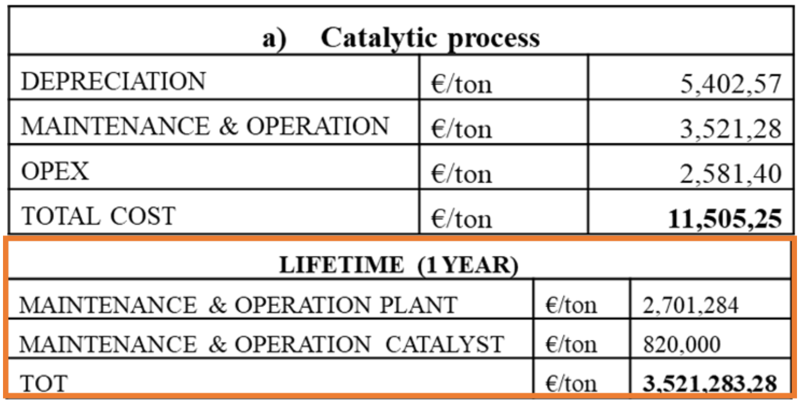

a) Catalytic process		
DEPRECIATION	€/ton	5,402,57
MAINTENANCE & OPERATION	€/ton	3,521,28
OPEX	€/ton	2,581,40
TOTAL COST	€/ton	**11,505,25**

LIFETIME (1 YEAR)		
MAINTENANCE & OPERATION PLANT	€/ton	2,701,284
MAINTENANCE & OPERATION CATALYST	€/ton	820,000
TOT	€/ton	**3,521,283,28**

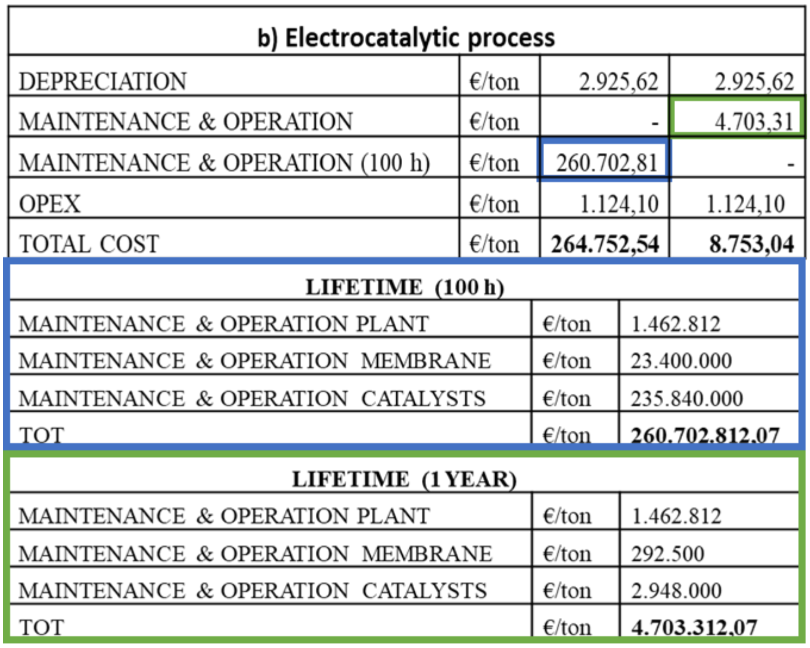

b) Electrocatalytic process			
DEPRECIATION	€/ton	2.925,62	2.925,62
MAINTENANCE & OPERATION	€/ton	-	4.703,31
MAINTENANCE & OPERATION (100 h)	€/ton	260.702,81	-
OPEX	€/ton	1.124,10	1.124,10
TOTAL COST	€/ton	**264.752,54**	**8.753,04**

LIFETIME (100 h)		
MAINTENANCE & OPERATION PLANT	€/ton	1.462.812
MAINTENANCE & OPERATION MEMBRANE	€/ton	23.400.000
MAINTENANCE & OPERATION CATALYSTS	€/ton	235.840.000
TOT	€/ton	**260.702.812,07**

LIFETIME (1 YEAR)		
MAINTENANCE & OPERATION PLANT	€/ton	1.462.812
MAINTENANCE & OPERATION MEMBRANE	€/ton	292.500
MAINTENANCE & OPERATION CATALYSTS	€/ton	2.948.000
TOT	€/ton	**4.703.312,07**

In table 5.9 the orange, green and blue rectangles show what the item maintenance and operation (M&O) includes. Itis calculated by the following equation:

$$\text{M\&O} = \frac{\text{Maint \& oper plant+ Maint \& oper cat (+ Maint \& oper membr)}}{annual\ capacity} \qquad \text{(eq. 5.7)}$$

Where the annual capacity is equal to 1000 ton/y.

To make clearer the economic weight of the maintenance and operation of the two processes a histogram is presented in figure 5.3. The graph shows the detailed maintenance and operation costs of the catalytic process, in orange, which is referred to as 1 year lifetime, while the electrocatalytic process compares two lifetimes 1 year, in green, and 100 h, in blue.

Due to the instability of the electrocatalysts and membranes, whose lifetime is estimated at approximately 100 h, the maintenance costs are elevated. Despite the OPEX and CAPEX expenses being lower for this process, the costs are unsustainable for industrial production, because, as shown in table 5.9 b, the total cost, which stands for the price of 1 ton of the product, is extremely high: 264,753 €.

In the optimistic case that the lifetime of catalysts and proton exchange membranes will be enhanced to 1 year or more, the electrocatalytic process might be more cost-effective than the catalytic one. Even if the maintenance costs are slightly lower for the catalytic process (€ 3,521) than for the electrocatalytic one (€ 4,703), as visible in figure 5.3, the price of 1 ton of product through the electrocatalytic process, as reported in table 5.9, is 8,753, which is 24% lower than the catalytic one (i.e., € 11,505).

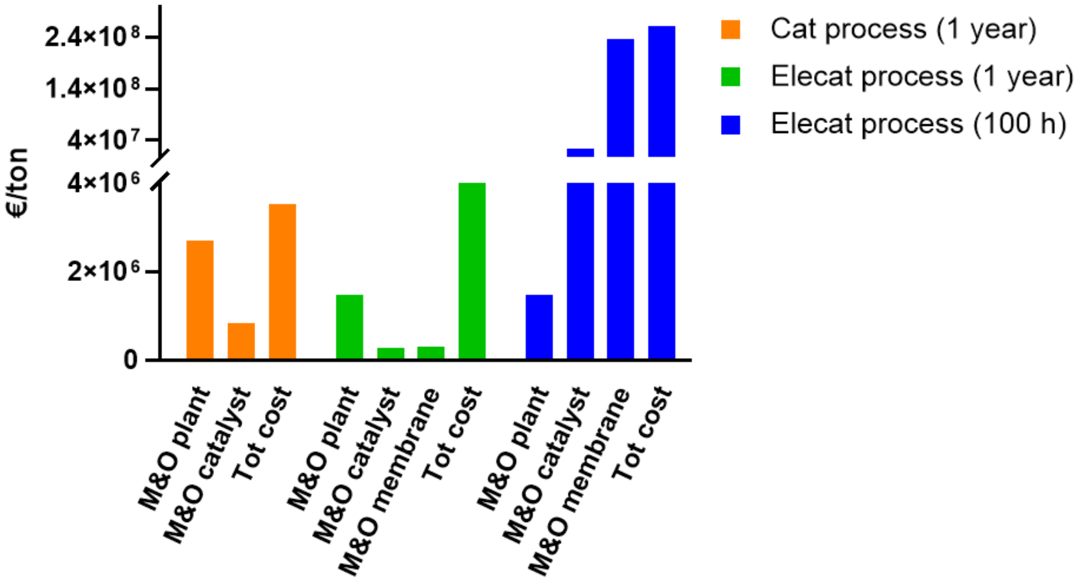

Figure 5.3: Comparison of maintenance costs for a period of 1-year of the catalytic process (orange), maintenance costs for a period of 1 year (green) and 100 h (blue) of the electrocatalytic process.

5.7 Conclusion

To summarize, a catalytical and an electrocatalytic process for producing glycolic acid are simulated by using Aspen Plus 11 software. The former involves the oxidation of ethylene glycol and the other one the reduction of CO_2. It is hypothesized that the two processes are carried out for 8000 h to produce 1000 ton/y. For both processes an economic analysis, including operational and investment expense, is carried out. It is concluded that despite the operational (table 5.5 b) and investment costs of the electrocatalytic process (table 5.8 b) being more advantageous, electrocatalysis is not a mature technology yet. The electrocatalysts and proton exchange membranes are not stable enough. Also, most of the electrocatalysts and proton exchange membranes after 60-100 h reduce their activity. Therefore, because they need to be changed approximately after 100 h, the product cost is approximately 20 times higher than the catalytic process. Only if, in the future, the electrocatalysts and proton exchange membranes are improved and the lifetime is increased to 1 year or more, the electrocatalytic process might be competitive because, as shown in table 5.9 b, the total cost would become 24% lower than for the catalytic one.

Bibliography

1. Zhou, X. *et al.* Glycolic Acid Production from Ethylene Glycol via Sustainable Biomass Energy: Integrated Conceptual Process Design and Comparative Techno-economic-Society-Environment Analysis. *ACS Sustain. Chem. Eng.* **9**, 10948–10962 (2021).

2. Yan, H. *et al.* Engineering Pt-Mn2O3 interface to boost selective oxidation of ethylene glycol to glycolic acid. *Appl. Catal. B Environ.* **284**, 119803 (2021).

3. Zhou, X. *et al.* Producing glyceric acid from glycerolviaintegrating vacuum dividing wall columns: conceptual process design and techno-economic-environmental analysis. *Green Chem.* **23**, 3664–3676 (2021).

4. Miola, M., Chillé, D., Papanikolaou, G., Lanzafame, P. & Pescarmona, P. P. Optimisation of the electrochemical conversion of CO2 into formate in a flow cell configuration using a bismuth-based electrocatalyst. *Green Chem.* **25**, 1875–1883 (2023).

5. Schuler, E., Ermolich, P. A., Shiju, N. R. & Gruter, G. J. M. Monomers from CO2 : Superbases as Catalysts for Formate-to-Oxalate Coupling. *ChemSusChem* **14**, 1517–1523 (2021).

6. R. Turton, J. A. Shaeiwitz, D. Bhattacharyya, and W. B. W. *Analysis, synthesis, and design of chemical processes*.

7. Matthew Jouny, Wesley Luc, F. J. A General Techno-Economic Analysis of CO2 Electrolysis Systems. 1–23.

CHAPTER 6

6.1 General conclusion

The constant increase in energy demand and the problems related to greenhouse gas emissions, in particular CO_2, has given rise to ecological and climate challenges. In this PhD thesis, different approaches have been explored with a focus on studying CO_2 as an alternative and economically viable raw material.

Chapter 2 focuses on the synthesis and characterization of novel electrocatalysts based on biomass. The main objective of the chapter is to discover sustainable, renewable, and efficient carbon-based electrode materials, such as biochar, for key electrochemical applications. Orange and lemon peels are utilized to demonstrate the feasibility of employing citrus waste directly in the synthesis of C-supported Cu nanoparticles using carbonaceous precursors naturally rich in ascorbic acid. This biomass offers two advantages: (i) serving as a carbon support for the Cu nanoparticles and (ii) providing the ascorbic acid necessary for Cu reduction. Subsequently, these electrocatalysts, containing Cu, are tested to evaluate their performance in the CO_2 electrocatalytic reduction reaction. The results highlight that biomass, due to its multifaceted role as a carbon support in electrocatalysis, presents the opportunity to use waste directly in the production of valuable materials in an environmentally friendly manner.

Chapter 3 presents the performance of g-C_3N_4/TiNT composites in the electrocatalytic reduction of oxalic acid, an intermediate in the CO_2 reduction chain. Oxalic acid can be further hydrogenated to produce valuable alcohols, such as glyoxylic and glycolic acid (the desired products). These products have added value, with the market estimated at around USD 170 million for glyoxylic acid and USD 327 million for glycolic acid in 2022, with predicted annual growth rates for

both. Given this significant market demand, it is crucial to synthesize novel electrocatalysts for their production.
An attempt to enhance TiNT, the primary electrocatalyst for oxalic acid reduction, is made through the chemical vapor deposition (CVD) of g-C_3N_4. The obtained results are promising, as the conversion of oxalic acid and the faradaic efficiency are superior to those of pristine TiNT. This suggests that the composite material, with its g-C_3N_4 dispersed layer, influences the selectivity toward glycolic acid as the principal product.

Chapter 4 presents a computational study on the synthesis of methanol conducted using the Vienna Ab initio Simulation Package software. This investigation contributes to the broader study on plasma catalysis conducted during a 6-month period abroad at UAntwerpen (Belgium). It is specifically focused on examining the reduction of CO_2 to methanol through the formate pathway on the Cu(111) surface, employing the mGGA DF method. As methanol production is extensively studied due to its increasing industrial demand and diverse applications (as a chemical building block, a low-flammable liquid, and an alternative to fossil fuels), there is a critical need to enhance the reaction. Theoretical simulations serve as a valuable tool for studying the elementary reaction steps.
A systematic study is conducted to define the activation energy, revealing that (i) the rate-controlling step is CH_3O^* hydrogenation, and (ii) the formate pathway on Cu(111) proceeds through $HCOOH^*$ intermediates. The overall pathway can be summarized as $CO_2^* \rightarrow HCOO^* \rightarrow HCOOH^* \rightarrow H_2COOH^* \rightarrow CH_2O^* \rightarrow CH_3O^* \rightarrow CH_3OH^*$.

Finally, Chapter 5 presents a process simulation conducted using Aspen Plus 11 software from AspenTech Inc. This study was carried out during a 6-month collaboration with NextChem Tech SpA (Rome).

Two processes were compared: (i) the oxidation of ethylene glycol through thermal catalysis and (ii) the electrocatalytic reduction of CO_2 for glycolic acid production. A systematic study was performed, initially providing information on the optimal operating conditions to minimize costs and enhance product quality for both simulations. Subsequently, an economic analysis of operational (OPEX) and capital (CAPEX) expenses was conducted. The OPEX analysis revealed that the electrocatalytic process is more cost-effective, with approximately 56% lower costs than the catalytic process. Similarly, the CAPEX analysis showed a significant price difference between the two processes, with the electrocatalytic process being economically advantageous, boasting a 46% lower capital cost. This suggests potential scalability for electrocatalytic processes at an industrial scale in the future.

However, it is important to note that despite the current cost-effectiveness of CAPEX and OPEX for the electrocatalytic process, the maintenance of electrocatalysts and proton exchange membranes remains prohibitively expensive. Consequently, under current conditions, the cost of 1 ton of glycolic acid in the electrocatalytic process is approximately 20 times higher than in the simulated catalytic process.

LIST OF PUBLICATIONS

Cai, Y., Michiels, R., **De Luca, F**., Neyts, E., Tu, X., Bogaerts, A., Gerrits N.
Improving Molecule-Metal Surface Reaction Networks Using the Meta-Generalized Gradient Approximation: CO_2 Hydrogenation. (Submitted)

Abramo, F. P., **De Luca, F.,** Chiodoni, A., Centi, G., Giorgianni, G., Italiano, C., Perathoner, S., Abate, S.
Nanostructure-performance relationships in titania-only electrodes for the selective electrocatalytic hydrogenation of oxalic acid. Journal of Catalysis, **429**, 115277 (2024). DOI: 10.1016/j.jcat.2023.115277

Miah, T., Demoro, P.,Nduka, I., **De Luca, F**., Abate, S., Arrigo, R.
Orange-Peel Biomass-derived Carbon Supported Cu Electrocatalysts Active in the CO_2-Reduction to Formic Acid. ChemPhysChem **202200589**, (2023).
DOI: doi.org/10.1002/cphc.202200589

Passalacqua, R., Abate, S., **De Luca, F.,** Perathoner, S., Centi, G.
Graphitic Layered Structures Enhancing TiNT Catalyst Photo-Electrochemical Behavior. Coatings, **13**, 358 (2023).
DOI: https://doi.org/10.3390/coatings13020358

Abramo, F. P., **De Luca, F.,** Passalacqua, R., Centi, G., Giorgianni, G., Perathoner, S., Abate, S.
Electrocatalytic production of glycolic acid via oxalic acid reduction on titania debris supported on a TiO_2 nanotube array. Journal of Energy Chemistry **68**, 669-678 (2021). DOI: 10.1016/j.jechem.2021.12.034

De Luca, F., Passalacqua, R., Abramo, F. P., Centi, G. & Abate, S. g-C_3N_4 *Decorated TiO_2 Nanotube Ordered Thin Films as Cathodic Electrodes for the Selective Reduction of Oxalic Acid.* Chemical Engineering Transactions **84**, 37–42 (2021). DOI: 10.3303/CET2184007

ABSTRACT PROCEEDINGS IN NATIONAL AND INTERNATIONAL CONFERENCES

Abramo, F. P., **De Luca, F.,** Chiodoni, A., Centi, G., Giorgianni, G., Italiano, C., Perathoner, S., Abate, S.
Insight the Ti nanotubes array nanostructure and its role on the electro reduction of CO_2-derived oxalic acid (OX). EUROPACAT2023 - 15th European Congress on Catalysis, Prague, Czech Republic, 27th August - 1st September 2023.

De Luca F., Miah, T., Demoro, P., Nduka, I., Arrigo R., Perathoner S., Centi, G., Abate S.
Biomass-derived Carbon Supported Cu Electrocatalysts for the CO_2-ElectroReduction. EUROPACAT2023 - 15th European Congress on Catalysis, Prague, Czech Republic, 27th August - 1st September 2023.

De Luca, F., Abate S., Passalacqua R., Perathoner, S.
Novel possibilities to produce high-value chemicals from CO2 by electrocatalysis. XIII National Catalysis Congress GIC 2003 Genova, 14th - 16th June 2023.

F.P. Abramo**, F. de Luca,** R. Passalacqua, P. Demoro, G. Centi, S. Perathoner, S. Abate
Metal-Free Nanocomposite Electrodes by Anodic Oxidation for Selective Electrocatalytic Hydrogenation Reactions. UCRA2022 – The 2nd International

Conference on Unconventional Catalysis, Reactors and Applications, Leamington Spa, the UK, 21st - 23rd September 2022.

De Luca, F., Passalacqua, R., Abramo, F. P., Centi, G. & Abate, S.
g-C_3N_4 decorated TiO_2 Nanotube Ordered Thin Films as Cathodic Electrodes for the Selective Reduction of Oxalic Acid. NINE2021 - The 4th International Conference on Nanotechnology Based Innovative Applications for The Environment 28th - 31st March 2021.

ATTENDED SEMINARY/WORKSHOP/SCHOOL

Trilateral eCCU^3 Workshop of the European Horizon 2020 projects on electrochemical carbon capture and utilization in the three European-funded projects LOTER.CO_2M, ECO_2 Fuel and OCEAN (30th March 2022).

SOLAR2CHEM X SEAFUEL Symposium (31st March - 1st April 2022).

Brevetti per invenzioni industriali: strumenti per la tutela delle invenzioni nascenti dalla ricerca universitaria (7th June 2022).

Workshop - Tips & Trics CAS SciFinder-n (23rd November 2022).

AvogAdro colloquia 2022 5th edition From Water to Chemicals: Vision and Opportunities of a Sustainable Hydrogen Society (15-16 December 2022).

Catalysis by carbon supported metal species: insights from advanced characterization techniques. (24th May 2023).

Scuola Chimica Industriale - Torino (28th May - 1st June 2023).

Reduction of CO_2 in the Chemical Industry - Tech. Approach to the Challenge. (4th October 2023).